

Bose-Einstein Condensation in Microgravity

Trapping of dilute quantum-degenerate gases in ultra-shallow
magnetic traps under microgravity conditions

DISSERTATION

zur Erlangung des akademischen Grades
doctor rerum naturalium
(Dr. rer. nat.)
im Fach Physik

eingereicht an der
Mathematisch-Naturwissenschaftlichen Fakultät I
Humboldt-Universität zu Berlin

von

Herr Dipl.-Phys. Wojciech Lewoczko-Adamczyk
geboren am 01.07.1979 in Koszalin (Polen)

Präsident der Humboldt-Universität zu Berlin:

Prof. Dr. Dr. h.c. Christoph Marksches

Dekan der Mathematisch-Naturwissenschaftlichen Fakultät I:

Prof. Dr. Lutz-Helmut Schön

Gutachter:

1. Prof. Dr. Achim Peters
2. Prof. Dr. Ernst Rasel
3. Prof. Dr. Hanspeter Helm

eingereicht am: 19.12.2007

Tag der mündlichen Prüfung: 16.03.2009

Abstract

Recently, cooling, trapping and manipulation of neutral atoms and ions has become an especially active field of quantum physics. The main motivation for the cooling is to reduce motional effects in high precision measurements including spectroscopy, atomic clocks and matter interferometry. The spectrum of applications of these quantum devices cover a broad area from geodesy, through metrology up to addressing the fundamental questions in physics, as for instance testing the Einstein's equivalence principle. However, the unprecedented precision of the quantum sensors is limited in terrestrial laboratories. Freezing atomic motion can be nowadays put to the limit at which gravity becomes a major perturbation in a system. Gravity can significantly affect and disturb the trapping potential. This limits the use of ultra-shallow traps for low energetic particles. Moreover, free particles are accelerated by gravitational force, which substantially limits the observation time.

Targeting the long-term goal of studying cold quantum gases on a space platform, we currently focus on the implementation of a Bose-Einstein condensate (BEC) experiment under microgravity conditions at the drop tower in Bremen. Special challenges in the construction of the experimental setup are posed by a low volume of the drop capsule as well as critical decelerations up to 50g during recapture at the bottom of the tower. All mechanical and electronic components were thus been designed with stringent demands on miniaturization and mechanical stability.

This work reports on the observation of a BEC released from an ultra-shallow magnetic potential and freely expanding for one second. Both, the low trapping frequency and the long expansion time are not achievable in any earthbound laboratory. This unprecedented time of free evolution leads to new possibilities for the study of BEC-coherence. It can also be applied to enhance the sensitivity of inertial quantum sensors based on ultra-cold matter waves.

Keywords:

Bose-Einstein condensate, microgravity, magnetic trap, atom-chip

Abstract

Ultra-kalte atomare Gase werden in zahlreichen Laboren weltweit untersucht und finden unter anderem Anwendung in Atomuhren und in Atominterferometer. Die Einsatzgebiete erstrecken sich von der Geodäsie über die Metrologie bis hin zu wichtigen Fragestellungen der Fundamentalphysik, wie z.B. Tests des Äquivalenzprinzips. Doch die beispiellose Messgenauigkeit ist durch die irdische Gravitation eingeschränkt. Zum einen verzerrt die Schwerkraft das Fallenpotential und macht damit die Reduktion der atomaren Energie unter einem bestimmten Limit unmöglich. Zum anderen werden die aus einer Falle frei gelassenen Teilchen durch die Erdanziehung beschleunigt und so ist deren Beobachtungszeit begrenzt.

Im Rahmen dieser Arbeit werden die Ergebnisse des Projektes QUANTUS (Quantengase Unter Schwerelosigkeit) dargestellt. Auf dem Weg zur Implementierung eines Quantengasexperimentes im Weltraum wurde innerhalb einer deutschlandweiten Zusammenarbeit eine kompakte, portable und mechanisch stabile Apparatur zur Erzeugung und Untersuchung eines Bose-Einstein-Kondensats (BEC) unter Schwerelosigkeit im Fallturm Bremen entwickelt. Sowohl die Abbremsbeschleunigung von bis zu 50 g als auch das begrenzte Volumen der Fallkapsel stellen hohe Ansprüche an die mechanische Stabilität und die Miniaturisierung von optischen und elektronischen Komponenten. Der Aufbau besteht aus einer im ultra-hoch Vakuum geschlossenen magnetischen Mikrofalle (Atomchip) und einem kompakten auf DFB-Dioden basierenden Lasersystem. Mit diesem Aufbau ließ sich das erste BEC unter Schwerelosigkeit realisieren und nach 1 Sekunde freier Expansion zu beobachten. Weder die schwache Krümmung des Fallenpotentials noch die lange Beobachtungszeit würden in einem erdgebundenen Experiment realisierbar.

Die erfolgreiche Umsetzung des Projektes eröffnet ein innovatives Forschungsgebiet - degenerierte Quantengase bei ultratiefen Temperaturen im pK-Bereich, mit großen freien Evolutions- und Beobachtungszeiten von mehreren Sekunden.

Schlagwörter:

Bose-Einstein Kondensat, Schwerelosigkeit, magnetische Falle, Atom-Chip

Dedication

Dla kochanych rodziców.

Contents

1	From Quantum to Cosmos	1
1.1	Introduction	1
1.2	Bose-Einstein condensate	3
1.3	Disadvantages of the gravity	5
1.3.1	Short observation time	5
1.3.2	Deformation of the trapping potential	5
1.3.3	Limited trap flatness	6
1.4	Advantages of the space environment	7
1.4.1	Atomic clocks	8
1.4.2	Atom interferometers	9
1.4.3	Benefits for the fundamental research	11
1.5	Existing cold atom platforms in microgravity	13
1.5.1	Experiments in the parabolic flights	13
1.5.2	ACES / PHARAO	13
1.5.3	QUANTUS	14
1.6	Composition of this thesis	16
2	Cold atom experiment at the Drop Tower in Bremen	18
2.1	The drop tower Bremen	18
2.2	Requirements on the experiment	21
2.3	Quantus experimental setup	23
2.3.1	Drop capsule overview	23
2.3.2	Vacuum	24
2.3.3	Chip trap and mirror MOT	25
2.3.4	Laser system	26
2.3.5	Drop capsule board computer	39
2.4	Time sequence	39
2.4.1	Doppler cooling in the magneto-optical trap	40
2.4.2	Optical molasses	42
2.4.3	Optical pumping	43
2.4.4	Magnetic Z-trap	44

2.4.5	Evaporative cooling	45
2.4.6	Phase transition to BEC	46
2.4.7	Decompression	46
2.4.8	Holding trap and free expansion	48
3	Atom chip	49
3.1	Magnetic trapping of neutral atoms	49
3.1.1	Magnetic potential	50
3.1.2	Harmonic approximation	51
3.1.3	Majorana losses	51
3.2	Microchip traps	52
3.2.1	Principle of operation	53
3.2.2	Ideal H-trap	57
3.2.3	Z-trap	62
3.2.4	Quantus chip	62
4	First observation of the Bose-Einstein condensate in micro-gravity	66
4.1	Evolution of the BEC in a time dependent trap	66
4.1.1	Thomas-Fermi approximation	67
4.1.2	Time dependent potential	68
4.1.3	Generalization to a rotating trap	69
4.2	Evolution of the trapping potential	69
4.2.1	Adiabatic decompression of the trap	69
4.2.2	Shift of the trap center by decompressing	71
4.2.3	Collective oscillation of the BEC in the decompressed trap	73
4.3	Free expansion of the BEC in microgravity	76
4.3.1	Center-of-mass motion	76
4.3.2	Systematic errors	76
4.3.3	Free (?) expansion	81
5	Future perspective	85
5.1	BEC in a magnetic insensitive state	85
5.2	Bragg diffraction of the condensate	87
5.3	The QUANTUS II project	89
	Appendix	85
A	Harmonic frequencies in a three-dimensional trap	93

B	Magnetic field of a finite piece of wire	95
B.1	Infinitely thin conductor	95
B.2	Infinitely flat conductor	96
B.3	Approximating an arbitrary shape conductor with a chain of thin straight wires	97
C	Technical drawings	99

List of Figures

1.1	BEC released from the trap, falling in the gravity	6
1.2	Deformation of a trap by the gravity	6
1.3	BEC after 50 ms free expansion	7
1.4	Atomic clock	8
1.5	Mach-Zender atom interferometer	10
1.6	First BEC in microgravity	15
1.7	1 s expansion of the BEC	16
2.1	Drop tower Bremen	19
2.2	Waterfall amplitude spectrum of g	20
2.3	Drop tower acceleration	20
2.4	Schematic of the drop capsule	21
2.5	QUANTUS drop capsule	24
2.6	Vacuum chamber	24
2.7	Mirror MOT	25
2.8	D2 transition in rubidium	27
2.9	Schematic of the laser system	28
2.10	Mechanical mount of the laser system	28
2.11	Linewidth of a DFB diode	29
2.12	Master laser and MOPA	31
2.13	AOM module	32
2.14	Laser lock bandwidth	33
2.15	Laser lock test on the mini drop tower	34
2.16	Laser test at ZARM drop tower	35
2.17	Block laser	36
2.18	Laser lock test by the catapult launch	37
2.19	U-MOT	42
2.20	Initial magnetic trap	44
2.21	Evaporative cooling	45
2.22	Enhancement in phase-space density	47
3.1	Larmor precession in a magnetic field	50

3.2	Magnetic field of a current carrying wire	54
3.3	Transverse gradient of the 2D quadrupole field	55
3.4	U- and Z-trap	56
3.5	H-trap	57
3.6	Cigar-like potential of the H-trap	59
3.7	Tilt of the trap principal axis	60
3.8	H-trap magnetic field	60
3.9	Potentials of extremely decompressed H- and Z-trap	62
3.10	Quantus chip	63
3.11	Biot-Savart law	64
3.12	Magnetic trap depth	65
4.1	Validity of the Thomas-Fermi approximation	68
4.2	Chip current and bias field by the decompression	70
4.3	Trap decompression	70
4.4	Adiabatic decompression of the trapping potential.	72
4.5	Calculated dipole oscillations	73
4.6	Measured dipole oscillation	75
4.7	Measured dipole oscillation in microgravity	76
4.8	Center-of-mass position of the BEC during 1 s TOF	77
4.9	Residual acceleration due to air friction	78
4.10	Residual magnetic field in the drop tower	79
4.11	Inaccuracy of a Helmholtz coil	80
4.12	Expansion of the BEC during 1 s TOF	82
4.13	Expansion of a thermal cloud	84
5.1	Adiabatic rapid passage	87
5.2	Bragg scattering of the BEC	88
5.3	Hybrid MOPA	90
5.4	The next generation of the vacuum chamber	91
B.1	A finite piece of a thin wire	95
B.2	A finite piece of a flat wire	96
B.3	Magnetic field of a finite piece of a flat wire	98
B.4	Approximating a flat conductor with a chain of thin wires	98
C.1	Wire structure of the Quantus chip	99
C.2	Lockbox circuit 1	100
C.3	Lockbox circuit 2	101
C.4	Scheme of the AOM module	102
C.5	Optical components of the Quantus laser system	104
C.6	MTS master laser	105

List of Tables

2.1	Dimensioning of the drop capsules	22
2.2	Cooling phases	41
3.1	IP coil trap from Amsterdam vs. Quantus chip	53

Chapter 1

From Quantum to Cosmos

1.1 Introduction

Human's curiosity to go beyond the current frontiers is the main catalyst of progress. During one of his "post-Nobel" lectures, Wolfgang Ketterle told a story of the people of a tropical tribe. They suffer from an awful heat, so they invent a fridge. Their motivation was just to cool drinking water, but to their surprise, they discover ice - a novel state of water!¹

There are many examples in everyday life showing that technological improvements revealed new phenomena, inspired new ideas, confirmed or dethroned well established theories. In physics, two such particularly rewarding trends have determined the way of making fundamental research in the last decades. The first is to still increase the energy of a system. New constituents of matter are sought for by colliding known particles accelerated to enormous energies in the TeV range. Incessant attempts to find the Higgs boson is an illustrative example here. On the other end of the energy scale there is a quest for achievement of ever lower temperatures. It was marked with important discoveries in the last centuries, like gas to liquid phase transitions, superfluidity or superconductivity.

Recently, cooling, trapping and manipulation of neutral atoms and ions has become an especially active field of quantum physics. The main motivation for the cooling is to reduce motional effects in high precision measurements including spectroscopy, atomic clocks and matter interferometry. The high speed of the atoms makes measurements difficult. The Doppler shift causes displacement and broadening of the spectral lines of thermal atoms.

¹Based loosely on the lecture: "Ultrakalte Quantengase: die kälteste Materie im Universum" held by W. Ketterle in 2004 by a colloquium of the Physical Society of Berlin (PGzB).

Furthermore, the high atomic velocities limit the observation time and thus the spectral resolution. To give some numerical examples, air molecules at room temperature move with speeds on the order of 300 m/s. At this speed it takes the particles only 3 ms to pass through a 1 m long detecting device. Cooling to 4 K, the temperature of liquid helium, would reduce the mean speed roughly 9 times only. Laser cooling allows one to slow neutral atoms to a speed as low as a few cm/s and the corresponding temperatures are in the μK range. Other powerful cooling technique, evaporative cooling can reduce this speed by another order of magnitude. At this low temperature some remarkable new phenomena appear: the wave nature of the particles becomes apparent. The de Broglie matter wavelength, given by $\lambda_{DB} = h/p$, where p is atomic momentum and h the Planck constant, becomes comparable to the mean atom-atom separation and a phase transition to the Bose-Einstein condensate occurs. Quantum degenerate matter of Bose-Einstein condensates forms the coldest objects in the universe with effective temperatures in the low nK range.

However, further reduction of the atomic energy is hardly possible. Freezing atomic motion can be nowadays put to the limit at which Earth's gravity becomes a major perturbation in a system. Unlike electromagnetic forces, gravity cannot be controlled by experimentalists. Rather, it is a constant accompanying potential which has to be accounted for when trapping massive particles. Inside of a closed trapping volume a trapping potential must feature a gradient that is larger than the gravitational force on the trapped atoms. This limits the usefulness of ultra-shallow traps for low energetic particles. In contrast, microgravity offers a significant potential to further extend the physics of degenerate quantum gases towards nowadays inaccessible regimes of low energies and macroscopic dimensions of coherent matter-waves. Physics at the lower end of the energy scale might result in a discovery of "ice in the fridge". New phases of matter could be observed and physical phenomena, like weak, long-range magnetic dipole-dipole interactions [Stuhler et al., 2005; Schmaljohann et al., 2004], could be studied in the reduced-gravity environment. Moreover, in the absence of gravity the trapping potential can be completely switched off. This will allow for an enhancement of the free evolution time of the released sample by many orders of magnitude. Longer observation times are crucial for increasing the precision of some measurements. For example, accuracy of the atomic clocks in space could be improved by a factor of ten compared to the currently most precise earthbound clocks [Laurent et al., 1998].

After a brief introduction to the issues of ultra-cold quantum degenerate matter, this chapter gives an overview of how particularly this field of modern physics can benefit from space environment. Advantages of weightlessness

are discussed and the state-of-the-art on the way to a quantum laboratory in space is presented.

1.2 Bose-Einstein condensate

Bose-Einstein condensate (BEC) is an unusual state of matter in which bosons collectively occupy the energetic ground state of a quantum system. Millions of atoms lose their identity and form a single macroscopic wave function. This property makes the BEC to a great extent similar to a laser in which large number of photons occupy the same mode of the electromagnetic field. Due to the resulting coherence of the wave function, BEC applications in matter-wave interferometry (atom optics) are very promising in terms of enhanced contrast. Experiments based on single particle interference with thermal ensembles features a coherence length typically well below a μm . The phenomenon of Bose-Einstein condensation allows to create for the first time a macroscopically occupied matter wave with coherence length up in the mm range.

BEC is a purely statistical phenomenon. In 1924, S.N. Bose derived an energy distribution function for photons closed in a finite volume [Bose, 1924]. He based just on a very few general assumptions, which are foundation of the statistical physics (for derivation of the Bose statistic see for instance [Alonso and Finn, 2005]). One year later, Einstein generalized Bose's approach to massive particles of an ideal noninteracting gas [Einstein, 1925]. Moreover, he recognized for the first time the phase transition in the occupancy number of the ground state when the temperature approaches the absolute zero.

Some physical effects, like superfluidity or superconductivity are explained by a partial Bose-Einstein condensation. Observation of BEC in excitons has also been reported in 1990 [Snoke et al., 1990]. However, first after the realization of the BEC in dilute atomic gases in 1995 [Davis et al., 1995a; Anderson et al., 1995; Bradley et al., 1995], the subject undergoes a renaissance as confirmed by the Nobel prize in 2001. The "golden era" of BEC is associated with dramatically increased number of publications covering a broad theme spectrum like matter wave interference, superfluidity and vortex lattices, solitons and four-wave mixing in matter waves, matter wave amplification and atom lasers, quantum phase transitions such as the superfluid to Mott insulator transition, quantum gas magnetism and controlled cold molecule production, to name only a few points. The physics of BEC has already been summarized in several review articles, e.g. [Ketterle et al., 1999; Bongs and Sengstock, 2004] and textbooks, e.g. [Pethick and Smith, 2002; Pitaevskii and Stringari, 2003]. Here, following the notation of [Pethick and

Smith, 2002], a brief summary of the most important issues will be pointed out.

At a given temperature T the mean occupation number of the single particle state ν is given by the Bose distribution function:

$$f(\epsilon_\nu) = \frac{1}{e^{\frac{\epsilon_\nu - \mu}{kT}} - 1}, \quad (1.1)$$

where k is the Boltzmann constant, ϵ_ν the energy of the state ν and μ the chemical potential. μ is determined from the normalization of the distribution 1.1 to N and its physical meaning is the energy required to add one particle to the system. As the temperature decreases, μ rises and approaches ϵ_{min} , the energy of the ground state. If $\mu = \epsilon_{min}$, the occupation of the ground state $f(\epsilon_{min})$ goes to infinity: the condensation occurs.

For a three-dimensional harmonic trap characterized by the oscillation frequencies ω_i ($i = 1, 2, 3$) and confining N particles the condensation begins at the critical temperature T_c :

$$kT_c \approx 0.94\hbar\bar{\omega}N^{1/3} \quad (1.2)$$

with $\bar{\omega} = (\omega_1\omega_2\omega_3)^{1/3}$. If the temperature further decreases, e.g. when the cooling process proceeds, the fraction of condensed particles increases as

$$\frac{N_{BEC}(T)}{N} = 1 - \left(\frac{T}{T_c}\right)^3. \quad (1.3)$$

For noninteracting gases with large N , condition 1.2 can be equivalently expressed in terms of the phase-space density ρ_{ps} . This is defined as the product of the atomic density n and the cube of the thermal de Broglie wavelength λ_{dB} :

$$\rho_{ps} = n\lambda_{dB}^3 = n \left(\frac{2\pi\hbar^2}{mkT}\right)^{3/2}, \quad (1.4)$$

where m is the atomic mass. The BEC transition appears when $\rho_{ps} = 2.612$. A phase-space density close to unity means that the de Broglie wavelength is comparable to the mean distance $n^{-1/3}$ between the atoms. The waves associated with the individual atoms begin to overlap and form a giant single wave, a condensate.

One important issue of the BEC is its extremely narrow velocity distribution compared to that of the thermal atoms. This holds even in the presence of repulsive interatomic interactions in the BEC. The interaction strength depends on the atom density, thus it decreases in a shallow trap, whose ground state is considerably extended in space. In the limiting case of an extremely

decompressed trap, in which interactions could be neglected, the spreading of the BEC released from the trap results from the Heisenberg uncertainty principle and thus from the initial density distribution. It follows, that increasing the size of the ground state of the trap, that is decreasing its energy, slows down the expansion speed. The experiment described in this thesis allowed for the observation for the first time of a freely evolving BEC for a time scales of the order of 1 s. Both, the low steepness of the trap and the unprecedented time of the free evolution would not be achievable in an earthbound laboratory due to a disturbing effect of gravity.

1.3 Disadvantages of the gravity

1.3.1 Short observation time

Consider a sample of ^{87}Rb atoms cooled to a few nK - the critical temperature at which the Bose-Einstein condensation occurs. At this temperature the corresponding average energy per atom is equal to the gravitational potential energy of a single Rb atom at the height of 100 nm, much smaller than a typical physical extension of the condensate. Moreover, the atoms have, on average, a speed of less than 2 mm/s. If the confining potential is switched off the atoms accelerate pulled by the gravity. After just one tenth of a second their velocity exceeds the initial velocity by a factor 50. After another tenth of a second they have dropped by 20 cm and have usually hit the bottom of the vacuum chamber in which they were cooled. In practice the observation time is limited to the time of flight through the view field of the imaging device. A typical series of absorption images of the condensate taken on the ground for increasing time of flight (TOF) is shown in figure 1.1. After 30 ms TOF the atoms fly out of the 5 mm view field of the CCD-camera chip.

1.3.2 Deformation of the trapping potential

The destructive influence of the gravity on a trapping potential is shown in figure 1.2. If the trap was harmonic, the addition of the linear term $-mgz$ would pull down² the potential minimum by $\Delta z = g/\omega^2$, where m is an atomic mass and g the gravitational acceleration. This effect is known as the "gravitational sag". However, real trapping potentials can be approximated by harmonic only (if at all) in the vicinity of the minimum (see appendix A). In the space region where the gradient of the trapping potential is smaller than mg , that is where gravity dominates over the trapping force, the trap is

²Note that throughout this work the z -axis points down, just as \vec{g} .

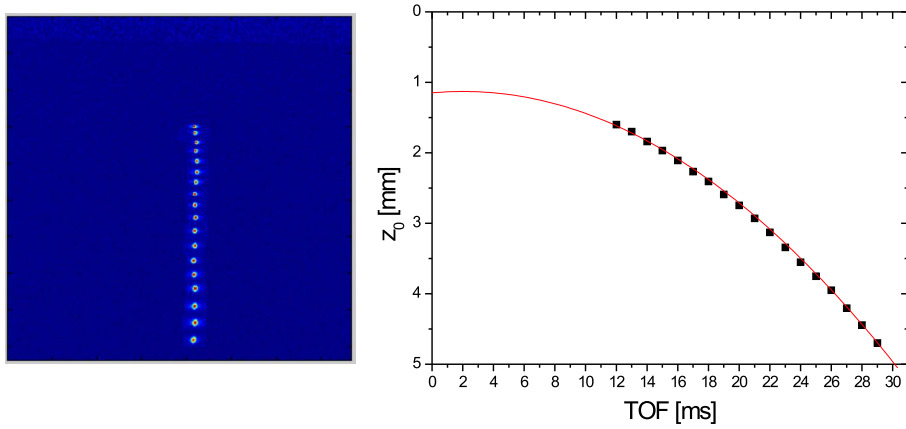


Figure 1.1: A series of absorption images of the condensate released from the trap (left). Since the measurement is destructive, each image represents a new experiment with TOF increasing in 1 ms steps. Vertical position as a function of TOF (right). The red solid line represents the expected acceleration due to the Earth gravity.

open. Particles with energies higher than the potential barrier ΔU can leave the trap.

Gravity is also a disturbing factor for the trapping of cold gas mixtures. Atoms with different masses experience different gravitational forces and therefore can not be equally well held by the trapping potential.

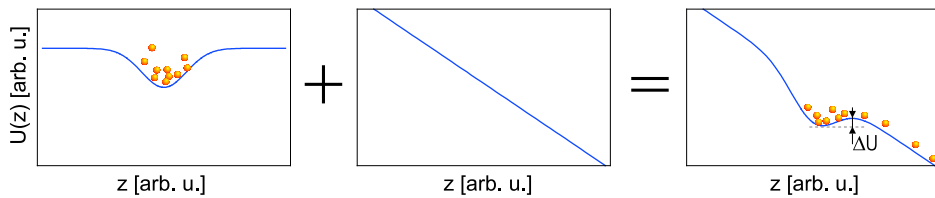


Figure 1.2: Linear gravity potential (central graph) opens the trap and leads to the losses of particles.

1.3.3 Limited trap flatness

It is obvious that a shallow trap is more affected by the gravity³. In the limiting case the gradient of the trapping potential is nowhere larger than the

³For the magnetic trap used for the purpose of this thesis the effect of gravity is quantitatively discussed in section 3.2.4 (Fig. 3.12).

gravitational force and the potential minimum does not exist. Typical harmonic trapping frequencies in the earthbound experiments are of the order of tens of Hz. Leanhardt *et al.* [Leanhardt et al., 2003] used a sophisticated levitation technique to compensate the gravity. They managed to adiabatically reduce the average trapping frequency to $\bar{\omega} = 2\pi \times 1.12$ Hz and reached a sample temperature of 500 pK.

Advantage of the free-fall environment is the possibility to use weaker confining forces on the atoms without the need of (noisy) levitational fields to compensate for the gravity. Sub-Hertz trapping frequencies and the corresponding temperatures in the femto-Kelvin range could be easily realized in space. Decompression of the trap is motivated by the need to slow down the expansion of atoms released from the trap. The expansion speed depends on the initial energy and thus on the trapping frequency. As an example, absorption images of the BEC released from traps with different curvatures are shown in figure 1.3. Both pictures were taken after 50 ms of the free expansion, a time hardly achievable on the Earth. Obviously the matter wave released from the shallower trap spreads much slower.

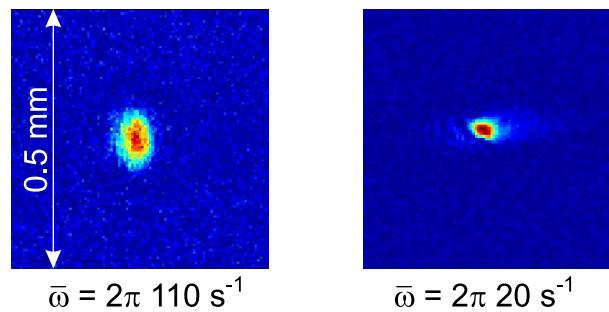


Figure 1.3: Absorption images of a BEC released from traps characterized by the average harmonic trapping frequency $\bar{\omega} = 2\pi \times 110 s^{-1}$ (left) and $\bar{\omega} = 2\pi \times 20 s^{-1}$ (right). Both pictures were taken after 50 ms of the free expansion.

1.4 Advantages of the space environment

”From Quantum to Cosmos” - the title of this chapter - is the name of an international workshop on the space-based research in fundamental physics and quantum technologies. The meeting was first held at the Airlie Center in Warrenton, Virginia on May 2006 and has since that time become an yearly event. Its main scope is to demonstrate if (and how) the laboratory experiments in space can provide the knowledge needed to address outstanding

questions at the intersection of physics and astronomy.

There are two approaches to the physical research in space: one can detect and study signals from remote astrophysical objects or one can perform carefully designed in-situ experiments. The two methods are complementary and the latter has the advantage of utilizing a well-understood and controlled laboratory environment in space. Currently available technologies in conjunction with existing space capabilities offer unique opportunities to take advantage of the variable gravity potentials, large distances, and high velocity and acceleration regimes accessible in space. Furthermore, space is an ideal low noise environment for high precision measurements. As a result, new techniques in quantum physics can achieve their full measurement potential in space and therewith address some fundamental questions. Two of these tools: astoundingly accurate atomic clocks and matter-wave interferometers based on ultra-cold atoms have already been recognized as certain candidates for a space mission and therefore they will be briefly introduced here.

1.4.1 Atomic clocks

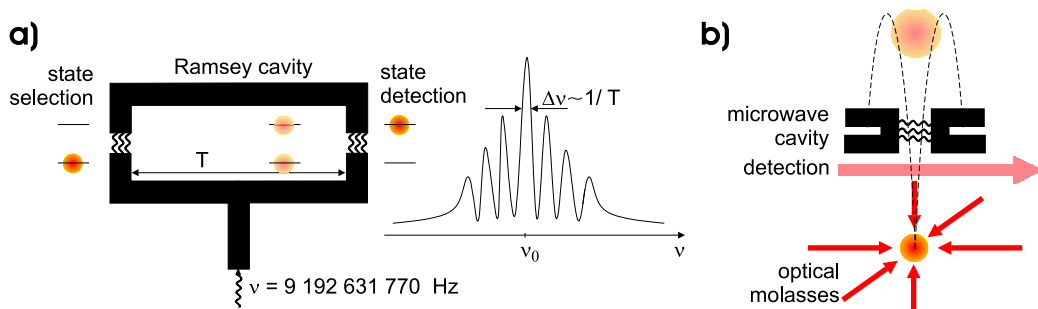


Figure 1.4: a) *Cs beam clock*; b) *fountain clock*

Atomic clocks are the most accurate time and frequency standards known (see [Sullivan et al., 2001] for a review). They use an atomic resonance frequency as the timekeeping element. The radio frequency from a short-time very stable source is synthesized in a frequency chain and tuned near the resonance of a two-level atom. The atomic resonance curve is probed and used to stabilize the source frequency to the peak of the resonance. The narrower the resonance curve the more precise the clock will work. Since 1967, the second is defined as the duration of 9 192 631 770 periods of the radiation corresponding to the transition between the two hyperfine levels of the ground state of the ^{133}Cs atom. Since both levels involved do not

decay, the width of this transition is determined by the time the atoms spend in the radio-frequency interaction zone. The method proposed by Ramsey [Ramsey, 1990] contributed a major improvement to the clock performance. In Ramsey's method the microwave excitation occurs in the two spatially separated zones, that are driven in phase (Fig. 1.4 a)). The width of the resonance is inversely proportional to the time T the atoms need to cross the area between the two zones. In modern clocks with the fountain geometry (Fig. 1.4 b)) there is only one microwave cavity and the Ramsey excitations are separated temporarily rather than spatially. Laser cooled atoms are launched upwards and they cross the interaction zone twice, once on the way up and once on the way down.

Cesium- and rubidium-fountain clocks belong nowadays to the most accurate frequency standards. The best fountains have a relative frequency instability of only a few parts in 10^{16} [Santarelli et al., 1999]. The separation time T between the two excitations is up to 0.7 s and the resonance linewidth is about 1 Hz [Sullivan et al., 2001]. T increases only as the square root of the fountain height H . Therefore to reduce the clock linewidth by one order of magnitude one would have to construct a fountain with a height of 100 m, which is unrealistic with respect to some technical aspects such as compensation of the residual electromagnetic fields. In space, on the other hand, separation times T of several seconds could be easily realized with a simple and compact device giving the resonance width of 0.05 Hz [Laurent et al., 1998].

Another point is that for the fountain frequency standards the transverse temperature of the atoms is a key parameter. During the flight of the atoms through the device, a large fraction of them (usually 90%) gets lost before they return to the detection region (Fig. 1.4 b)). In contrast, the wavefunction of a Bose-Einstein condensate spreads much slower and nearly 100% of the initial number of atoms can still be visible after 1 s of expansion (Fig. 1.7). Due to their high densities, the condensates suffer from the collisional level-shift and therefore have not been used in the atomic clocks so far. However, after several tens of ms, the density of the expanding condensate decreases to a level that is comparable to that in a fountain clock based on thermal atoms. Moreover, the collisional shift in Rb is 50 times smaller than in Cs [Sortais et al., 2000]. This makes the Rb-BEC a potential candidate to drive the future clocks in space with separation times T of several seconds.

1.4.2 Atom interferometers

Atom interferometers use most commonly optical fields to coherently split and recombine de Broglie matter waves. In the particle picture, each atom is

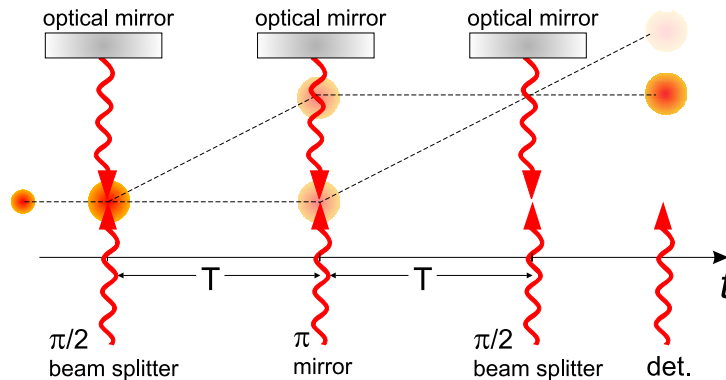


Figure 1.5: Scheme of a basic Mach-Zender type atom interferometer in the absence of gravity

placed into a superposition of two momentum states, that separate spatially in time. Each of these states accumulates a quantum-mechanical phase. If they are brought back together, the phase difference between the two arms of the interferometer leads to the occurrence of an interference pattern.

Figure 1.5 shows schematically a common interferometric sequence. The Raman two-photon transition transfers the atom to the other internal ground state and simultaneously changes the momentum of the center-of-mass of the atom's wave function. This process is coherent and can be performed with any efficiency between 0 and 100% depending on the duration of the Raman pulse. In particular the $\frac{\pi}{2}$ (π) pulse changes the atomic state with 50% (100%) probability and thus acts as a beam splitter (mirror). A combination of $\frac{\pi}{2} - \pi - \frac{\pi}{2}$ pulses forms a basic Mach-Zender interferometer. At the end of the sequence the probability to find the atom in one of the states depends on the phase difference $\Delta\phi$ which, among other things, depends on the gravitational acceleration g and the square of the time separation T between the Raman pulses:

$$\Delta\phi = \frac{m}{\hbar} v_{rec} g T^2 \quad (1.5)$$

with the atomic mass m and the photon recoil velocity v_{rec} .

Atom interferometers do not merely demonstrate the wave nature of matter. Due to their unprecedented sensitivity to external forces, they are widely used as inertial sensors in a variety of measurements, whose accuracy is comparable to, or better than the competing measurements using macroscopic objects. Currently the best known interferometric measurement of g has been performed with an absolute uncertainty of $\Delta g/g \approx 3 \times 10^{-9}$ after one minute of integration time and 1×10^{-10} after two days [Peters et al., 1999, 2001].

The geometry of the cold atoms gravimeter resembles that of the fountain

clock - the atoms are launched vertically - and thus, similar restrictions are put on the maximum height of the setup. Therefore, the interrogation time T is limited by the free fall of the cloud in the vacuum tube. Since the sensitivity of an interferometric measurement scales with the square root of the number of detected particles, low density of the expanding cloud is also a limiting factor. In microgravity T could be easily increased to a few seconds gaining two orders of magnitude in the sensitivity. Nevertheless, it will still be possible to detect the atoms due to much slower expansion of the ultra-cold samples achievable in space.

1.4.3 Benefits for the fundamental research

Two great theories of 20th century, the quantum mechanics and the general relativity, have no common ground: there has been no successful quantization theory of gravity so far. Almost all modern theories searching for the unification of gravitation with the three other fundamental interaction types, assume violations of Einstein's equivalence principle (EEP). Some theoretical studies [Lämmerzahl, 2006; Damour and Polyakov, 1994] predict these violations to be in the range 10^{-13} to 10^{-21} , which could be measurable in the near-future experiments. This motivates for trying to improve the accuracy of various experimental tests of EEP by several orders of magnitude.

EEP, which is a foundation of the general relativity, includes the local position invariance stating that in all local freely falling frames, the outcome of any nongravitational experiment is independent of where and when in the universe it is performed. One consequence of this statement is the time constancy of all nongravitational fundamental constants, such as the fine structure constant α . Another implication is the gravitational redshift of the clock frequency $\Delta\nu/\nu_0 = \Delta U/c^2$, where c is the vacuum speed of light and ΔU is the difference in Newtonian potential between the actual location of the clock and a reference value for which the clock frequency is ν_0 . This shift should be independent of the atomic species involved as a reference in the clock. Finally, the local position invariance imposes that all bodies, regardless of their internal composition, fall in the gravity with the same acceleration. This effect, probably the most familiar issue of the EEP, is also known as Einstein's weak equivalence principle (WEP) or as the equivalence of the inertial and the gravitational mass.

All three above mentioned consequences of the EEP have come under precision tests searching for a tiny deviations from Einstein's predictions. To give a few examples, the analysis of the Oklo natural nuclear reactor showed that two billion years ago α did not differ from the present value by more than a few parts in 10^{-7} [Damour and Dyson, 1996]. A similar upper bound

on a possible fractional time variation of the quantity $(\mu_{Rb}/\mu_{Cs})\alpha^{-0.44}$, where $\mu_{Rb,Cs}$ are the magnetic dipole moments of rubidium and cesium respectively, has been measured by comparing the hyperfine frequencies of ^{133}Cs and ^{87}Rb using atomic fountain clocks [Marion et al., 2003]. On the other hand, observation of the spectra of distant quasars indicates that α differed in the early universe from the present value by $(-7.2 \pm 1.8) \times 10^{-6}$ [Webb et al., 2001]. This until now unexplained discrepancy could be further explored with high-precision clocks in space.

Measurements of the gravitational redshift can also benefit from enhanced accuracy of the space clocks. The accuracy of atomic clocks has recently improved to the point at which it has become possible to measure the gravitational redshift on Earth over an altitude of one meter. The best up-to-date redshift measurement has been performed in 1976 with an H-maser by the NASA Gravity Probe A rocket [Vessot and Levine, 1979; Vessot et al., 1980]. Predictions of the general relativity have been confirmed at the 2×10^{-4} level of accuracy. In another experiment [Bauch and Weyers, 2002] a cesium fountain has been compared to an H-maser in a varying gravitational potential caused by the Earth's annual elliptical motion around the sun. A possible frequency variation of the two standards has been estimated to be less than $2 \times 10^{-5} \Delta U/c^2$.

Since the famous drop attempts of Galileo Galilei in the late 16th century, the weak equivalence principle has been most commonly tested with macroscopic objects including celestial bodies. Laser lunar ranging [Williams et al., 2004] provides currently the most sensitive test of the WEP with the precision of 3×10^{-13} . An even more precise test is planned within the STEP mission (Satellite Test of the Equivalence Principle) [Sumner, 2004]. This cryogenic instrument will contain four pairs of macroscopic proof-mass cylinders freely falling inside a satellite. STEP aims at 1 part in 10^{18} sensitivity.

However, unprecedented precision of atom interferometers will soon lead to laboratory tests of general relativity at levels exceeding those reached by macroscopic bodies and astrophysical observations. One kind of such tests is basing on a comparison of the effect of gravity on macroscopic bodies and on single atoms. So far the most precise measurement of this kind has been performed by A. Peters and S. Chu [Peters et al., 1999, 2001]. The authors measured the difference between the value for g obtained by a falling corner-cube optical interferometer and atomic Cs interferometer to be $(7 \pm 7) \times 10^{-9}g$. Another sort of experiments deals with microscopic objects only. In an interferometric experiment done by the group of T. W. Hänsch [Fray et al., 2004] the gravitational acceleration of the two isotopes ^{85}Rb and ^{87}Rb was compared, yielding a difference $\Delta g/g = (1.2 \pm 1.7) \times 10^{-7}$. In the same experiment a free fall measurement of atoms in two different spin

states was performed, giving a result of $\Delta g/g = (0.4 \pm 1.2) \times 10^{-7}$. The most promising experiment of this kind has been recently proposed by the Stanford group of M. Kasevich [Dimopoulos et al., 2007]. With the worldwide highest atom interferometer ($H \approx 10$ m, $T = 1.34$ s) it should be possible to initially test the equivalence principle to 1 part in 10^{15} and 1 part in 10^{17} in the near future. Interferometers in space could further break these limits.

1.5 Existing cold atom platforms in micro-gravity

1.5.1 Experiments in the parabolic flights

The first cold atoms experiment under the condition of reduced gravity is dated to 1993 by Lounis *et al.* [Lounis et al., 1993]. The authors observed cesium atoms released from a magneto-optical trap and ballistically expanding for 0.2 s. This simple experiment demonstrated that the fragile optical equipment for the laser cooling can be constructed portable and capable of being used under high-vibration conditions. The free falling reference was provided by a jet plane executing parabolic flights. During such a flight the gravity level is reduced to less than 2×10^{-2} g for about 20 s. Up to 30 successive parabolas can be made during one flight.

Another French collaboration I.C.E. (Interférométrie Cohérente pour l'Espace) aims at the construction of an atom interferometer for inertial sensing in microgravity [et al., 2006a]. A compact and transportable apparatus has been designed to be used during the parabolic flights. A mixture of quantum degenerate gases, bosonic ^{87}Rb and fermionic ^{40}K will be trapped in a crossed optical dipole trap. Subsequently a series of Raman light pulses will be implemented to form the beam splitters and mirrors for the matter wave interferometer. The I.C.E. interferometer should serve for the acceleration measurements. Currently the lasers and the vacuum system are under tests [et al., 2006a]. Acceleration fluctuations (vibrations) of up to 2×10^{-2} g during the parabolic flight have been identified as the main drawback limiting the sensitivity of the interferometer. Therefore implementation of a vibration-isolation system is required.

1.5.2 ACES / PHARAO

ACES: Atomic Clock Ensemble in Space is a project selected by the European Space Agency (ESA) to fly on the International Space Station (ISS). The payload of ACES includes two atomic clocks: a hydrogen maser and a

cold cesium atom clock PHARAO (Projet d'Horloge Atomique à Refroidissement d'Atomes en Orbite). The relative frequency stability of the PHARAO clock on board the ISS is expected to be better than 10^{-13} for one second measurement time and 3×10^{-16} for one day. Target accuracy is 10^{-16} .

The goal of the ACES mission is to operate the two kinds of atomic clocks and to make a direct frequency comparison between them on board the ISS. Moreover, frequency comparison between PHARAO and the ground clocks should be performed with a relative accuracy of 10^{-16} , a factor of 100 better than the best current GPS measurements. These features will give rise to increased precision of some fundamental physics test. The gravitational redshift, for example, will be measured with a 3×10^{-6} accuracy. This is a 25-fold improvement compared to the measurement of the Gravity Probe A mission. Another scientific objectives of ACES include the search for a possible time variation of the fine structure constant as well as an improved test of special relativity. For a review of the ACES mission see reference [et al., 2001].

Concerning the technology readiness for the operation in microgravity, PHARAO is up-to-date the most advanced among the cold atoms projects for space. The satellite version of PHARAO, developed by the French Space Agency (CNES) has entered the industrial development in June 2001. The clock is currently being characterized on the Earth and tested in the reduced gravity environment of the parabolic flights. The details of design and the first test results of the PHARAO clock can be found in reference [et al., 2006b].

1.5.3 QUANTUS

The QUANTUS (Germ.: Quanten Gase unter Schwerelosigkeit) project joined the space-oriented cold atom research community in spring 2004. The members of the collaboration are the Institutes of Physics from the Universities of Hannover, Ulm, Hamburg, Bremen (ZARM), and the Humboldt University of Berlin, as well as the Max-Planck Institut für Quantenoptik in Garching. The project is supported by the German Space Agency (DLR) with funds provided by the Federal Ministry of Economics and Technology (BMWi) under grant number DLR 50 WM 0346.

Targeting the long-term goal of studying cold quantum gases on a space platform, we currently implemented a ^{87}Rb BEC experiment under microgravity condition at the drop tower facility of the Center of Applied Space Technology and Microgravity (ZARM) in Bremen. The Bremen drop tower offers a significant compensation of the Earth gravity down to the 10^{-6} g level. Duration of microgravity is 4.5 s in the drop-mode and it can be doubled when using the catapult. This time is fairly enough for prelimi-

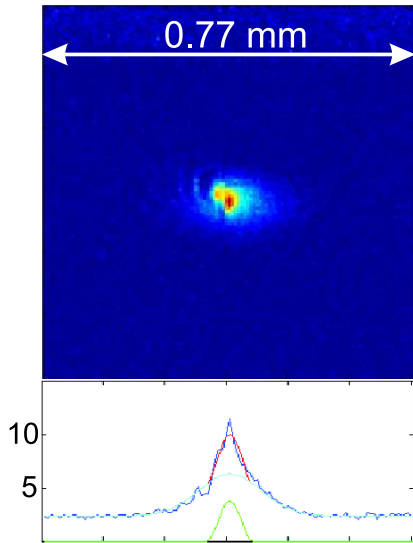


Figure 1.6: *The first BEC realized in microgravity. Absorption image taken after 16 ms TOF. Color scale represents variation in the optical density and the lower graph is integrated optical density along the vertical axis. The condensed part is fitted with an inverted parabola (green) and the residual thermal background with the Gaussian (cyan). From the fit we read $N \approx 6000$ condensed atoms.*

nary experiments aiming at the preparation and subsequent observation of the ultra-cold freely falling matter waves. The possible free expansion time of up to 7 seconds represents a gain of factor 100 compared to earthbound experiments.

Within 3 years from the beginning of the project we have designed, built and extensively tested a compact and robust BEC setup suitable for the operation in the drop tower. Special challenges in its construction were posed by a low volume of the drop capsule ($<1 \text{ m}^3$) as well as critical vibrations during capsule release and peak decelerations of up to 50 g during recapture at the bottom of the tower. All mechanical, optical and electronic components have thus been designed with stringent demands on miniaturization and mechanical stability. Additionally, the system provides remote control capability as it is not manually accessible during the drop. To the best of our knowledge the setup described in chapter 2 is, up-to-date, the only portable BEC apparatus worldwide.

For the sake of chronological completeness, the first laboratory Bose-Einstein condensation with the Quantus drop capsule was realized in February 2007. In that year in October we dismantled the setup almost completely and moved from Hannover to Bremen. Just one day after, we were able to reproduce the results from Hannover, which can also be seen as a kind of world record in the speed of a complete rearrangement of a quantum optics experiment. This demonstrates the high flexibility and reliability of our hardware.

On 06.11.2007 we succeeded in the first realization of the BEC in microgravity (Fig. 1.6). Since that time we have performed over 160 successful

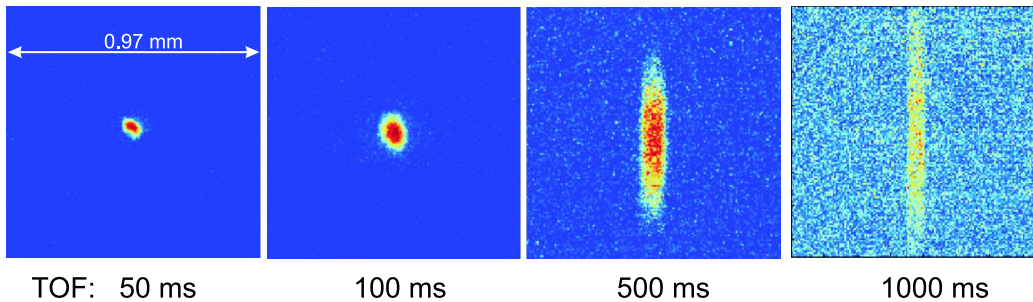


Figure 1.7: Absorption images of the BEC for TOFs 50, 100, 500 and 1000 ms.

drops. The experiment has been optimized to increase the number of atoms in the BEC to roughly 10^4 . The trap steepness has been systematically reduced so that during the last drop campaign we worked with the mean trapping frequency $\bar{\omega} = 2\pi \times 10.9(\pm 1)$ Hz. Note that this trapping frequency is not available in any earthbound experiment without levitation. Finally, we increased the time of free evolution to the unprecedented 1 second! (Fig. 1.7). After 1 s the size of the BEC reaches 1 mm with the peak density $3 \times 10^7 \text{ cm}^{-3}$. By an average expansion speed as low as 1 mm/s, all condensed atoms are expected to remain within the view field of the camera for 5 s. However, further increasing of the expansion time is currently limited by the low initial number of atoms in the condensate and a poor signal to noise ratio by the detection. The work to reduce the trapping frequencies to the sub-Hz regime is currently in progress.

1.6 Composition of this thesis

The results described in this thesis is an effect of a collaborative effort of the whole QUANTUS team. The author's contribution to the teamwork includes the design, assembly, characterization and drop tower tests of the complete laser system, including the relevant electronic components. After the completion of all individual components of the experimental setup the author took actively part in their integration into the drop capsule. Afterward he assisted by the most relevant project-milestones, like the generation of the BEC in laboratory, moving the setup to Bremen and operating it at the drop tower, finally by the first realization of the BEC in free fall. Furthermore, calculation and characterization of the time dependent trapping potential was done by the author. Simulation of the time evolution of the Boes-Einstein condensate wave function in this potential followed in close cooperation with

the theoretical group in Ulm.

The experimental setup is described in detail in chapter 2. Since the drop tower environment is to a large extent similar to that of a space platform, special emphasis is put on the strict requirements on the experiment to make it drop-tower-qualified.

The central part of the setup is the magnetic micro trap (atom-chip). Its principle of operation, characteristic of generated magnetic field and possible design modifications are the issues of chapter 3.

Chapter 4 contains a complementary, quantitative discussion of the results. It begins with a theoretical treatment of the time dependent evolution of the condensate wave function. An analysis of the time variation of the trapping potential, which drives the evolution of the condensate, follows. Finally, a detailed analysis of the result sketched in figure 1.7 is given in that chapter.

Last, the near future perspective including both further steps with the existing setup and the next generation of the Quantus experiment is briefly illuminated in chapter 5.

Chapter 2

Cold atom experiment at the Drop Tower in Bremen

2.1 The drop tower Bremen

The Bremen drop tower is a facility of the Center of Applied Space Technology and Microgravity (ZARM¹) at the University of Bremen. The research is concentrated mainly on the investigation of fluid mechanics phenomena under microgravity conditions and questions related to space technology. Within the scope of QUANTUS, the first quantum physics experiment at ZARM, the properties of a freely falling Bose-Einstein Condensate have been regularly investigated since November 2007.

The tower has a total height of 145 m and provides the possibility to drop experiments inside an evacuated steel drop tube (Fig. 2.1) with an altitude of over 100 m. This allows for approximately 4.7 s free-fall time, which can be doubled if one launches the experiment with a catapult. There are two basic reasons for evacuation of the drop tube. The first is to reduce the air friction during the drop. Second, friction in the deceleration container leads to the accumulation of electrostatic charge on the cover of the capsule. The presence of oxygen could lead to ignition and consequently to a flame. Evacuating the tube takes 2 hours on average and is one of the main factors limiting the repetition rate of the experiment to 3 drops per day. Weightlessness (or zero-g) is only an idealized state that does not exist. In fact any experiment is exposed to residual accelerations: those induced by the mass distribution of the experiment itself, and those caused by the residual vibrations of the experimental apparatus. The residual accelerations (microgravity quality) during the flight are as low as 10^{-6} to 10^{-5} g in the acoustic Fourier frequency

¹Germ.: Zentrum für angewandte Raumfahrttechnologie und Mikrogravitation

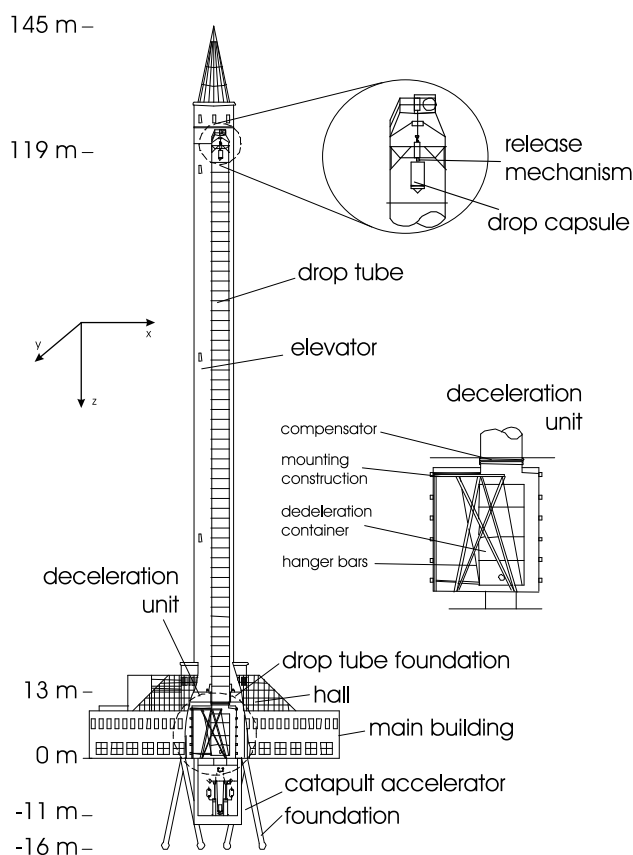


Figure 2.1: Cross-section of the drop tower in Bremen (figure from reference [Dro, 2007]).

range 0-500 Hz (Fig. 2.2). The velocity dependent DC deceleration caused by air friction is of the order of 10^{-5} g at the end of the flight (measured at the residual pressure in the drop tube of <20 mbar [Sellig, 2007]). This μ -g level is the best one amongst the microgravity facilities and is reached already after 1.5 s after capsule release or after 2 s after catapult launch (for a more detailed analysis of the acceleration in the capsule see the *Drop Tower Bremen User Manual* [Dro, 2007]).

At the bottom of the tower the freely falling drop capsule has a velocity of 166 km/h when it is captured in a deceleration unit. The deceleration container has a height of 5 m and is filled with polystyrene pellets. Despite of the macroscopic (5 mm) diameter of the granulate, the dynamics of the capturing process resembles that of submerging in a viscose fluid. The measured acceleration in vertical direction is shown in figures 2.3 and 2.15. The duration of the impact is 200 ms with an average deceleration value of approximately 25 g. The peak value of the impact deceleration reaches 50 g and

puts one of the most stringent requirements on the mechanical stability of the experimental setup. Note also the residual vibrations at the moment of capsule release (at $t = 0$). The release mechanism has been designed and revised over the years in order to achieve a smooth 1 g - 0 g transition. Nevertheless, the gravitationally induced mechanical tension of the composite elements of the drop capsule is released in microgravity. This excites eigenoscillations of the capsule elements (mainly flat payload platforms) which might affect the stability of the laser system.

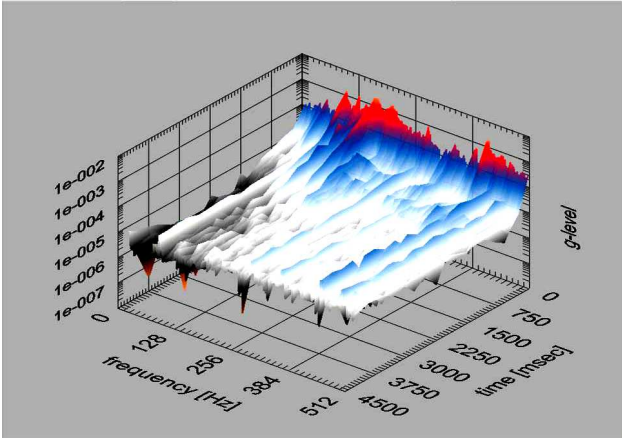


Figure 2.2: Time dependent Fourier spectrum of the residual acceleration (microgravity quality) inside of a falling capsule (figure from reference [Dro, 2007]).

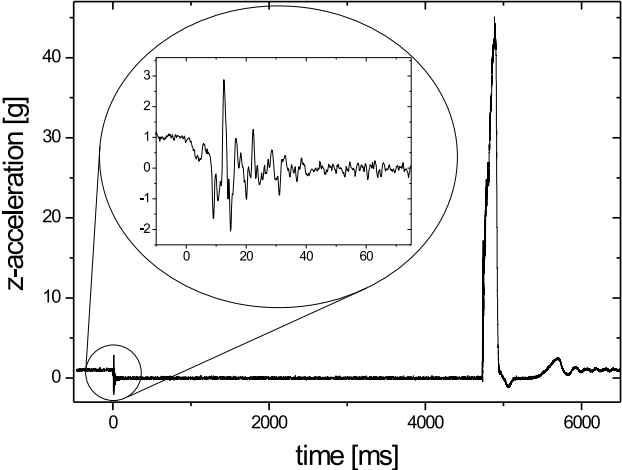


Figure 2.3: Acceleration in the z -direction in units of g measured inside of a falling capsule

2.2 Requirements on the experiment

The long-term goal of the QUANTUS collaboration is to establish an experimental platform in space to allow the investigation of ultra-cold quantum matter in free fall for unlimited time. The drop tower environment is similar to that of a space platform in several aspects. In particular, strict requirements concerning the limited volume, low power consumption, and high mechanical stability of the components have to be fulfilled. Thus, special technical challenges in the construction of the experimental setup make it different from common earthbound systems to a large extent. In detail, as specified in [Vogel et al., 2006], the following points have been crucial for the design of all mechanical, optical, and electronic modules:

- **Miniaturization** Optics for a common laboratory BEC experiment usually fills the area of the whole optical table. Roughly the same space above the table is required for the electronics. In contrast, our setup has to fit into the drop capsule, the volume of which is less than one cubic meter (Fig. 2.4 a)) with a surface of a single payload platform of 0.36 m^2 (Fig. 2.4 b)).

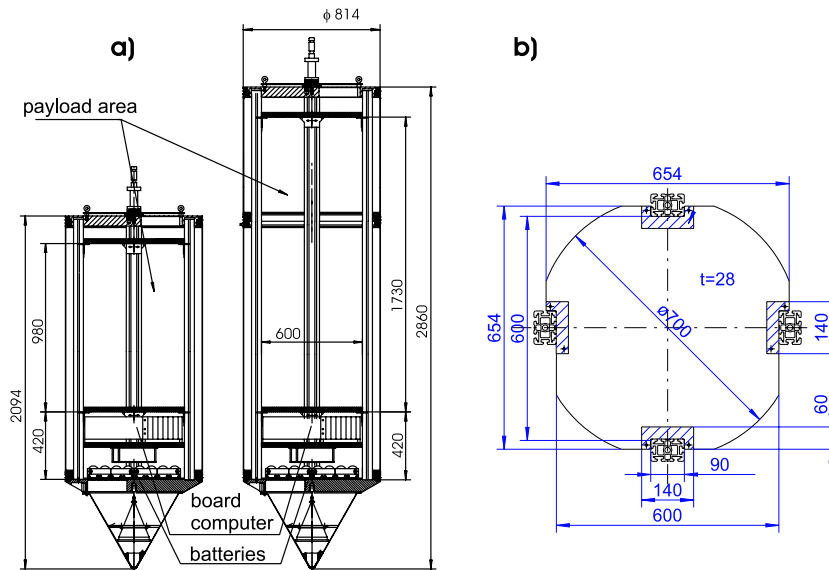


Figure 2.4: a) Two available versions of the drop capsule and b) the payload platform (figures from reference Dro [2007]).

- **Low mass** In all space missions weight is an important factor in terms of launch costs. The drop capsule can carry a maximum payload of

Table 2.1: *Dimensioning of the drop capsules*

parameter: \ capsule version:	short	long	catapult
stringer length [mm]	1545	2310	1342
max. payload height [mm]	980	1730	950
total area of experiment-platform [m ²]	0.36	0.36	0.36
base structure incl. batteries and computer [kg]	110	110	122.7
top lid plate [kg]	36	36	28.2
vacuum sealed cover incl. clamping rings [kg]	32	54	38.5
4 stringer [kg]	42	60	36.6
nose cone incl. connection rod [kg]	6	6	10.2
1 experiment-platform incl. brackets [kg]	15.2	15.2	15.2
capsule net weight [kg]	226	266	236.2
capsule gross weight [kg]	500	500	400
max. payload mass [kg]	274	234	163.8

234 kg. All masses and dimensions of the drop capsules (including the catapult version) are summarized in table 2.1. Note that more stringent demands on size and weight are put on the catapult capsule.

- **Low power consumption** Electrical power for the experiments in the drop tower is supplied from batteries placed at the bottom of the drop capsule. They operate at 28 V DC voltage and can provide a total energy of 0.56 kWh with a peak power of about 3 kW. Obviously, there are even stronger energy constraints on the space platform.
- **High mechanical stability** Residual vibrations of the platforms at the moment of capsule release can be critical for the laser frequency and light intensity stability. Moreover, all the components used have to withstand the peak deceleration of up to 50 g during impact and catapult launch. Due to the maximal drop rate of three times per day, there is only less than one hour for likely corrections and readjustment of the setup between the flights. Therefore, a permanent misalignment of the experiment after each drop should be avoided. Fulfilling this requirement would also be important in future space missions because of the presence of violent shocks and vibrations during the launch phase.
- **Thermal insensitivity** Whilst the drop or launch take place in the evacuated drop tube, the capsule is vacuum-tight and there is normal pressure inside of it. Most of the electronics remain turned on during drop tube evacuation, which results in a temperature increase in the

upper parts of the capsule of up to 4 degrees within 2 hours. The components of the experiment which are highly sensitive to temperature change (e.g. the optical rack with fiber docks) are therefore required to have connection to water cooling circuit.

- **Fast BEC preparation** In order to damp the effect of the above mentioned vibrations, the atoms are kept in the non-conservative magneto-optical trap (MOT) during the capsule release and 1 s thereafter. Thus, all following cooling phases, in particular the evaporation in the magnetic trap, have to be faster than the total drop time of about 4.7 s minus the free expansion time of up to 1 s.
- **Remote control** Two hours before the drop, while the drop tube is evacuated, the experiment is accessible only via remote control. In particular, one has to be able to lock the lasers to an adequate atomic transition without manual access.

In the following section the experimental setup will be described in detail, emphasizing how it addresses the above issues.

2.3 Quantus experimental setup

Nowadays Bose-Einstein condensates can be nearly routinely produced in many optical laboratories and a number of different experimental techniques are being extensively discussed in the literature [Metcalf and van der Straten, 1999; Phillips, 1998; Ketterle et al., 1999]. The main requirements are, however, similar. The most important are: good thermal decoupling from the environment using contact-free storage in ultra-high-vacuum chambers (typically better than 10^{-10} mbar) and a sophisticated two-stage trapping and cooling process. The latter begins with precooling using Doppler- and sub-Doppler laser cooling in a magneto-optical trap down to the temperatures in the μK range. Subsequently, the cold atomic sample is transferred to a conservative trapping potential (magnetic or optical) and cooled further by evaporative cooling.

2.3.1 Drop capsule overview

The QUANTUS drop capsule with its components is depicted in figure 2.5. The heart of the experiment is the vacuum chamber which houses the magnetic chip-trap. The uppermost platform is occupied by the complete laser system (including the laser electronic rack) and the remaining space is tightly

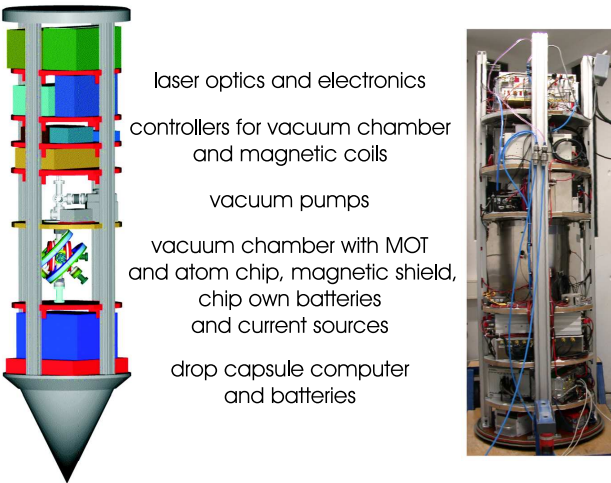


Figure 2.5: Quantus drop capsule with its composite modules.

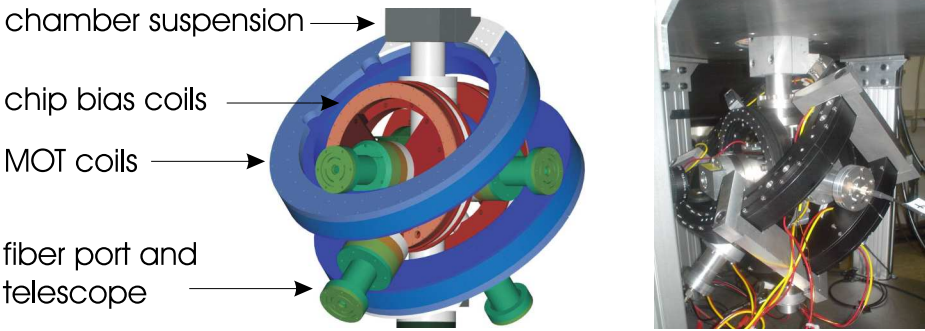


Figure 2.6: Vacuum chamber with magnetic coils and fiber telescopes rigidly attached to the chamber body (left drawing courtesy of Tim van Zoest [van Zoest, 2008]).

filled with control electronics. It is worth to mention that QUANTUS is the heaviest experiment ever dropped at ZARM. The total weight of the drop capsule slightly exceeds the maximal allowed mass of 500 kg.

2.3.2 Vacuum

The atoms are trapped inside of a non-magnetic, stainless steel, ultra high vacuum chamber, which is kept at ultra low pressure of less than 10^{-10} mbar by an ion getter pump (25 l/s) and a titanium sublimation pump. It is important, that there are no moving elements inside either of the pumps

which could be damaged during deceleration of the capsule. In particular, to avoid long-run loosening, all screws inside of the pumps have been spot-welded. Moreover, high voltage elements of the ion pump are fastened with mounts specially designed for operation in the drop tower, that prevent an eventual short circuit of the electrodes. Also, special attention has been paid to the mounting of the filaments of the titanium pump. These are mounted vertically so that they are less sensitive to torques during capsule deceleration.

To minimize mechanical strains that could lead to leakage, there is only a single suspension of the vacuum chamber inside the drop capsule. All peripheral components like magnetic coils, CCD-camera telescopes and fiber ports are rigidly attached to the steel body of the vacuum chamber, giving maximum stability and minimizing possible sources of relative misalignment (Fig. 2.6). A detailed description of the vacuum system, including technical drawings of the chamber and characteristics of the Helmholtz-coils have been given in the PhD thesis of Tim van Zoest [van Zoest, 2008]. A drop tower vacuum-tightness test has been described in reference [Könemann et al., 2007].

2.3.3 Chip trap and mirror MOT

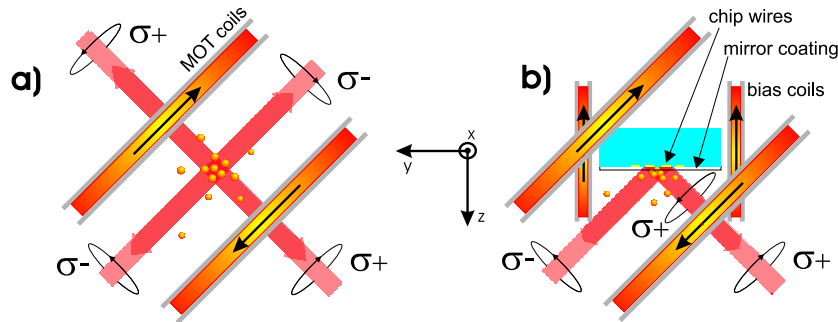


Figure 2.7: a) A common 6-beam MOT and b) 4-beam mirror MOT. The two counter propagating beams perpendicular to the picture plane are not shown. σ^+/σ^- refer to the light helicity, not the polarization.

In order to meet the need of short evaporation times and low power consumption, we use a magnetic micro-trap on a chip [Reichel et al., 2001; Folman et al., 2002]. Its operating principle, the architecture of the strip lines as well as the generated magnetic fields are described extensively in chapter 3. At this point it is worth to point out the key role of the chip in magneto-optical trapping and pre-cooling of the atoms before the magnetic

trap is turned on. An ordinary magneto-optical trap consists of 6 orthogonal, counter-propagating, circularly polarized laser beams, that intersect at the minimum of a quadrupole magnetic field generated by a pair of macroscopic anti-Helmholtz coils (Fig. 2.7 a)). However, this configuration is not applicable in the case of a chip-trap since the chip substrate is not opaque. Instead, the chip surface features a highly reflective dielectric coating and reflects two of the diagonal beams (Fig. 2.7 b)). $\sigma+$ circularly polarized light changes into $\sigma-$ once reflected from a mirror. Therefore in the vicinity of the chip surface, there are pairs of counter-propagating beams with the same helicity but with orthogonal circular polarization seen by the atoms. The quadrupole field for the MOT can be generated either by the external anti-Helmholtz coils or a superposition of an external bias field and a field that is created from a current through the U-shaped wires on the chip (Chap. 3).

2.3.4 Laser system

Requirements on the laser system

In order to keep the setup as simple as possible, we trap ^{87}Rb , which, like other alkali atoms, has a simple laser cooling scheme (Fig. 2.8) for which laser diodes are commercially available. Furthermore, a relatively high ratio of elastic to inelastic collision rate in ^{87}Rb is advantageous for evaporative cooling.

For cooling and trapping ^{87}Rb atoms in a magneto-optical trap infrared laser light ($\lambda = 780.2 \text{ nm}$) is required to drive the D2 transition $5^2S_{1/2} \longrightarrow 5^2P_{3/2}$. All frequencies used in the experiment can be divided into two classes (blue and green arrows in Fig. 2.8) separated by the hyperfine splitting of the ^{87}Rb ground state (6.8 GHz). For atoms with a natural transition linewidth Γ_{nat} , the low intensity theory of Doppler cooling in one dimension yields an optimal detuning of the cooling laser δ that minimizes atomic temperature: $\delta = -\Gamma_{nat}/2$ [Metcalf and van der Straten, 1999]. In 3D and for light sources with a spectral width comparable to Γ_{nat} the optimal detuning is greater than $\Gamma_{nat}/2$. Besides, with increased detuning a larger fraction of atoms from the thermal background can be caught. Also the trap volume increases with δ . Thus, in practice, the optimal detuning δ is of the order of 2-3 Γ_{nat} and its value has to be found empirically as a compromise that gives sufficiently low temperature for a still satisfactory number of atoms. In order to fulfill this demand the spectral linewidth of the laser has to be at least as narrow as Γ_{nat} (6 MHz for the D2 transition in rubidium) and the long-term frequency variance should be much less than that. As shown in reference [Chen et al.,

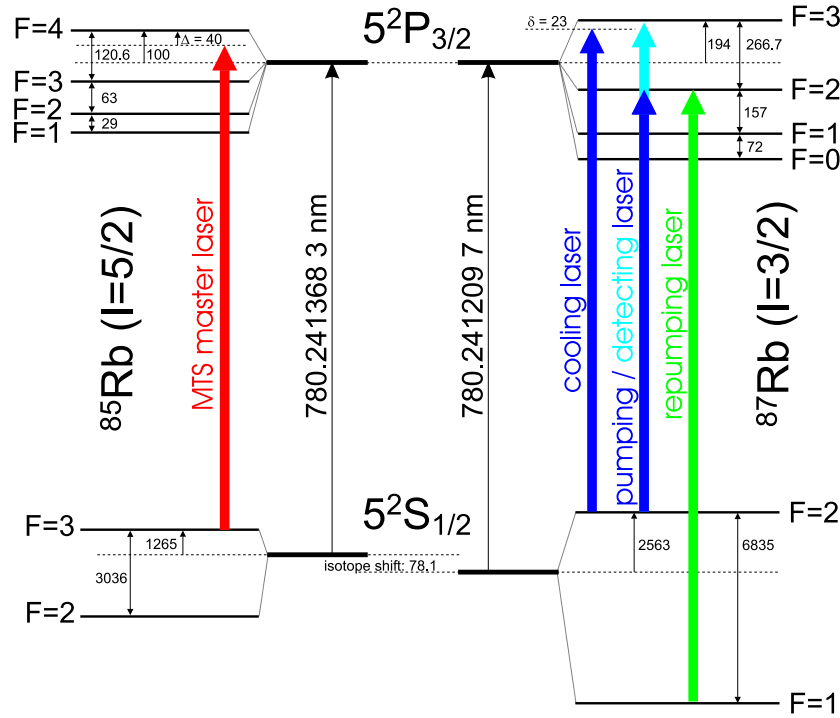


Figure 2.8: Hyperfine splitting of the D2 line in rubidium (all frequencies in MHz) and laser transitions (colored arrows) required for the BEC experiment.

2000] the number of trapped ^{87}Rb atoms in a MOT decreases by a factor of 1.7 when the linewidth of the cooling laser approaches 10 MHz.

A total power of about 50 mW of the cooling light is needed at the atom cloud, while a few mW are sufficient for the other transitions.

Full control over laser frequency and intensity at the moment of capsule release and during the flight are critical parameters that determine whether a satisfactory number of atoms can be trapped at a temperature that is low enough to efficiently load the magnetic trap.

Laser system overview

Our laser system is schematically shown in figure 2.9. It consists of a master laser stabilized to an atomic transition, a MOPA amplifier (Master-Oscillator Power Amplifier), a repumping laser (both frequency-offset locked to the master laser), and a power-distribution and -control module with acousto-optic modulators (AOM-module). Optical connections between those modules and with the vacuum chamber are realized exclusively with single mode polarization-maintaining optical fibers.

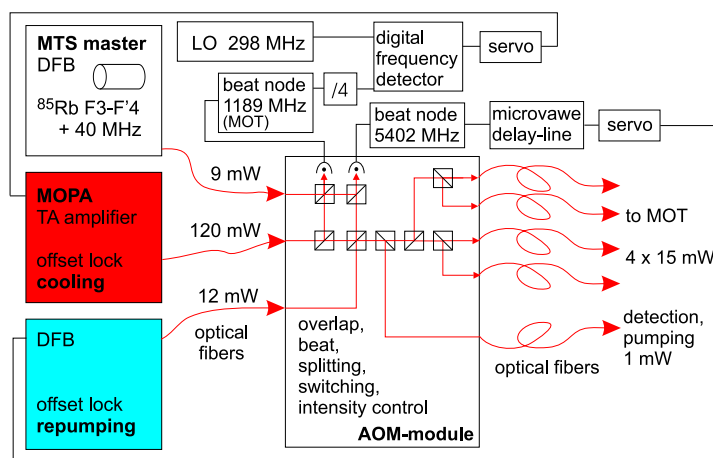


Figure 2.9: Schematic of the laser system. The red lines are light paths and the black are electronic connections.

All mounts for optical elements have a beam height of 20 mm and were designed by us with a special emphasis on mechanical stability. The majority of them are not adjustable. Exceptions are the mirror holders in front of the fibers (Fig. 2.10 right) and beat photodiodes as well as the mirrors used to superimpose two laser beams. In contrast to most commercially available spring-based adjustable mounts, our ultra-stable stainless steel construction makes use of flexure metal sheets for tilting the mirror.

The laser modules are placed in a stable and robust housing ($210 \times 190 \times 60$ mm) made of stress-free aluminum. The three lasers together with the AOM-intensity-control module are integrated into a frame assembly with dimensions chosen to be compatible with a standard 19" electronic rack (Fig. 2.10 left and middle). The laser system including electronics has a total weight of about 45 kg and fits the area of one platform in the drop capsule.



Figure 2.10: Mechanical mount of the laser system. Optic (left) and electronic (middle) racks have the standard width of 19". Mounts for optics with the beam height of 20 mm (right).

DFB diode

For the sake of mechanical stability, we have intentionally excluded the use of extended cavity diode lasers (ECDL) which are otherwise commonly used for laser trapping. Instead, we drive our laser system with distributed feedback (DFB) laser diodes [Caroll et al., 1998], which have an intrinsic grating in the active semiconductor area. Commercially available DFB diodes from Eagleyard (EYP-DFB-0780-00080-1500-TOC03-0000) mounted in a TO3 housing with an internal Peltier element fit well our requirements regarding compactness. Moreover, the diode's emission linewidth is about the same order of magnitude as the natural linewidth of the ^{87}Rb D2 transition.² The linewidth was measured by beating the DFB laser with a spectrally much narrower (< 100 kHz) ECDL laser. The beat signal was subsequently analyzed with three independent methods: fast Fourier transform (FFT), phase-noise analysis and with the use of a spectrum analyzer. An example of the latter is shown in figure 2.11. From the Lorentz fit we obtain a spectral width (FWHM) of 4.7 MHz. The other two methods are described in reference [Schiemangk, 2007] in detail.

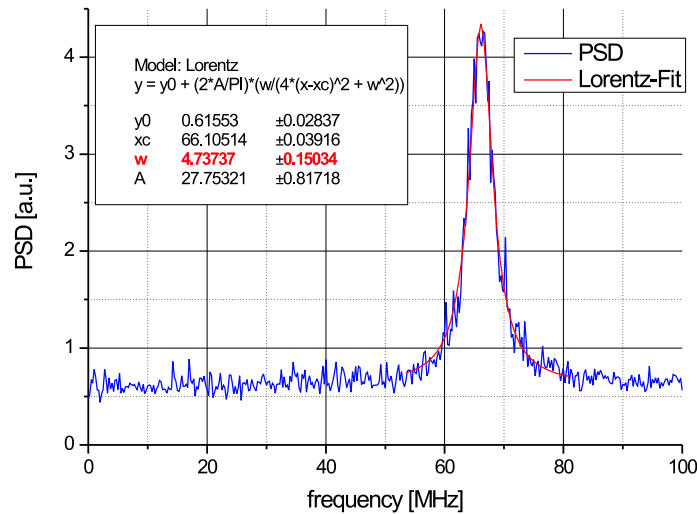


Figure 2.11: Power spectral density (PSD) of a DFB diode measured as a beat signal with an ECDL laser. The resolution bandwidth of the spectrum analyzer was 30 kHz and the sweep time 20 ms.

We stabilize the temperature of the diodes, and use only the current to vary the wavelength. DFB diodes have an extremely wide mode-hop-free operation range of more than 100 GHz, which greatly facilitates their use.

²The manufacturer guarantees a linewidth of less than 10 MHz

Information on rubidium spectroscopy with DFB diode lasers can be found in reference [Kraft et al., 2005].

MTS master laser

The master laser (left picture in figure 2.12) is stabilized to the atomic transition $|5^2S_{1/2}, F = 3\rangle \longrightarrow |5^2P_{3/2}, F = 4\rangle$ in ^{85}Rb (Fig. 2.8). The choice of this particular line is motivated by its largest transition strength among the whole D2 spectrum. Moreover, a relatively high natural abundance (72.1%) of the ^{85}Rb isotope additionally enhances the signal. Light from the master laser does not play any further role in the experiment other than serving as a reliable frequency reference for all other required transitions.

The error signal for frequency stabilization is generated using modulation transfer spectroscopy (MTS) [Shirley, 1982; Zhang et al., 2003]. Similar as in frequency modulation spectroscopy (FM) [Bjorklund, 1979; Bjorklund and Levenson, 1983; Supplee et al., 1994], a part of the laser beam (approx. 1 mW) is split into a weak probe beam and a much stronger pump beam with an intensity that exceeds the saturation intensity of the transition. The two beams counter propagate through the atomic vapor inside the glass cell and the probe beam is detected after passing the cell using heterodyne detection. The resulting signal reveals the sub Doppler structure of the transition. Whereas both beams (or only the probe) are modulated in the case of FM, the pump beam only is modulated in the MTS technique. The modulation is transferred to the probe beam in a nonlinear processes of modulated hole burning and reflection from an induced population grating. The resulting demodulated signal is free of a Doppler broadened background.

Phase modulation of the master laser is done with an electro-optic modulator (EOM) whose resonant frequency is 7.4 MHz. To avoid unwanted interference of the probe beam with a residual back-reflection of the pump beam, the probe beam is frequency shifted with an acousto-optic modulator (AOM) by $2\Delta = -80$ MHz. This leads to a red shift Δ of the laser frequency relative to the atomic transition (Fig. 2.8)

MOPA

The MOPA module (right picture in figure 2.12) has been built by the QUANTUS partner from Hamburg. It consists of a DFB diode that seeds a tapered amplifier (TA, Eagleyard EYP-TPL-0780-01000-3006-CMT03-0000). This TA emits a maximum light power of 1 W at an operating current of 3 A and a maximal seed power of 50 mW. The outgoing beam profile is mode matched to a Gaussian beam profile using a set of cylindrical lenses as described in

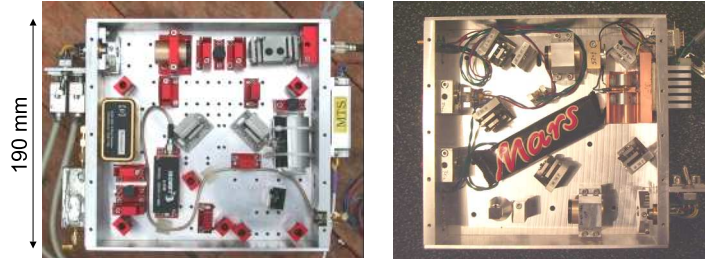


Figure 2.12: *MTS master laser (left) and MOPA module (right) with a gauging stick from the Masterfood company.*

reference [Wilson et al., 1998]. Nevertheless we achieve a maximum fiber coupling efficiency of 40% only. Since TA is not operated at its absolute maximum ratings and the fiber coupling is usually not perfectly aligned, we typically provide 120 mW of cooling light at the output of the TA-fiber, which is fairly enough for our purposes.

Repumping laser

In the early stage of the experiment we stabilized the repumping laser directly to the repumping transition in ^{87}Rb : $|5^2S_{1/2}, F = 1\rangle \rightarrow |5^2P_{3/2}, F = 2\rangle$. For this purpose we used a Doppler-free dichroic atomic vapor laser lock (DFDL) [Wasik et al., 2002]. Its advantage was a very simple construction with a minimum number of optical and electronic components. However, to generate a DFDL error signal retardation optics is required, which is sensitive to temperature variations. Consequently, the long term frequency stability was not satisfactory for drop tower operation (as already mentioned, temperature in the drop capsule varies by up to 4 degrees). At the present, the repumping laser is a single DFB diode coupled to a fiber (12 mW at the fiber output) and offset-locked to the master laser.

AOM-module

Light from the cooling, the repumping and the master laser is provided to the AOM-module (Fig. 2.13 and C.4) via optical fibers. Cooling and repumping beams are superimposed, split into 4 beams of equal intensity³ (15 mW cooling + 0.5 mW repumping) and coupled to the output fibers. Roughly 2 mW of the cooling beam is pinched off for optical pumping to the $|F = 2, m_F = 2\rangle$ state and detection of the atoms. Each of the 3 kinds of the output beams

³So far there has been no necessity to use active stabilization of the light power splitting ratio, however this possibility is considered for the future catapult experiments

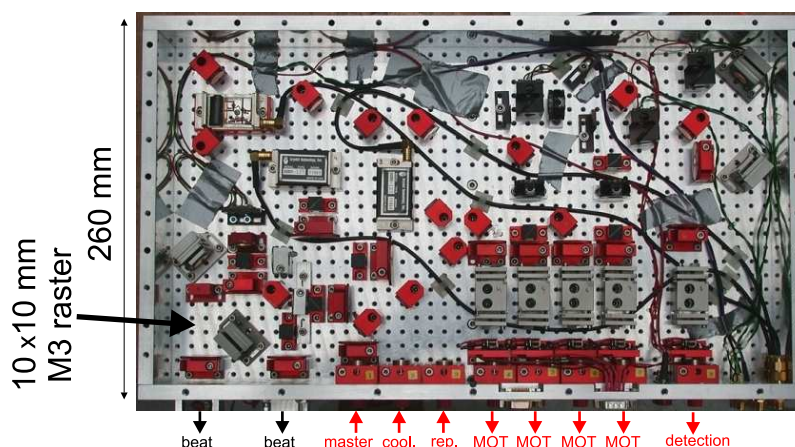


Figure 2.13: *AOM-module.*

goes through an acousto-optic modulator (AOM, Crystal Technology, 3080-125). The AOMs are driven with 32 dBm RF-power, which allows for 85% efficiency of the first diffraction order. The RF-frequency is kept constant (80 MHz)⁴, thus the AOMs are not used to frequency chirp the light. Rather they serve as variable attenuators and fast switches for the light beams. Even if the RF driving the AOMs is off, some residual light might be diffracted and coupled to a fiber. This might give rise to heating of the magnetically trapped condensate. To avoid this, there is a mechanical shutter mounted in front of each outgoing fiber port.

Finally, inside the AOM-module the cooling and repumping beams are superimposed with the light of the master laser and focused on fast photodiodes (Hamamatsu, G4176-03) to record the beat signals needed for the offset lock.

Frequency-offset lock

Both cooling and repumping lasers are frequency-offset locked to the master laser (Fig. 2.9). The idea behind an offset lock is to detect the beat frequency between a reference laser (master) and a laser of interest, and to keep it constant. This is done by converting a high frequency beat signal into a voltage which feeds-back the laser's frequency actuator (laser current in a DFB laser or laser current and piezo voltage in an ECDL). Our two offset lock assemblies differ in the way the beat frequency is converted into voltage. In case of the cooling laser, we use a digital phase-frequency de-

⁴This additional frequency shift must be considered when estimating the offset frequencies.

tector (Hittite HMC440QS16G) with an integrated programmable prescaler (divider). The beat frequency is internally divided by 4 and compared to the reference frequency generated by a 15 bit direct digital synthesizer (DDS, AA-Opto-Electronics). The reference frequency is varied from 291.5 MHz for the resonant detection, 297.25 MHz for the MOT up to 357 MHz for pumping to the $|F = 2, m_F = 2\rangle$ state. Both, detection and the optical pumping take place in the presence of a magnetic field.

Frequency detection for the repumping laser is realized with the so called “trombone”. After amplification, the beat signal (5.4 GHz) is split. One half goes through an adjustable microwave phase shifter (P1506, ATM Inc.). Subsequently the two signals are electronically multiplied (mixed) with a double balanced frequency mixer. If the input frequencies are equal the mixer acts as a phase detector. Its output DC voltage is proportional to the sine of the phase difference of the inputs. This phase shift depends on the input frequency to the trombone phase shifter and one can adjust it in such a way that at the frequency of interest the phase difference is equal to a multiple of π . In this case the output from the mixer is equal zero and changes linearly for small frequency variations, thus it can be used to feed back the laser.

Lock bandwidth

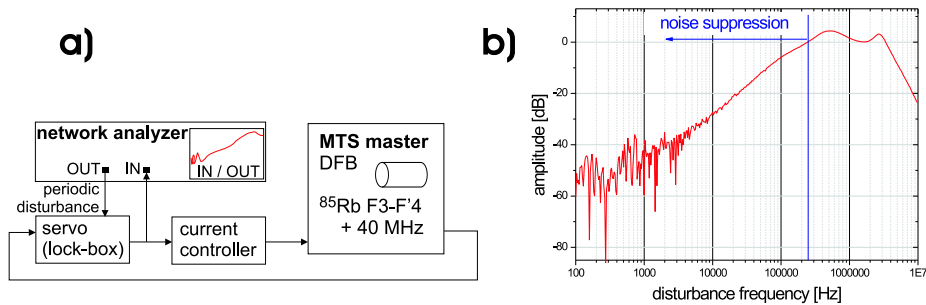


Figure 2.14: a) Schematic of the lock bandwidth measurement setup and b) an example of the measurement with a lock bandwidth of 250 kHz.

Possible laser frequency disturbances during the release of the drop capsule and at the impact are mainly of mechanical origin. This is because residual back reflections (also stray light) from the surface of optical elements placed in front of the Faraday isolator may feed back the laser diode. Critical elements mounted before Faraday isolator are for example the diode housing window, collimating lens and the entrance window of the isolator

itself. To give a numerical example, moving one window of a 5 cm long parasitic resonator by just 1 nm is enough to shift the laser frequency (at $\lambda = 780$ nm) by 8 MHz, which is more than Γ_{nat} in rubidium. Passive mechanical stability at this level is hardly realizable. Therefore active stabilization of the laser frequency has been designed with special emphasis on high gain in the acoustic frequency range. The lock bandwidth has been measured with a network analyzer (Fig. 2.14 a)). The unity gain point is at 250 kHz (Fig. 2.14 b)) with the phase margin (not shown on the graph) below 180 degrees. Below 250 kHz the amplitude of disturbances is suppressed by a factor increasing by 20 dB per decade.

Mini drop tower test

In order to test the sensitivity of the laser to vertical acceleration, a mini drop tower assembly with a drop altitude of approximately 1 m has been built in Berlin (Fig. 2.15 a)). Test objects are fastened to a platform that is identical to the standard ZARM drop capsule platform. In order to assure high repeatability of experimental conditions, the platform is falling down suspended with linear ball bearings to two high precision, stainless steel rods. Deceleration is done by a 30 cm thick foam sheet. The height and softness of the foam have been chosen such that the impact deceleration is comparable to that in the ZARM drop tower (Fig. 2.15 b)). As seen in figure 2.15 a), the master laser in the laboratory test stays locked after an impact with the vertical acceleration exceeding 45 g.

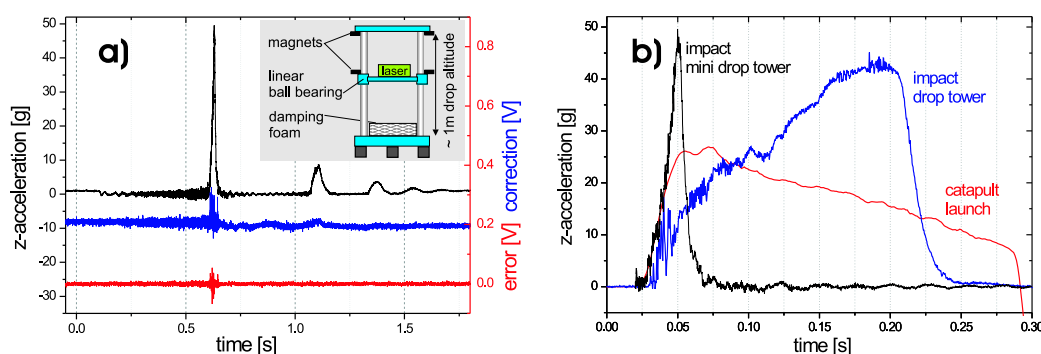


Figure 2.15: Laser lock test on the mini drop tower: a) z-acceleration (black), error signal (red), and feed back (correction) signal (blue) during a drop from 1 m height. The error signal does not change and the laser stays locked. b) comparison of the z-acceleration of the mini drop tower, ZARM drop tower impact, and that of the catapult launch.

Drop tower test at ZARM Bremen

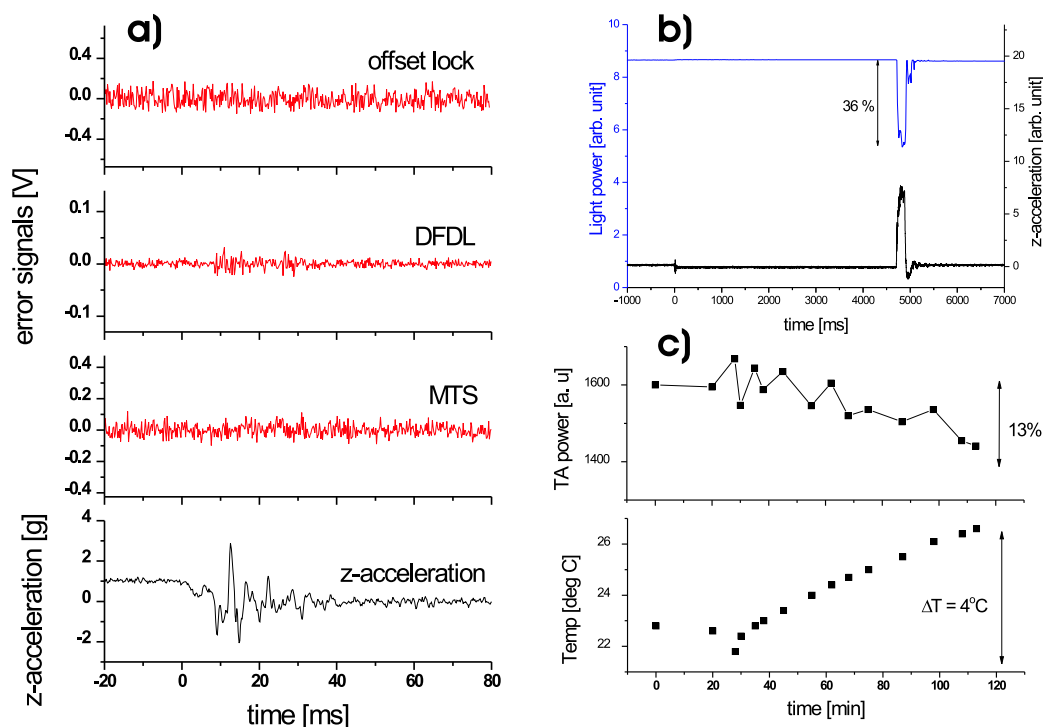


Figure 2.16: Drop tower test of the laser system: a) laser frequency during capsule release; b) fiber coupling stability during the flight; c) long run temperature stability of the TA power.

A dedicated test of the laser system stability has been carried out at ZARM in Bremen. Graph a) in figure 2.16 shows the error signals of both MTS and DFDL master lasers⁵ and of the offset lock during capsule release. All three lasers remain locked and their frequency is not sensitive to residual capsule vibrations. Figure 2.16 b) shows the stability of the fiber coupling during the flight. In the moment of capsule release the intensity remains stable, it drops by about 36% during recapture to finally reach its beginning value. The latter indicates no need to readjust the fiber coupling after each drop. The result of the long-run temperature sensitivity test of the TA output power is shown in figure 2.16 c). For a typical temperature change of 4 degrees in the drop capsule the output power of the TA drops by 13%. Both, coupling of the seeding laser to the TA and coupling of the TA in the

⁵At the time the laser system was tested in the drop tower we were using DFDL to lock the repumping laser. It has been later on replaced by the "trombone" offset lock, but the feedback electronic (lock-box) stayed unchanged.

fiber are sensitive to the temperature and thus contribute to a decrease in the output power. However, the test has been performed without connecting the capsule to the water cooling circuit, thus 13% is regarded as an upper limit of the slow power drift.

Catapult test

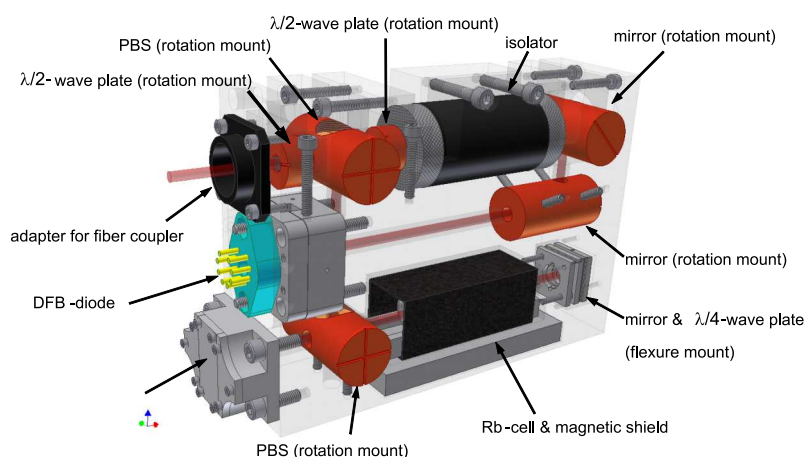


Figure 2.17: “Block laser”- catapult capable master laser concept.

The catapult facility at ZARM in Bremen can extend the microgravity time up to 9 s. However, the acceleration that occurs at the launch of the capsule is comparable to that at the impact (Fig. 2.18). This dramatically enhances the demands on shock-insensitivity of the laser. As a part of the preparation for the future catapult-launched cold atoms experiments, we have built an ultra-stable prototype of the master laser. It is based on FM spectroscopy with direct current modulation. In contrast to the present lasers, where all optics is mounted on a flat planar base, the new block-like construction (Fig. 2.17) has been optimized for maximum stiffness. Details of the mechanical design can be found in reference [Schiemangk, 2007]). By building this laser care has been taken to minimize any back reflections into the laser diode (including stray light). In particular, we identified the back reflection from the AR-coated window of the TO3 housing of the laser diode to be the main drawback of the setup. Therefore we operate the laser with diode-can open⁶. Moreover, the lock bandwidth has been increased to more than 300 kHz by improvements in both the lock electronics and the generation

⁶To avoid water condensation, the diode is run at a temperature higher than the room temperature.

of the error signal. The latter involves optimizing the relative intensities of the pump and probe beam in the Rb cell. On one hand, by low intensity the amplitude of the error signal decreases. Moreover, the atom's reaction to variations in the laser frequency is slowed down due to the lowered optical pumping rate. Higher intensity, on the other hand, leads to excessive power broadening of the spectrum. We accept the power broadening of a few Γ_{nat} in order to make the lock faster.

Due to some technical problems with the catapult facility, the block-laser has not been launched yet and the next laser-test campaign is planned for February 2009. However, the experiences gathered during the construction of the block-laser have been implemented in one of the lasers that are already in use in Bremen. This laser has been catapulted three times, once staying locked during launch and after impact (Fig. 2.18).

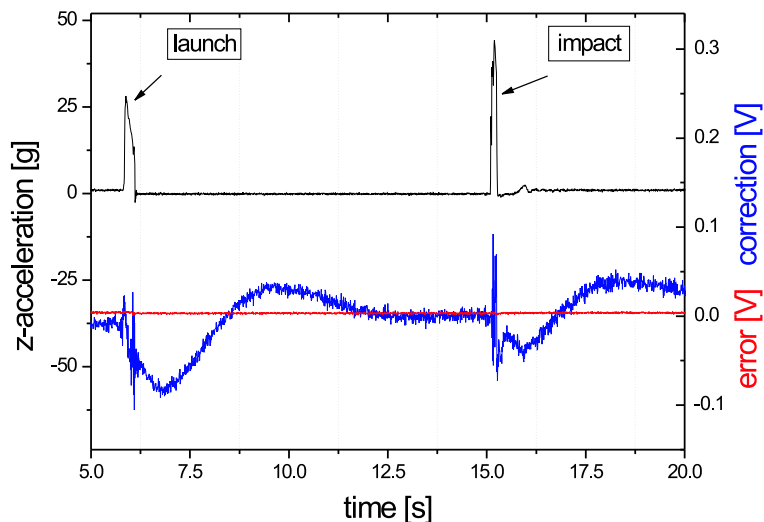


Figure 2.18: The z-acceleration by the catapult launch (black), error signal (red) and feed-back (correction) signal (blue). Constancy of the error signal indicates that the laser stayed locked during the flight and after impact.

Detection

All information relevant for data analysis like the number of trapped atoms or size and position of the cloud are extracted from the resonant absorption imaging [Lye et al., 2002]. The detection beam, similar as the 4 MOT beams, is provided to the vacuum chamber with a polarization maintaining optical fiber and expanded to a diameter of 20 mm with a telescope arrangement (for details of the telescope mount see [van Zoest, 2008]). Trapped or released

from the trap atoms are illuminated with the collimated detection beam with circular $\sigma+$ polarization resonant⁷ with the $|5^2S_{1/2}, F = 2, m_F = 2\rangle \longrightarrow |5^2P_{3/2}, F = 3, m_F = 3\rangle$ transition in ^{87}Rb . The intensity of the detecting beam is 0.3 mW/cm^2 , which is much less than the saturation intensity of rubidium. The atoms absorb a part of the resonant light, which is seen as a shadow by the 12 bit CCD-camera chip (Hamamatsu, C8484-15G) placed face to face with the detection beam. Despite the AR-coating of the imaging optics, interference patterns like Newton's rings, that significantly degrade the picture quality, are unavoidable. In order to get rid of them, the image of the atomic shadow is followed by a second one without atoms, but with roughly the same interference pattern of the laser beam. Subtraction of the two images cancels the laser intensity pattern. Denoting the intensity distribution of the two captured images by $A(x, z)$ and $B(x, z)$ respectively one gets:

$$\begin{aligned} A(x, z) &= I_0(x, z)e^{-O(x, z)} + \text{Noise} \\ B(x, z) &= I_0(x, z) + \text{Noise}, \end{aligned} \quad (2.1)$$

where the laser beam propagates along the y -axis with the intensity distribution $I_0(x, z)$. $O(x, z)$ is the optical density of the atomic sample and Noise the constant level of thermal noise of the camera. The latter is measured by simply taking a dark picture with all lasers off. From 2.1 one can determine the optical density:

$$O(x, z) = \ln \left(\frac{B(x, z) - \text{Noise}}{A(x, z) - \text{Noise}} \right). \quad (2.2)$$

The optical density is directly proportional to the atomic density $n(x, y, z)$ integrated along the y -direction:

$$O(x, z) = \sigma \int_{-\infty}^{+\infty} n(x, y, z) dy = \sigma D(x, z), \quad (2.3)$$

with a cross-section σ for atom-light interaction given by

$$\sigma = \frac{\sigma_0}{1 + 2\frac{I}{I_{sat}} + (2\frac{\delta}{\Gamma_{nat}})^2}. \quad (2.4)$$

The resonant cross-section is $\sigma_0 = 2.910^{-9} \text{ cm}^2$, the saturation intensity $I_{sat} = 1.67 \text{ mW/cm}^2$ [Steck, 2008], I is the detection laser intensity and δ

⁷Detection takes place in the presence of a magnetic field, thus the Zeeman level shift has to be taken into account for an estimate of the resonant frequency

the detuning from resonance. In order to calculate the number of atoms N one has to integrate $D(x, z)$ over the picture area A :

$$N = \int_A D(x, z) dx dz = \frac{1}{\sigma} \int_A O(x, z) dx dz. \quad (2.5)$$

The integral 2.5 can be done in two ways. Numerically one can sum the optical density O_i over all CCD pixels: $N = \sum_i \frac{O_i a}{\sigma}$, where a is the area of a single pixel. The second method is to make an explicit assumption about the spatial shape of $D(x, z)$ (a Gaussian distribution for thermal atoms and an inverted parabola for the BEC) and to fit the assumed function to the captured data. With the results of this fit one can easily calculate the integral. Both methods have been implemented by us.

2.3.5 Drop capsule board computer

The experiment is controlled by two commercially available computers (National Instruments) mounted in a compact PXI-chassis inside of the drop capsule. Both of them are operating with a Real Time (RT) operation system allowing for timing precision on a μs level. LabView routines (Virtual Instruments - VIs), that are communication interfaces between the user and the RT-hardware are loaded to the memory of the RT computer via WLAN when the capsule is hanging at the top of the drop tower. One of the computers belongs to the standard equipment of the drop capsule and is partially used to control and trigger the capsule release process as well as to measure and save some physical parameters before and during the drop (capsule pressure and temperature, acceleration) [Dro, 2007]. The second computer serves exclusively for controlling the Quantus experiment. In particular, three relevant VIs run on it: one to lock the lasers before the experiment starts, one to generate the actual experimental time sequence and the third to trigger the camera and to capture absorption images. These three routines as well as the data acquisition cards handled by them are described in detail in [van Zoest, 2008].

2.4 Time sequence

In this section the timing of the experiment is described. It takes less than 15 s to run the whole experimental sequence once. During this time atoms are captured from the thermal background and slowed down in successive cooling stages (Tab. 2.2) culminating with the achievement of quantum degeneracy. The way to produce the BEC in microgravity is the same as in

the laboratory on the earth. Differences appear only after emergence of the BEC and they concern the flatness of the final holding trap as well as the time of free evolution (TOF) after turning the trap off.

2.4.1 Doppler cooling in the magneto-optical trap

Macroscopic MOT

Since laser cooling is for the present experiment a tool rather than a subject of investigation, it will not be treated in detail here. A review of the theory, different techniques and applications of the laser cooling can be found in numerous textbooks, e.g. [Metcalf and van der Straten, 1999].

First, thermal background atoms are captured in the center of the mirror MOT. As a source for thermal atoms we use a rubidium dispenser (SAES Getters), that is operated at a current of 5.5 A. The trap consists of four circularly polarized laser beams (Fig. 2.7) detuned from the resonance by $\delta = 23$ MHz, with a light power of 15 mW each and 2 cm beam diameter. The beams intersect at the zero of the quadrupole magnetic field generated by a pair of macroscopic anti-Helmholtz coils (blue in Fig. 2.6). With a maximum current of 7 A, these coils can generate a magnetic field gradient of 12 G/cm at the trap center.

Approximately 10^8 ^{87}Rb atoms at a temperature of $220 \mu\text{K}$ are loaded to the MOT. Since the MOT loading time is approximately 10 s it takes place before dropping the capsule. At this time the timing sequence is suspended with the MOT loading still progressing. The further run of the sequence is triggered by the acceleration sensor at the moment of the capsule release. Subsequently the macroscopic MOT remains on in microgravity for one more second. The reason for this extension of the MOT phase is to let residual atomic oscillations subside after the capsule release⁸ (Fig. 2.3). Moreover, by varying this time slightly, we can precisely determine the height in the drop tower at which the phase transition to BEC takes place. This is important, because residual magnetic fields vary throughout the drop tower (Fig. 4.10). These fields affect the parameters for the evaporative cooling and we have to make sure that they are the same for each drop.

U-MOT

The next step is to transfer the atoms to the chip-MOT. Superimposing a homogeneous magnetic field with the quadrupole field shifts the position of the field minimum. By ramping the bias field in the y -direction from 0 to

⁸MOT is a nonconservative trap

Table 2.2: Cooling phases

	MOT loading	MOT	U-MOT	optical molasses	optical pumping	magnetic trap	compression	evaporation I	evaporation II	evaporation III	decompression	holding	free expansion
duration [ms]	10^4	$1.1 \cdot 10^3$	5	4	0.7	0	20	540	400	160	752	18	< 1000
atom number		10^8	$5 \cdot 10^7$	$1.3 \cdot 10^7$	10^7	$4 \cdot 10^6$		$8 \cdot 10^4$	$2.5 \cdot 10^3$	10^4	$8 \cdot 10^3$	$8 \cdot 10^3$	$8 \cdot 10^3$
temperature [μ K]		220	200	20-30			50			0.5		0.023	
phase-space density						$2 \cdot 10^{-7}$	$2 \cdot 10^{-7}$	$2 \cdot 10^{-2}$	> 1	> 2.6	> 2.6	> 2.6	
$\omega_x/2\pi$ [Hz]						25.6	20.7	13.7		18.5	4.46	4.46	0
$\omega_y/2\pi$ [Hz]						259	1338	7620		2245	13.4	13.4	0
$\omega_z/2\pi$ [Hz]						262	1344	7623		2249	21.7	21.7	0
f_{evapor} [MHz]							40	5	3.1	2.695	2.88		
z-acceleration	1 g	0	0	0	0	0	0	0	0	0	0	0	0

1.2 G within 20 ms (not shown in table 2.2) we move the cold atom cloud towards the chip surface to the position of minimum of the U-MOT magnetic field.

The U-MOT, or the chip-MOT is a magneto-optical trap for which the quadrupole magnetic field is obtained by superposition of a homogeneous field with a field of a microscopic U-shaped current conductor (the field of such wire configuration is discussed in section 3.2.1). Turning off the macroscopic MOT coils takes up to a few ms. During this time the magnetic field is undefined. Therefore, to avoid unwanted "kicks" we switch off the laser light for 4 ms (not shown in table 2.2). At the same time the chip U-current of 2 A is turned on and the bias field had already been turned on during shifting of the MOT.

Compared to the macroscopic coils, micro-fabricated wires on the chip can generate much higher field gradients with much smaller current. The position of the trap minimum is therefore better defined and can be controlled more precisely. This is advantageous for loading the magnetic trap. On the other hand, the capture volume of the chip trap is smaller so that it cannot be effectively loaded directly from the thermal background. Rather, loading with atoms precooled in a macroscopic MOT is required. The transfer efficiency is thereby about 50% which results in approximately 5×10^7 trapped atoms.

Finally, the U-MOT is shifted within 20 ms to the position of the minimum of magnetic trap (not shown in table 2.2).

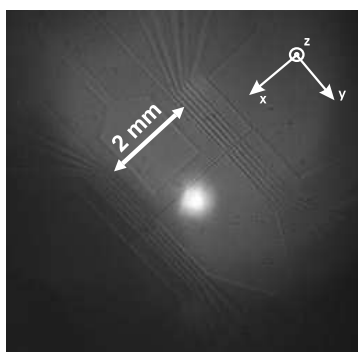


Figure 2.19: *Fluorescence picture of 5×10^6 atoms trapped in the U-MOT. The structure of the atom chip with the U-shaped wire can be seen in the background.*

2.4.2 Optical molasses

In the process of Doppler cooling the action of red detuned light on atoms creates a viscous environment with velocity-dependent friction force ("a fly in a honey jar"). Hence the process is also called optical molasses. A simple model of Doppler cooling concerns two-level atoms and predicts a minimal

achievable temperature of $T_D = \hbar\Gamma_{nat}/(2k_B)$ also called the Doppler limit⁹. Experimentally however one observes optical molasses with temperatures well below T_D [Lett et al., 1988]. The theoretical explanation of this phenomenon [Dalibard and Cohen-Tannoudji, 1989] takes into account the multilevel Zeeman structure of the atomic states involved in the cooling cycle and the spatial dependence of the light polarization resulting from the superposition of two counter-propagating laser beams. Thus cooling in an optical molasses is frequently called polarization gradient cooling. The additional cooling mechanism works at atomic velocities comparable to a few multiples of the recoil velocity $v_R = \hbar k/m$ (with the atomic mass m and the wave number of the laser radiation k). Thus it affects atoms that are much slower than the Doppler cooling capture range Γ_{nat}/k . For these atoms the dependence of the friction force on atomic velocity is steeper than in "normal" Doppler cooling.

In our molasses, the laser detuning is increased for 4 ms to $\delta = 29 \times \Gamma_{nat}$, the power of the trapping and repumping laser is reduced to 80% of their MOT-values, and the magnetic fields and chip current are turned off. It is important that no residual magnetic fields are present at the location of the atoms. Despite of the μ -metal screening of the vacuum chamber, a residual field of 0.1 G in the x -direction, 0.19 G in the y -direction, and 0.15 G in the z -direction remains and has to be compensated with external coils. With well optimized molasses we are able to capture 1.3×10^7 atoms at a temperature of 18.4 μ K. The corresponding phase-space density (ρ_{ps}) is 6×10^{-6} . For comparison, rubidium atoms from the thermal background in our vacuum chamber ($T = 300$ K, $p = 10^{-10}$ mbar) are characterized by a phase-space density of 3×10^{-21} . This illustrates what a powerful tool the laser cooling is. Though, due to the recoil associated with each photon absorption process, a further increase in ρ_{ps} is hardly possible with the use of dissipative light forces¹⁰.

2.4.3 Optical pumping

According to equation 3.2 the strength of the confining potential depends on the quantum magnetic number m_F . Therefore it is reasonable to trap the atoms in the Zeeman state with the highest possible magnetic moment. Within 700 μ s we optically pump the atoms to the $|F = 2, m_F = 2\rangle$ state. For optical pumping we use $\sigma+$ polarized light propagating in the y -direction (de-

⁹The Doppler limit for Rb is $T_D = 145 \mu$ K.

¹⁰Overcoming the recoil limit for laser cooling has been reported however at less than three dimensions [J.Reichel et al., 1995] or at relatively low atomic densities.

tection beam), resonant with the $|5^2S_{1/2}, F = 2\rangle \rightarrow |5^2P_{3/2}, F = 2\rangle$ transition. All other lasers are switched off at this time. To define the quantization axis for optical pumping we turn on the homogeneous magnetic field of 8 G in the y -direction which simultaneously serves as the bias field for the following Z-trap.

2.4.4 Magnetic Z-trap

Immediately after the optical pumping is finished, a current of 2 A in the Z-path of the chip is switched on. The Z-current together with the 8 G bias field mentioned above form an Ioffe-Pritchard magnetic potential elongated in the x -direction (Fig. 2.20 a)). The strong asymmetry of the potential in the z -direction is caused by the singularity on the chip surface at $z = 0$ (see chapter 3 for details of the chip geometry). However at the trap bottom the potential is nearly cylindrically symmetric and in the harmonic approximation is characterized by the trapping frequencies: $\omega_{x,y,z} = 2\pi \times (25.6, 259, 262)$ Hz. The trap center is at the position $z_0 = 446 \mu\text{m}$ under the chip surface.

The transfer efficiency is limited by the trap volume to about 35% so that we are able to confine 4×10^6 atoms in the magnetic trap. Atoms are slightly heated during loading of the magnetic trap and the resulting temperature is $50 \mu\text{K}$.

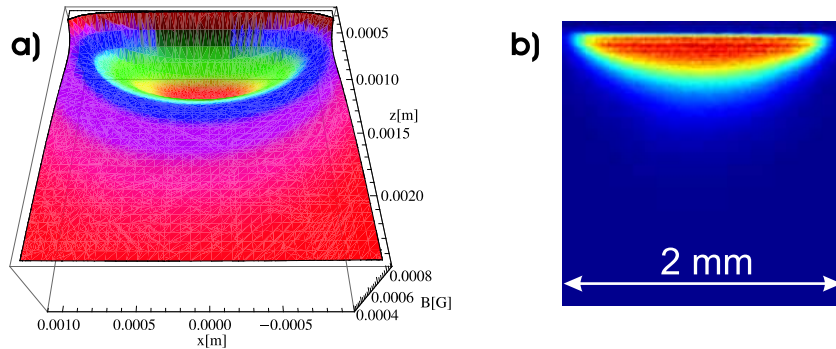


Figure 2.20: *Initial magnetic trap. a) Simulation of the magnetic potential at $y = 0$ for a chip current $I = 2$ A and a bias field $B_0 = 8$ G. The initial trap depth is 6.74 G, which corresponds to $453 \mu\text{K}$ in temperature units. b) Absorption image of the 4×10^6 atoms in the initial trap.*

Trap compression

Compression of the trap does not change the phase-space density: an increase in atomic density is associated with an increase in the temperature so that phase-space density remains constant. However, at higher densities the elastic collision rate and therefore the speed of the evaporative cooling grows (see also Sec. 3.2). The initial trap is compressed by raising the bias field to 27 G within 20 ms. At the same time the amplitude of an additional homogeneous field in the x -direction is increased from 0 to 3 G. This field defines the value of the magnetic field at the trap minimum and thus the Larmor precession frequency (Eq. 3.3). Increasing the Larmor frequency is necessary to avoid trap losses caused by Majorana-Spin-Flips (see also Sec. 3.1.1). The compressed trap has the harmonic frequencies: $\omega_{x,y,z} = 2\pi \times (20.7, 1338, 1344)$ Hz at the minimum at $z_0 = 146 \mu\text{m}$ away from the chip.

2.4.5 Evaporative cooling

Evaporative cooling [Davis et al., 1995b,c; Ketterle and van Druten, 1996] has been a key technique in all experiments aiming to achieve Bose-Einstein condensation so far. It allows to increase phase-space density by more than 6 orders of magnitude while the number of atoms decreases only by a factor of 100. The idea behind evaporative cooling is a successive removal of the hottest particles from the sample and subsequent rethermalization via elastic collisions resulting in a decreased average energy per particle. For this purpose we utilize the so called RF-knife. This technique uses radio frequency (RF) radiation to induce transitions between Zeeman sublevels separated by the magnetic field. The frequency of the radiation matches the Zeeman splitting of the most energetic atoms. These atoms are transferred to the states with lower quantum number m_F until they end up in a high field seeking state and are repelled from the trap (Fig. 2.21 a)). The evaporation frequency is chirped as the temperature of the sample decreases.

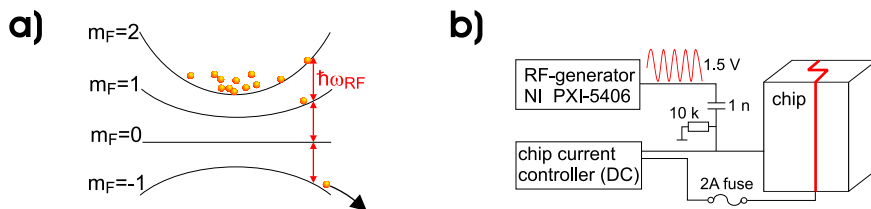


Figure 2.21: *Evaporative cooling in the magnetic trap with the RF-knife method. a) Zeeman states are split in the magnetic field of the harmonic trap; b) Coupling of the RF-frequency directly to the chip.*

A common way to irradiate the atoms with RF is to use a macroscopic antenna which can be a single coil with a few cm diameter. However, for effective evaporation a few Watt of RF-power is required. Instead, we AC-couple the RF-power directly to the chip Z-wires (Fig. 2.21 b)). Our "on-chip" antenna is located less than 1 mm away from the atom cloud, thus only a few mW of RF-power are required. Radio frequency is generated by a 16-bit frequency synthesizer (NI PXI-5406) which is a part of the data acquisition equipment of our board computer. No additional amplifier is required.

The evaporation process takes 1.1 s. This is a typical duration for a chip-based experiment and is one order of magnitude shorter than in macroscopic magnetic traps or in optical dipole traps. The evaporation is split into 3 phases (Tab. 2.2). The RF-knife is turned on at the end of the trap compression with the beginning frequency of 40 MHz. Subsequently the frequency is ramped linearly within 540, 400 and 160 ms to 5 MHz, 3.1 MHz and 2.695 MHz respectively, culminating with the transition to a BEC.

Whereas the chip current of 2 A is kept constant during evaporation, the bias field is varied. In the first phase it increases to 65 G in order to compress the trap further. The maximum trapping frequencies are $\omega_{x,y,z} = 2\pi \times (13.7, 7620, 7623)$ Hz. A high atom density is advantageous for fast evaporation, however the rate of inelastic 3-body collisions (3-body recombination), which are the main loss channel from the trap, raises dramatically as n^2 . Thus, it is necessary to decompress the trap as the evaporation proceeds. The bias field is reduced to 55 G at the end of the first phase, 53 G in the second phase and 35 G at the end of evaporation. The final trap in which the BEC emerges has the frequencies: $\omega_{x,y,z} = 2\pi \times (18.5, 2245, 2249)$ Hz.

Figure 2.22 illustrates the enhancement in the phase-space density and the loss in the number of atoms during the three phases of evaporation cooling.

2.4.6 Phase transition to BEC

The formation of a BEC occurs at the beginning of the last evaporation phase at the critical temperature $T_c \approx 560$ nK (Eq. 1.2 with $N = 20000$ atoms and $\bar{\omega} = 2\pi \times 454$ Hz). With proceeding evaporation the last thermal atoms are removed from the trap or condense. Finally we produce pure BECs with approximately 10000 atoms (more than 90% in the condensed phase).

2.4.7 Decompression

The steep trap holding the BEC has to be adiabatically decompressed for two reasons. First, three-body inelastic collisions at the density of the condensate of $5 \times 10^{14} \text{ cm}^{-3}$ would limit its lifetime to a few tens of ms. Second, a

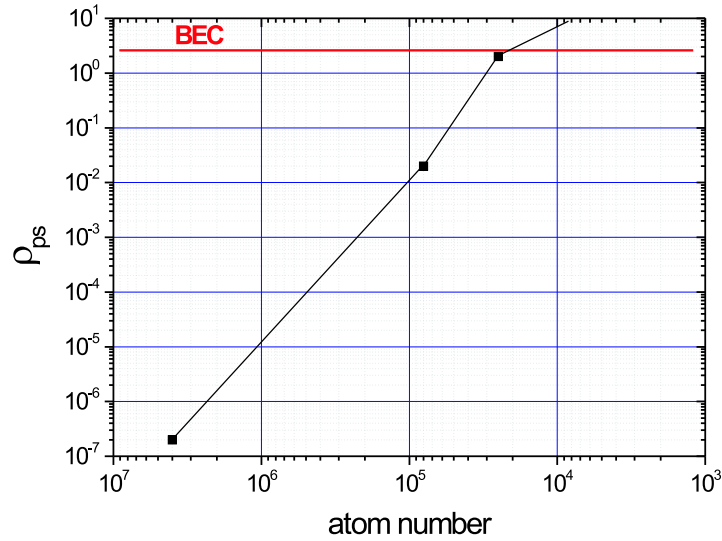


Figure 2.22: *Enhancement in phase-space density during the three phases of evaporative cooling*

reduction of the trapping frequencies is necessary in order to slow down the free expansion after switching off the trap. Adiabatic decompression of the trap is discussed in section 4.2.

In order to get rid of the remaining thermal atoms, the RF-frequency is kept on for another 350 ms and is ramped up to 2.88 MHz.

The variation of any parameter (e.g. an analog voltage) from one phase of the experiment to another can be chosen to be done in three alternative ways: stepwise, linearly or by smooth ramping. Most of the time the two first methods are used. However, during decompression the position of the minimum of the magnetic potential varies, which can lead to unwanted momentum transfer to the condensate and collective oscillation of its center-of-mass (Sec. 4.2.3). Therefore it is required, that decompression is performed in smoothest possible way to minimize the acceleration of the trap center. This is realized by Gauss-like ramping of the parameter value:

$$P(t) = (P_{start} - P_{stop})e^{-\left(\frac{t}{AT}\right)^a} + P_{stop}, \quad (2.6)$$

where $P_{start/stop}$ is the beginning and the final value of a parameter P , T is the duration of the ramp, A and $a \approx 1.7$ are free parameters, whose values are tuned empirically.

2.4.8 Holding trap and free expansion

After decompression atoms are held for 18 ms in the final shallow trap whose calculated trap frequencies are $\omega_{x,y,z} = 2\pi \times (4.46, 13.4, 21.7)$ Hz. Varying the holding time can be useful for a measurement of the oscillation or the lifetime in the trap (Sec. 4.2.3).

At the end of the holding trap the magnetic fields and the chip current are turned off. We leave only a weak homogeneous field of 0.8 G in the y -direction to fix the quantization axis. The condensate expands freely for the time of up to 1 s. The results are presented in section 4.3.3.

Free expansion is followed by a destructive absorption image (Sec. 2.3.4).

Chapter 3

Atom chip

A proper explanation of the results presented in the next chapter requires a knowledge of the magnetic field generated by the chip-trap with a μG precision. Since the simulation of this field was an essential part of this work, it is worth to study the principle of operation of a magnetic micro-trap in detail and to characterize the magnetic potential generated by the Quantus chip.

3.1 Magnetic trapping of neutral atoms

The idea to use magnetic fields to control the motion of particles emerged from molecular beam physics, mass spectrometry and particle accelerator physics. Planar multipole fields were primarily used for focusing and guiding neutral particles having permanent magnetic dipole moment [Friedburg and Paul, 1951]. A straightforward way to realize a closed storage volume - a trap - is to properly bend the two-dimensional field. An example is a magnetic storage ring in which a sextupole field is bent to a torus. The magnetic storage ring was used in the late seventies to confine cold neutrons for several minutes - the time substantially exceeding their natural decay time [Kügler et al., 1978]. It is remarkable, that it were neutrons which were trapped magnetically first, despite the fact that their magnetic moment is a thousand times smaller than that of some neutral atoms (e.g. alkalis). Though, three-dimensional DC magnetic traps play nowadays a crucial role in production of atomic BECs. It is worth to underline the fact, that, with the exception of the optical dipole traps [Cennini et al., 2003], so far there is no way to achieve Bose-Einstein condensation in dilute gases other than magnetic trapping and successive forced evaporative cooling.

3.1.1 Magnetic potential

For a particle with a permanent magnetic dipole moment $\vec{\mu}$ placed in a magnetic field \vec{B} the interaction energy is given by:

$$U = -\vec{\mu} \cdot \vec{B} = -\mu B \cos \vartheta, \quad (3.1)$$

where ϑ is the angle between $\vec{\mu}$ and \vec{B} . A classical object like a bar magnet or a compass needle, simply aligns its magnetic moment parallel to the field in order to reduce its energy. However, the magnetic moment of single atoms or molecules arises from the angular motion (and/or spin) of their elementary components. Thus, the behavior in a magnetic field is similar to that of a spinning top in gravity. The exerted torque $\vec{\tau} = \vec{\mu} \times \vec{B}$ produces a change in angular momentum perpendicular to that angular momentum. This drives the magnetic moment to precess around the direction of the magnetic field keeping the angle ϑ constant (the so called Larmor precession - see Fig. 3.1).

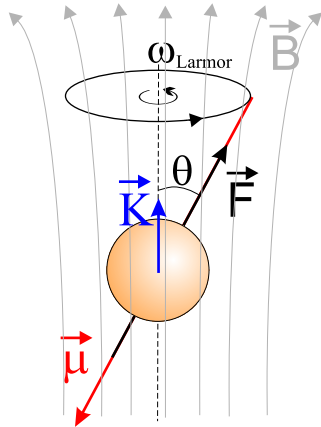


Figure 3.1: A weak field seeking atom with a total angular momentum \vec{F} and magnetic dipole moment $\vec{\mu}$ placed in an inhomogeneous magnetic field \vec{B} . $\vec{\mu}$ precesses with the Larmor frequency ω_{Larmor} around the local direction of the magnetic field. The force (here denoted as \vec{K} to avoid confusion with the angular momentum \vec{F}) points in the direction of the weak field.

Quantum mechanics allows only for discrete energy values depending on the quantum number m_F of the projection of the total angular momentum \vec{F} on \vec{B} :

$$U(m_F, B) = \mu_B g_F m_F B, \quad (3.2)$$

where μ_B is the Bohr magneton and g_F the g-factor. The angular frequency ω associated with the energy splitting $U = \hbar\omega$ can be interpreted classically as the Larmor precession frequency. From 3.2 one gets:

$$\omega_{Larmor} = \frac{\mu_B g_F m_F}{\hbar} B. \quad (3.3)$$

For ^{87}Rb in its ground state $5^2S_{1/2}$, $F = 2$ and $m_F = 2$: $\omega_{Larmor} \approx 9 \text{ MHz/G}$.¹

¹valid only for magnetic fields, for which the interaction energy is small compared to the hyperfine splitting

3.1.2 Harmonic approximation

An important remark about equation 3.2 is that the potential energy depends on the magnitude, not on the sign of the magnetic field: $U \propto |\vec{B}| = B$. The curvature of the potential and thus its attractive or repulsive character depends on the sign of the product $g_F m_F$. Maxwell's equations do not allow for existence of a local magnetic field maximum in free space (Wing's theorem [Wing, 1984]). Thus, only particles with $g_F m_F > 0$ (weak field seeking states) can be confined in a local minimum of the (static) magnetic field.

Around the minimum, the trapping potential can be approximated by a harmonic one with the characteristic oscillation frequency along the i th eigenaxis of the potential:

$$\omega_{trap}^i = \sqrt{\frac{\mu_B g_F m_F}{m} \frac{\partial^2 B}{\partial x_i^2}}. \quad (3.4)$$

See Appendix A for details of calculating trapping frequencies in 3D.

3.1.3 Majorana losses

The above considerations are only valid as long the spin orientation relative to the magnetic field is conserved - classically one would say: as long ϑ stays constant. However, the field direction in a three-dimensional trap varies in space. To fulfill the condition of constant ϑ the atom must move slowly enough such that its magnetic moment adiabatically follows the direction of the field. This is the case when the rate of change of ϑ is much less than the precession frequency ω_{Larmor} . The upper limit for $\frac{d\vartheta}{dt}$ is the harmonic trap frequency ω_{trap} . Consequently, a stable trap requires:

$$\omega_{Larmor} \gg \omega_{trap}. \quad (3.5)$$

The adiabaticity condition 3.5 can be violated in regions of weak magnetic field for instance in the trap center, where ω_{Larmor} is correspondingly small. In such regions spin flips called ‘‘Majorana flops’’ [Majorana, 1932] take place leading to losses from the trap. This is a problem for traps that use quadrupole fields generated by a pair of anti-Helmholtz coils (MOT coils) which have a zero crossing of the field. To avoid the Majorana losses another type of magnetic trap with non zero magnetic field minimum can be used. The most common such configuration is that of the Ioffe-Pritchard trap [Pritchard, 1983]. For review and detailed analysis of the magnetostatic traps see reference T.Bergeman et al. [1987].

Typical harmonic frequency of a steep trap for rubidium is of the order of a few kHz. With a 1 G magnetic field in the minimum the Larmor precession

frequency for an atom with $m_F = 2$ is roughly 9 MHz, which is fairly enough to satisfy the condition 3.5.

3.2 Microchip traps

Evaporative cooling, the final cooling stage on the way to BEC, can increase phase-space density of an atomic ensemble by many orders of magnitude. The key role in an effective evaporation plays a high elastic collision rate γ :

$$\gamma = n\sigma\bar{v}, \quad (3.6)$$

where n is the density, σ the elastic scattering cross section, and \bar{v} the mean atomic velocity. Adiabatic compression of the trap increases both n and \bar{v} . A typical three-dimensional harmonic trap is composed of a set of macroscopic coils and bars with spatial extent ranging from a few cm up to 1 m. In order to compress the trap, and to reach the desired steepness, high currents of up to a few hundred A are required. Thereby several kW of Joule heat is dissipated which can cause a variation of the trapping potential due to thermal expansion of the coils. This puts challenging technical demands on cooling the apparatus.

The idea to use micro-fabricated conducting planar structures to generate three-dimensional magnetic confinement has been suggested by Weinstein and Libbrecht [Weinstein and Libbrecht, 1995] in 1995. It is based on the fact, that the magnetic field around a thin wire carrying the current I scales with the distance r as I/r . The corresponding gradient and curvature of the field scale as I/r^2 and I/r^3 respectively. Still, sub-mm wires with a cross-section of several μm^2 can carry a few A of current. Thus, reduction of the characteristic size of the trap (i.e. the distance from the conductors to the trap minimum) promises an enormous improvement in the trap steepness and at the same time significantly reduces power consumption. Table 3.1 compares some properties of a tightly confining Ioffe-Pritchard (IP) trap, built of a set of macroscopic coils by a group in Amsterdam, and described in [Dieckmann, 2001], with the chip trap used for the Quantus experiment. Despite over 50 times smaller current, the microtrap allows for tighter confinement resulting in ten times faster evaporation time. Unfortunately, miniaturization affects the number of condensed atoms. 10^4 atoms in a BEC is a typical value for chip traps. However, some setups optimized for higher trap depth and volume achieve 10 times larger condensates [Ott et al., 2001; Schwindt, 1997].

Nowadays a multitude of different chip-trap configurations have been designed and used worldwide. For a detailed review and application of mi-

Table 3.1: *IP coil trap from Amsterdam vs. Quantus chip*

	IP coil trap	Quantus chip
current [A]	400	2 chip + 5.3 bias coil
power dissipation [kW]	5.4	< 0.01
switch-off time [μ s]	60	< 1
radial gradient [G/cm]	353	6300
radial frequency [Hz]	$2\pi \cdot 477.4$	$2\pi \cdot 7620$
axial frequency [Hz]	$2\pi \cdot 20.6$	$2\pi \cdot 25.6$
evaporation time [s]	10.6	1.1
atom number in BEC	$3.8 \cdot 10^6$	9500

crotraps see references Reichel et al. [2001]; Folman et al. [2002]). Rapid development in the field has culminated in 2001 with the realization of an on-chip Bose-Einstein condensate by groups in Tübingen and Munich [Ott et al., 2001; Hänsel et al., 2001].

3.2.1 Principle of operation

Two-dimensional confinement

Consider an infinitely thin wire carrying a current I along the positive x direction (Fig. 3.2 a). The magnetic field is concentric and has an amplitude that decays with the distance r from the wire axis:

$$B_{wire}(r) = \frac{\mu_0 I}{2\pi r}, \quad (3.7)$$

where μ_0 is the permeability of vacuum. If a uniform external field \vec{B}_0 is added perpendicular to the wire axis, it cancels the tangential component of B_{wire} at the height:

$$z_0 = \frac{\mu_0 I}{2\pi B_0}, \quad (3.8)$$

forming a line of zero field along the wire at $\vec{r} = [x, 0, z_0]$ (Fig. 3.2 b). It has been shown, that atoms can be guided in such a two-dimensional trap [Denschlag et al., 1999]. This particularly simple field configuration is a starting point for three-dimensional confinement, therefore it is instructive to point out some of its properties. First, the field is of a quadrupole type: its amplitude vanishes at the minimum and rises linearly and radially symmetric in the vicinity of this minimum (see the density plot of the field amplitude in Fig. 3.2 c) and cross sections of it along z and y in Fig. 3.2 d). For $y = 0$

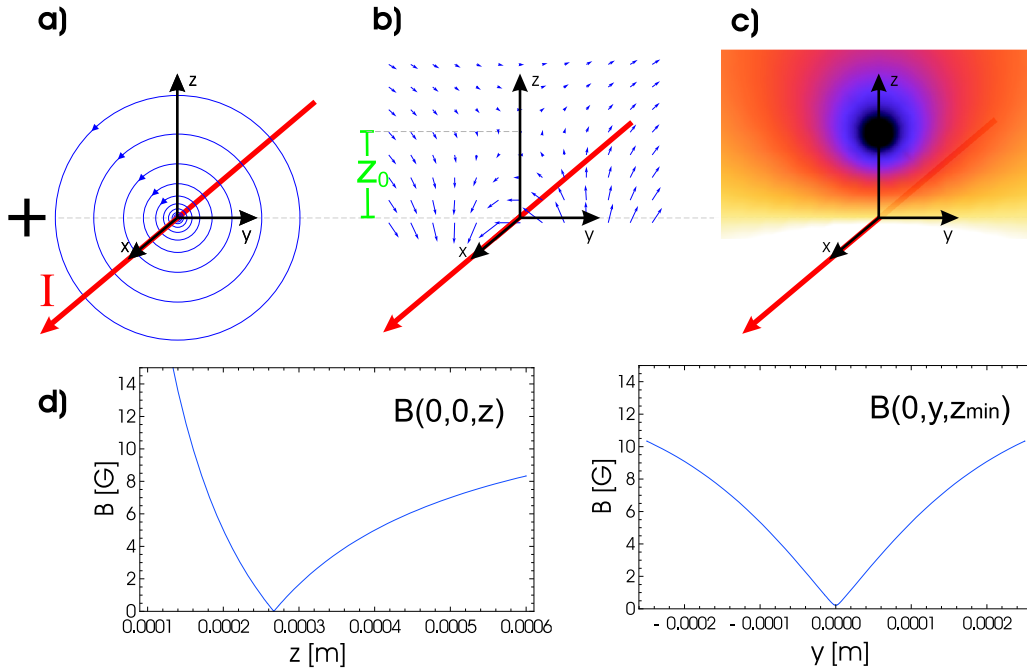


Figure 3.2: a) Two dimensional quadrupole confinement along a current carrying wire is formed by the addition of a homogeneous field B_0 perpendicular to the wire axis. b) The resulting vector field has a zero-crossing line at the distance z_0 from the wire axis. c) shows the density plot of the total magnetic field amplitude B (dark colors mean small field) and d) the cross-sections taken at the minimum. The plots were calculated for $I = 2$ A and $B_0 = 15$ G.

the gradient of the field amplitude has only a vertical component, which can be calculated by differentiating 3.7:

$$|B'(r)|_{y=0} = \frac{\mu_0 I}{2\pi r^2}. \quad (3.9)$$

In order to estimate the magnitude of the field gradient on the transverse axis passing through the minimum, consider figure 3.3. It shows the magnetic field at the distance r from a current carrying infinitely thin wire laying along the x -axis. As in figure 3.2, an external homogeneous field \vec{B}_0 in the y -direction is superimposed on that of the wire. At the minimum \vec{B}_{wire} has the same direction as \vec{B}_0 and the resulting field is zero. At a distance δr from the minimum the amplitude of the field B_{wire} is (almost) the same as at the minimum, but has a slightly different direction. The resulting field

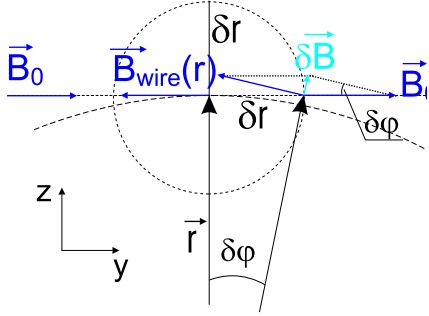


Figure 3.3: Towards estimation of the field amplitude gradient along the transverse axis passing through the minimum of the quadrupole field generated by a current carrying wire and a homogeneous bias field.

(light blue) can be approximated by:

$$\delta B = B_{wire}(r)\delta\varphi. \quad (3.10)$$

Substituting $B_{wire}(r) = \mu_0 I / (2\pi r)$ and $\delta\varphi = \delta r / r$ one gets for the transverse field gradient:

$$\frac{\delta B}{\delta r} = \frac{\frac{\mu_0 I}{2\pi r} \frac{\delta r}{r}}{\delta r} = \frac{\mu_0 I}{2\pi r^2}. \quad (3.11)$$

Thus, in the vicinity of the minimum, the gradient on the transverse axis is the same as on the vertical axis and the trap has a radial symmetry.

Second differentiation of equation 3.7 and substituting $r = z_0$ from equation 3.8, yields the field curvature at the minimum²:

$$B''(z_0) = \frac{(2\pi)^2 B_0^3}{\mu_0^2 I^2}. \quad (3.12)$$

Equations 3.8, 3.9, and 3.12 show, that the full control over the trap parameters depends on two physical variables I and B_0 .

Three-dimensional confinement

Three dimensional confinement requires a field with non-zero magnetic field components in x direction in addition to the field configuration described above. This can be generated by bending the wire. Depending on how the wire is bent, one distinguishes between two basic trap types: U- and Z-trap (Fig. 3.4). In both cases the field generated by the central part of the wire (along the x -axis), combined with the external field, produces a two-dimensional quadrupole trap as before. The x -components from the bent

²Due to the zero crossing, the first derivative of the modulus of the field is not continuous at z_0 and thus the second derivative does not exist. However, for three-dimensional traps with a non-zero minimum, this discontinuity is abrogated and equation 3.12 gives a good approximation for the field curvature and consequently for the radial trap frequency ω_{rad}

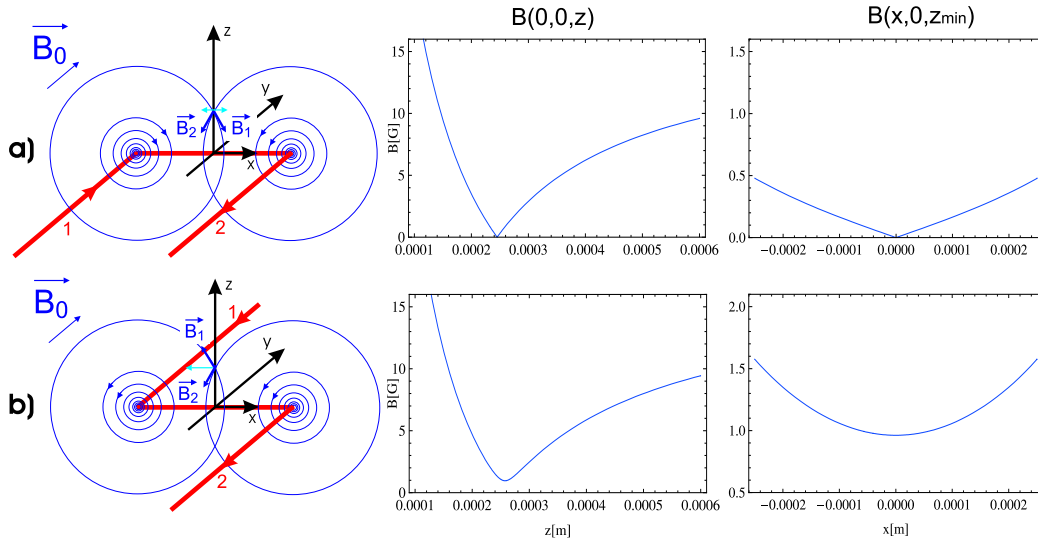


Figure 3.4: Three-dimensional confinement by U- and Z-trap. a) The U-trap is of the quadrupole type: the field is zero at the minimum and rises linearly in the vicinity of it. b) The Z-trap is of the Ioffe-Pritchard type: the field has a finite x -component at the minimum (light blue arrow). Note a slight shift of the minimum in the z -direction compared to the field from Fig. 3.2. This shift is caused by the non-vanishing z -components of the field generated by the bent part of the wire (marked as 1 and 2) which are superimposed on the quadrupole field of the central part of the wire. The plots were calculated for $I = 2$ A and $B_0 = 15$ G, and a distance of 2 mm between wires 1 and 2.

part of the wire close the trap along the x axis, whereas z -components shift the position z_0 of the quadrupole minimum. Axial confinement is usually much weaker than radial. Note, that the vertical scale of the very right graphs in figure 3.4 is ten times smaller than that of the left graphs.

In the case of the U-trap, the x -components of the field from the bent part of the wire cancel at the center of the trap. The resulting field is zero, therefore quadrupole-like (in all three spatial directions). Hence, the U-trap is used as a microscopic equivalent of quadrupole coils in the magneto-optical trap (see section 2.4.1).

The Z-trap, in contrast, is of the Ioffe-Pritchard type. It has a non-vanishing x -component at the minimum. This field component is perpendicular to the field of the central wire. All components are added quadratically, so that the discontinuity of the first derivative of the field amplitude is abrogated.

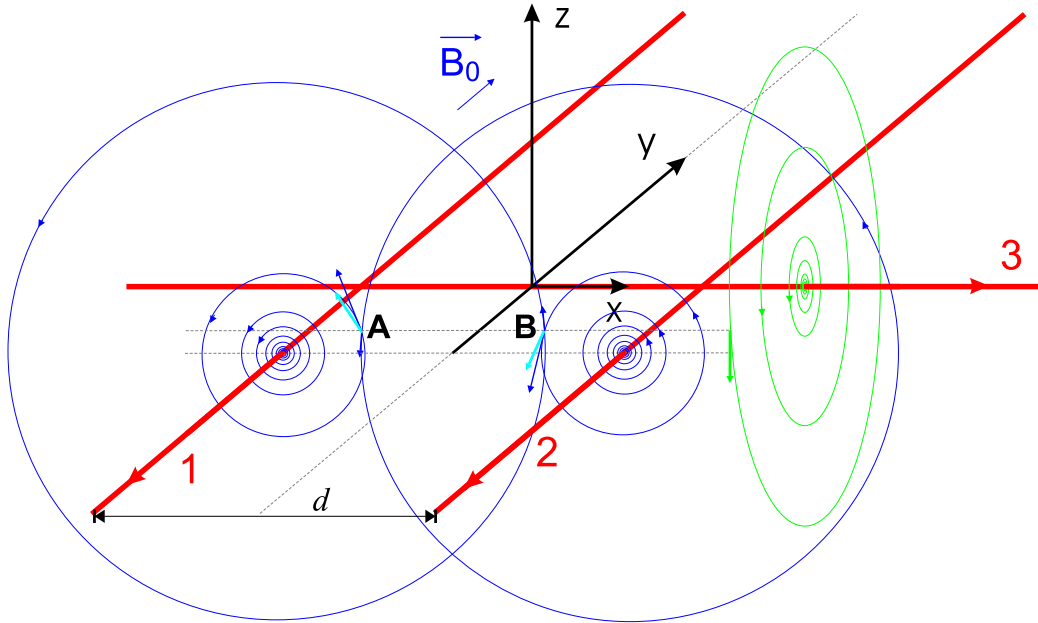


Figure 3.5: Wire configuration for an H-type trap. Despite the symmetry of the currents, the amplitude of the magnetic field at points **A** and **B** differs leading to a tilt of the potential with respect to the x -axis (details in text).

3.2.2 Ideal H-trap

The major advantage of a Z-type trap is that it can easily be realized with a single wire and an external bias field. However, this simplicity limits the diversity of possible field configurations. Alternatively to bending the wire, a three-dimensional confinement can be achieved with additional wires perpendicular to the central one. Consider two such parallel wires at a distance d , forming an H-type trap (Fig. 3.5). Although this requires separate current drivers for each wire, it provides more flexibility. In particular, varying the current in one of the parallel wires shifts the position of the trap minimum along the axial direction. Moreover, inverting the current direction in one of the wires changes the quadrupole trap into an Ioffe-Pritchard one. Last, but not least, the possibility to change the current in the central wire separately, provides independent control of axial and radial confinement.

An ideal H-trap as the one shown in figure 3.5 is assumed to be composed of infinitely long and infinitely thin wires. This assumption greatly simplifies the calculation of the field distribution and its analysis. Still, most of the properties of such an ideal trap are valid also for real traps (both: H- and Z-type) as long the wires are longer than their separation d .

The ansatz for the calculation is a simple analytic formula for the mag-

netic field around an infinite wire. For the wires of the Ioffe Pritchard trap in figure 3.5 this yields:

$$\begin{aligned}\vec{B}_{1,2}(x, y, z) &= C \begin{bmatrix} -z \\ 0 \\ x \pm \frac{d}{2} \end{bmatrix} \frac{1}{(x \pm \frac{d}{2})^2 + z^2} \\ \vec{B}_3(x, y, z) &= C \begin{bmatrix} 0 \\ -z \\ y \end{bmatrix} \frac{1}{y^2 + z^2} + \begin{bmatrix} 0 \\ B_0 \\ 0 \end{bmatrix},\end{aligned}\quad (3.13)$$

with $C = \frac{\mu_0 I}{2\pi}$. For simplicity the current is assumed to be equal in each arm. The amplitude of the resulting magnetic field is:

$$B = \sqrt{\vec{B} \cdot \vec{B}}, \quad (3.14)$$

with $\vec{B} = \vec{B}_1 + \vec{B}_2 + \vec{B}_3$.

Shape of the potential

Figure 3.6 shows surfaces of constant field amplitude B for the H-type trap. As already seen from figure 3.4, the axial confinement is usually much weaker than the radial one. This statement is valid only if the trap minimum is located close to the wire plane: $z_0 \ll d/2$. If this is the case, the potential is cigar-shaped with the main axis along x . A parameter that characterizes elongation of the trap is the ratio of axial to radial trapping frequency:

$$\epsilon = \frac{\omega_{ax}}{\omega_{rad}}. \quad (3.15)$$

Obviously $\epsilon \ll 1$ for a cigar-shaped trap. For the highly compressed Z-trap used in the Quantus experiment, $\epsilon \approx 1/320$.

Further away from the minimum the potential apparently differs from its harmonic approximation (right column in figure 3.6) and looks rather submarine- than cigar-like. This flattening of the equipotential surfaces for $z < z_0$ is caused by a rapid growth of the field amplitude close to the chip surface.

Asymmetry

Due to the symmetry of the wire configuration, the potential of the H-trap might be expected to have a perfect radial symmetry around the x -axis. In fact, only the position of the minimum: $\vec{r}_0 = [0, 0, z_0]$ remains "symmetric". The symmetry axis of the trap is tilted in the xy -plane (Fig. 3.7). This tilt

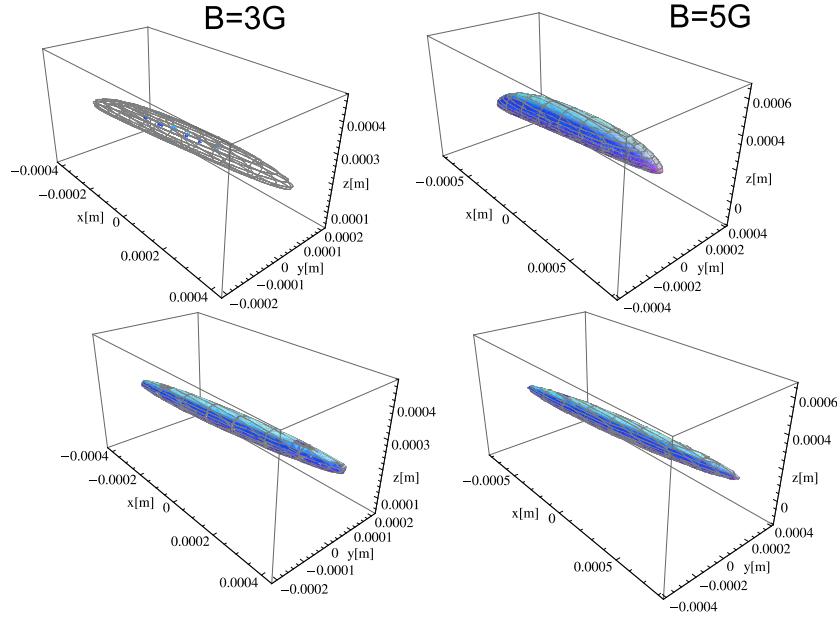


Figure 3.6: Surfaces of constant field amplitude of 3 G and 5 G (upper row) for the H-trap (Fig. 3.5) and harmonic approximation of the potential (lower row). The graphs were made with $I = 2$ A, $B_0 = 15$ G, and $d = 2$ mm. The value of the field amplitude at the minimum is $B_{min} = 2$ G, and the harmonic frequencies are: $\omega_{x,y,z} = 2\pi \times (39, 521, 535)$ Hz.

originates from the vector addition of the field components which can easily be understood from figure 3.5. Consider the magnetic field at points **A** and **B** located above the chip surface, symmetrically with respect to the yz -plane. The magnetic field vectors at these points (light blue arrows) generated by the currents in the wires 1 and 2 have equal amplitude, but opposite sign of the z -component. Adding the field of wire 3 (green arrow), which for $y \neq 0$ has a non-zero z -component, results in a total field amplitude that is slightly higher at point **B**. Thus, the equipotential lines in the vicinity of the minimum tend to tilt towards point **A**.

Maximum displacement of the minimum

According to equations 3.8 and 3.12 one could expect, that, by reducing the bias field B_0 , arbitrary shallow traps at any distance z_0 can be achieved. These equations, however, are valid only for the simple two-dimensional case of figure 3.2. In 3D they are a good approximation for steep potentials with a minimum close to the chip surface.

Figure 3.8 shows what happens to the vertical confinement of an H-trap

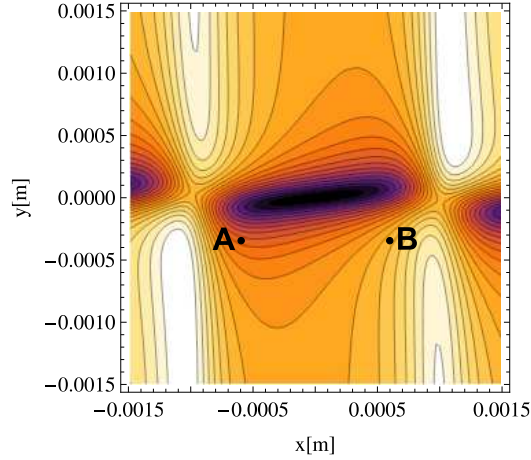


Figure 3.7: Density plot of the amplitude of the magnetic field generated by the H-trap at $z = z_0$. Dark colors correspond to decreasing field; the white "hills" are caused by the wires lying underneath (Fig. 3.5). The symmetry axis of the potential is tilted in the xy -plane. .

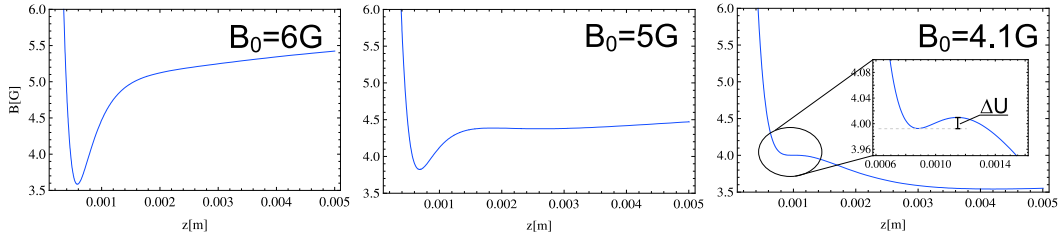


Figure 3.8: Amplitude of the magnetic field for the H-trap ($I = 2$ A and $d = 2$ mm) at $x = y = 0$ for decreasing value of the bias field B_0 .

if one reduces B_0 . The trap opens and the vertical position of the minimum shifts towards its maximal value z_0^{max} , for which the minimum disappears. If the bias field is reduced such that the minimum position is close to z_0^{max} the field amplitude for $z > z_0^{max}$ is lower than that at the minimum, which can lead to tunneling of atoms through the potential barrier ΔU . For $z \rightarrow \infty$ the chip field vanishes and the potential increases: $B(z) \rightarrow B_0$ (not shown in figure 3.8). One should however not be confused by the presence of a second minimum for $z > z_0^{max}$ - it is just a minimum in one direction and the overall gradient at this point does not vanish.

Such behavior of the potential is caused by the presence of x -components of the magnetic field (generated by the wires 1 and 2) which are vectorially added to the quadrupole field of the central wire. Quantitatively one can characterize the "opening" of an H-trap with the wire separation d with the

following statements:

- The maximal vertical position of the minimum is:

$$z_0^{max} = \frac{d}{2}.$$

- If a minimum exists, the field amplitude at the minimum (trap bottom) is lower than the bias field:

$$B(z_0) < B_0.$$

In the limiting case $B(z_0^{max}) = B_0$.

- For a given current I , z_0^{max} is reached for the bias field:

$$B_0^{min} = \frac{2C}{d},$$

with $C = \frac{\mu_0 I}{2\pi}$. For $I = 2$ A and $d = 2$ mm, $B_0^{min} = 4$ G.

- Second mixed derivatives $\frac{\partial^2 B}{\partial x \partial z}$ and $\frac{\partial^2 B}{\partial y \partial z}$ vanish at the minimum, therefore one of the eigenvectors of the Hessian matrix (Appendix A) equals $[0, 0, 1]$. Consequently, the vertical axis of the trap is parallel to the z -axis.
- By asymptotically approaching z_0^{max} , the vertical trapping frequency ω_z can take an arbitrary small value.
- The other two frequencies are equal at z_0^{max} and reach there a finite saturation value:

$$\omega_{x,y} = \sqrt{\frac{\mu_B g_F m_F}{m} \frac{8C}{d^3}}.$$

For $I = 2$ A and $d = 2$ mm, $\omega_{x,y} = 2\pi \times 25.5$ Hz.

- The tilt angle discussed in the previous section increases with increasing z_0 and asymptotically reaches its maximum value for $z_0 \rightarrow z_0^{(max)}$. At $z_0^{(max)}$ this angle is undefined due to the equality of the two horizontal trapping frequencies.

From the four last statements it can be seen, that the trapping potential, initially cigar-shaped along the x -axis, evolves during decompression to become cigar-shaped along the z -axis (Fig. 3.9 left).

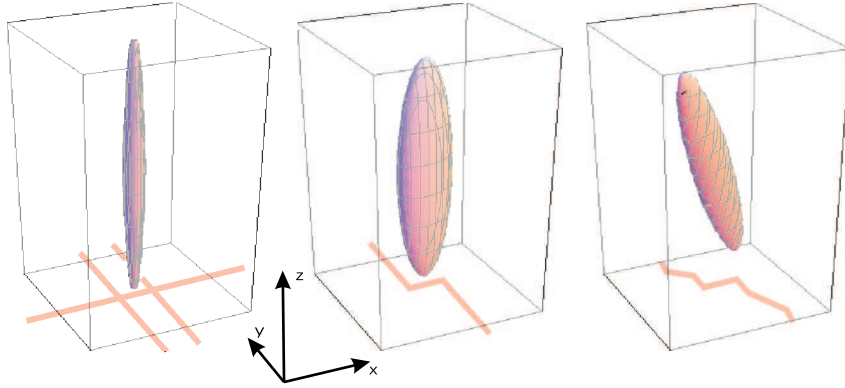


Figure 3.9: Equipotential surfaces of extremely decompressed traps ($z_0 \rightarrow z_0^{(max)}$) for the H trap, Z trap and more realistic Z trap with diagonal wires.

3.2.3 Z-trap

The properties of an ideal Z-trap (with infinite wire 1 and 2) are qualitatively very similar to those of an H-trap. However, the missing halves of the wires 1 and 2 as well as the short central wire (of length d), lead to some quantitative differences. First, x -components of the field at the trap center are lower than for an H-trap. Consequently, the trap is deeper and the maximum vertical position of the minimum $z_0^{(max)}$ can exceed $d/2$. Second, the trapping potential still has one of its principal axes along z , for which the corresponding trapping frequency ω_z is arbitrarily small for $z_0 \rightarrow z_0^{(max)}$. However, there is no cylindrical symmetry as in the case of an H-trap and the potential resembles a pumpkin seed (Fig. 3.9 center). The reason for this is, that in the horizontal plane there is a strong confinement from wire 1 and 2 along the diagonal axis connecting those wires. In comparison to an H-trap, a Z-trap with $d = 2$ mm and $I = 2$ A reaches $z_0^{(max)} = 2.3$ mm with $B_0 = 1.84$ G and has horizontal frequencies $\omega_{1,2} = 2\pi \times (8.5, 4.3)$ Hz with a tilt angle of approximately 30° . To achieve lower frequencies, one has to put a magnetic field in the x -direction opposite to the field generated by the Z-wires. This way the trap bottom is lowered further. Thereby attention should be paid not to violate inequality 3.5 which could lead to Majorana losses in the trap.

3.2.4 Quantus chip

Real chips are usually composed of finite pieces of wires, some of which are directed diagonally. In addition, some wires must provide current to the chip, and they are most commonly perpendicular to the chip plane. As a

consequence of the presence of this additional wires the vertical principal axis of the potential is in general additionally tilted (Fig. 3.9 right).

Chip architecture

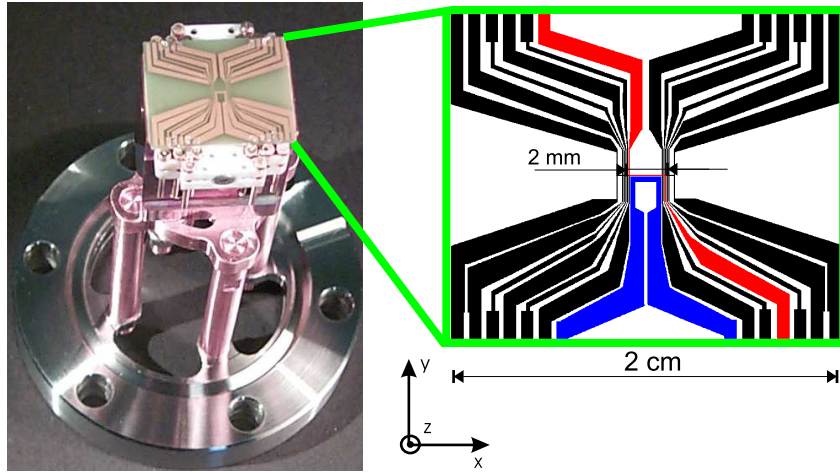
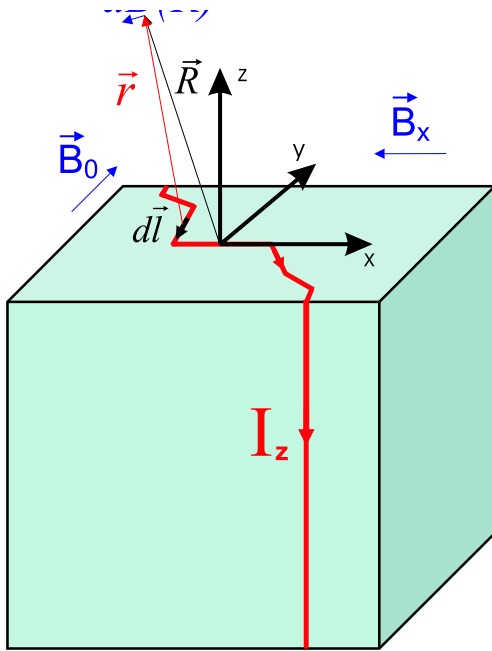


Figure 3.10: Atom chip used in the Quantus experiment mounted on a CF-40 vacuum flange (left). Chip surface with U- (blue) and Z-wires (red) for generation of quadrupole and Ioffe-Pritchard potentials respectively.

The chip used in the Quantus experiment is shown in figure 3.10. It can generate both: quadrupole and Ioffe-Pritchard magnetic potentials. Note, that only the central part of the chip with a spacial extension of roughly 2 mm contains the bent wires that form the U and the Z shape. All other diagonal wires, that provide current to the central part, are negligible with respect to the tightly confining potentials with a minimum close to the chip surface. However, they can drastically change the properties of an ultra-shallow trap, whose minimum is located at a distance $z_0 \approx 1$ mm. In particular, they lead to a tilt of the trapping potential with respect to the z -axis in addition to the tilt in the horizontal plane discussed in the previous section. Moreover, in order to model the potential of the final shallow trap (the holding trap) described in section 2.4, one has to take into account even the current-supplying wires which are perpendicular to the chip surface (Fig. 3.11).

The magnetic field generated by the chip has been calculated by integrating the Biot-Savart formula along current carrying wires and by adding external homogeneous fields:

$$\vec{B}(\vec{R}) = \frac{\mu_0 I_z}{4\pi} \int_l \frac{d\vec{l} \times \vec{r}}{r^3} + \vec{B}_0 + \vec{B}_x + \vec{B}_{ext}. \quad (3.16)$$



$$d\vec{B}(\vec{R}) = \frac{\mu_0 I_z}{4\pi} \frac{d\vec{l} \times \vec{r}}{r^3}$$

Figure 3.11: Biot-Savart law for calculation of the magnetic field generated by the chip wires.

\vec{B}_x is an additional homogeneous field used to increase the value of the Ioffe-Pritchard field at the minimum, in order to increase the Larmor precession frequency (Eq. 3.3). \vec{B}_{ext} represents all kinds of remaining magnetic fields, in particular the residual field inside the drop tower (Fig. 4.10). To calculate the integral in equation 3.16 the strip lines on the chip are modeled by a chain of straight and infinitely thin wires, for which an analytic solution to 3.16 exists. Parametrization of a straight thin wire is described in Appendix B.

Limits of the chip trap

It has been mentioned in the previous section, that trapping potentials with arbitrarily small harmonic frequency in z -direction can be generated with microtraps. However, the existence of the potential barrier ΔU (Fig. 3.8) and the decreasing potential beyond, limit the usefulness of extremely decompressed traps. At a certain minimum trap frequency, the mean atomic energy equals ΔU and atoms can leave the trap. In the Thomas-Fermi approximation (Sec. 4.1) the wave function of the trapped condensate vanishes for the trap energies greater than the chemical potential μ . Thus, the ratio $\Delta U/\mu$ serves as a measure of the trap depth. In figure 3.12 the trap depth $\Delta U/\mu$ is depicted as a function of the harmonic trap frequency in the direction of the

weakest confinement³. The minimum absolute depth at which the trap still holds the atoms is 1 (red straight line). However, due to anharmonicity of the potential further away from the minimum and due to the tunnel effect, one should assume $\Delta U/\mu > 1$ as a realistic limit for an efficient trap. As already mentioned, the existence of a potential barrier is correlated to the field amplitude in the x -direction. In our experiment, in order to minimize Majorana losses in the steep trap, we keep a field of 3 G in x -direction. This limits the minimum trap frequency to roughly $2\pi \times 3$ Hz. Figure 3.12 shows, that reducing this trap bottom field shifts the minimum trap frequency into the 1 Hz domain.

Note that in the presence of gravity the weakest potential curvature is almost one order of magnitude larger than in microgravity.

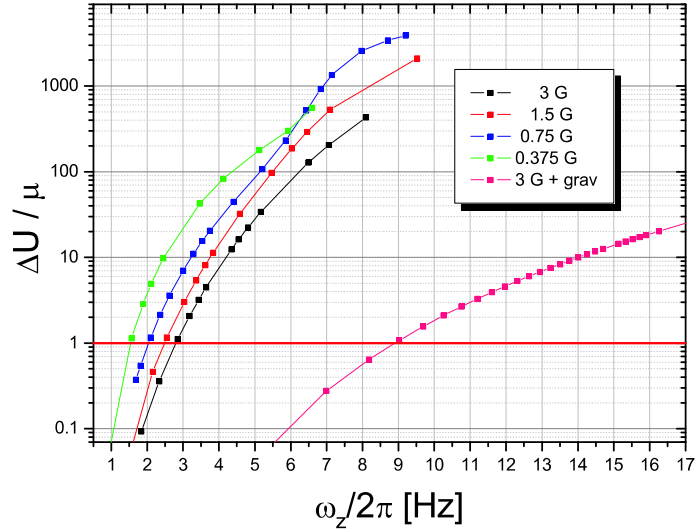


Figure 3.12: Ratio of the potential barrier ΔU to the chemical potential μ (trap depth) as a function of the trap frequency corresponding to the weakest axis of the harmonic potential for different values of external homogeneous magnetic field in the x -direction (trap bottom field). This simulation was done for $I = 2$ A and $N = 10000$ atoms.

³For the ideal H- or Z-trap this is the z -direction. For the real Quantus chip the weak vertical axis is tilted.

Chapter 4

First observation of the Bose-Einstein condensate in microgravity

4.1 Evolution of the BEC in a time dependent trap

The QUANTUS collaboration aims at observation of matter waves freely evolving for times unprecedented in any earthbound BEC experiment. In order to slow down the free expansion of the condensate, a reduction of the trap curvature (decompression) is required. A theoretical description of the experiment should therefore include the evolution of a Bose-condensed gas under variations of the confining potential. The formalism should also be valid in the limiting case of turning the potential completely off. Kagan *et al.* [Kagan et al., 1996] introduced a scaling approach which allows for an efficient description of the macroscopic wave function of a BEC in a time dependent isotropic harmonic potential. In the seminal paper by Castin and Dum [Castin and Dum, 1996] this theory was extended to 3D anisotropic harmonic potentials characterized by three trapping frequencies ω_i . However, the principal axes of the anisotropic trap were assumed to be time independent and parallel to the axes of the frame. Moreover, the position of the potential minimum was assumed to be fixed at the origin. None of these assumptions is directly applicable in our experiment. A natural generalization of the scaling approach that includes also arbitrary shifts and rotations of time dependent harmonic traps has been developed by the Quantus theory team from the University of Ulm and is described in detail in [Eckart, 2008]. The following section presents a brief overview of the basic ideas of

this approach.

4.1.1 Thomas-Fermi approximation

Following the notation of [Castin and Dum, 1996] the single particle wave function $|\Phi\rangle$ of the Bose-Einstein condensate in a static trap is described by the time independent Gross-Pitaevskii (GP) equation:

$$\mu\Phi(\vec{r}) = \left[-\frac{\hbar^2}{2m}\Delta + U(\vec{r}) + Ng|\Phi(\vec{r})|^2 \right] \Phi(\vec{r}). \quad (4.1)$$

$U(\vec{r})$ is the trapping potential, which, in the vicinity of the minimum, can be approximated by a harmonic one:

$$U(\vec{r}) = \frac{1}{2}m \sum_{j=1,2,3} \omega_j^2 r_j^2 \quad (4.2)$$

with harmonic frequencies ω_j and atom mass m . The last term of the Hamiltonian in equation 4.1 describes the atomic interactions in the mean-field approach. Each atom exerts an averaged force from all other atoms, therefore the mean-field energy is proportional to the atomic density $N|\Phi(\vec{r})|^2$, where N is the number of atoms. The interaction strength is characterized by a constant $g = 4\pi\hbar^2 a/m$, where a is the s-wave scattering length. For $g > 0$ the mean-field potential is repulsive. Finally μ is the chemical potential determined by the normalization of $|\Phi\rangle$:

$$\mu = \frac{1}{2}\hbar\bar{\omega} \left(15Na\sqrt{\frac{m\bar{\omega}}{\hbar}} \right)^{2/5}, \quad (4.3)$$

where $\bar{\omega} = (\omega_1\omega_2\omega_3)^{1/3}$ is the geometrical mean of the trap frequencies.

Equation 4.1 has a particularly simple solution in the regime where the atomic interactions are much larger than the level spacing of the trapping potential: $Ng|\Phi(\vec{r})|^2 \gg \hbar\omega_j$. In that case, one can use the Thomas-Fermi approximation to solve 4.1, that is, one can neglect the kinetic energy term. The resulting wave function is:

$$\Phi_{TF}(\vec{r}) = \sqrt{\frac{\mu - U(\vec{r})}{Ng}} \quad (4.4)$$

for $\mu \geq U(\vec{r})$ and 0 otherwise. If $U(\vec{r})$ is harmonic then a 1D cut through the condensate density $N|\Phi(\vec{r})|^2$ is an inverted parabola whereas a 3D ellipsoidal surface of constant energy $U(\vec{r}) = \mu$ determines the edge of the spatial extension of the condensate.

It is worth to investigate the limit of the validity of the Thomas-Fermi approximation. By neglecting the kinetic energy in 4.1 the total energy in the center of the trap is the mean-field energy and equals μ . Thus, in the Thomas-Fermi regime $\mu \gg \hbar\omega_j$ is required. The ratio $\eta = \mu(\bar{\omega})/(\hbar\bar{\omega})$ for a spherical symmetric trap ($\bar{\omega} = \omega_j \equiv \omega$) is plotted in figure 4.1. For $N = 10000$ atoms $\eta = 3$ for $\omega = 10$ Hz. The final decompressed trap (holding trap) in our experiment has the (geometric) mean frequency $\bar{\omega} = 2\pi \times 10.9$ Hz, and the frequency of the weakest confinement is $\omega_3 = 2\pi \cdot 4.46$ Hz, both satisfying $\eta \gg 1$.

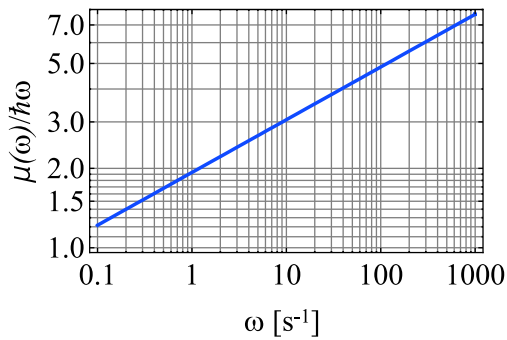


Figure 4.1: Validity of the Thomas-Fermi approximation. Ratio of the chemical potential to the trap level spacing as a function of average trap frequency for $N = 10000$ atoms.

4.1.2 Time dependent potential

Generalization of 4.1 to the time dependent case in which both U and Φ are functions of t leads to an explicitly time dependent GP equation for which the Thomas-Fermi approximation is not applicable. This equation can be solved numerically [Ruprecht et al., 1995] or, as derived in [Castin and Dum, 1996], by introducing a coordinate transformation: $r_j(t) = \lambda_j(t)r_j(0)$, ($j = 1, 2, 3$). The dynamic of the macroscopic wave function is then contained in the evolution of three scaling parameters λ_j , which obey the set of differential equations:

$$\ddot{\lambda}_j = \frac{\omega_j^2(0)}{\lambda_j \lambda_1 \lambda_2 \lambda_3} - \omega_j^2(t) \lambda_j \quad (4.5)$$

with the initial conditions $\lambda_j(0) = 1$ and $\dot{\lambda}_j(0) = 0$. The condensate density becomes a time dependent inverted paraboloid:

$$N |\Phi(\vec{r}, t)|^2 = \frac{1}{g \lambda_1(t) \lambda_2(t) \lambda_3(t)} \left[\mu - \frac{1}{2} m \sum_{j=1,2,3} \omega_j^2(0) \left(\frac{r_j}{\lambda_j(t)} \right)^2 \right] \quad (4.6)$$

if the right hand side is positive and zero otherwise.

4.1.3 Generalization to a rotating trap

The above approach describes the evolution of the macroscopic wave function of the condensate in a frame whose axes are collinear with the principal axes of the trapping potential. Moreover, the latter are assumed to be time independent. A natural generalization of the equations 4.5 and 4.6 can be introduced for the case of a rotating trap. A harmonic trap, whose principal axes are oriented arbitrarily in space is described by the Hessian matrix $\Omega(t)$ (Eq. A.1). Also the scaling parameters λ_j in this general case are represented by a matrix $\Lambda(t)$, which has to satisfy a nonlinear matrix differential equation [Eckart, 2008]:

$$\Lambda^T(t) \left(\frac{d^2\Lambda}{dt^2} + \Omega^2(t)\Lambda(t) \right) = \frac{\Omega^2(0)}{\det\Lambda(t)} \quad (4.7)$$

with the initial conditions $\Lambda(0) = \mathbb{1}$ and $\dot{\lambda}_j(0) = 0$. Obviously, in the case of a freely expanding condensate released from the trap at $t = t_0$, $\Omega(t) \equiv 0$ for $t > t_0$ is required. It is also straightforward to implement nonzero elements of the Hessian, that for $t > t_0$ describe residual fields and thus can influence the free expansion.

Evolution of the condensate density now becomes:

$$N |\Phi(\vec{r}, t)|^2 = \frac{1}{g \cdot \det\Lambda(t)} \left[\mu - \frac{1}{2} m (\vec{r} - \vec{r}_0(t))^T \mathbf{M}(t) (\vec{r} - \vec{r}_0(t)) \right] \quad (4.8)$$

for the right hand side positive and zero otherwise, with $\mathbf{M}(t) = (\Lambda^{-1}(t))^T \Omega^2(0) \Lambda^{-1}(t)$ and $\vec{r}_0(t)$ the time dependent position of the minimum of the potential. Thus, everything required to determine the dynamics of the condensate in a time dependent trap is the Hessian matrix of the potential $\Omega(t)$ and the position of the trap center $\vec{r}_0(t)$. Both were estimated by numerical calculation of the trapping potential $U(\vec{r}, t) \propto |\vec{B}(\vec{r}, t)|$ as described in section 3.2.4 and appendix A. The next section quantitatively summarizes the time evolution of the trapping potential during the trap decompression phase.

4.2 Evolution of the trapping potential

4.2.1 Adiabatic decompression of the trap

As shown in the last section, the trapping frequencies (or generally the Hessian matrix $\Omega(t)$) are crucial parameters that determine the free evolution of the condensate after switching-off the trap. In order to slow down the free expansion one has to adiabatically reduce the trapping frequencies (Fig.

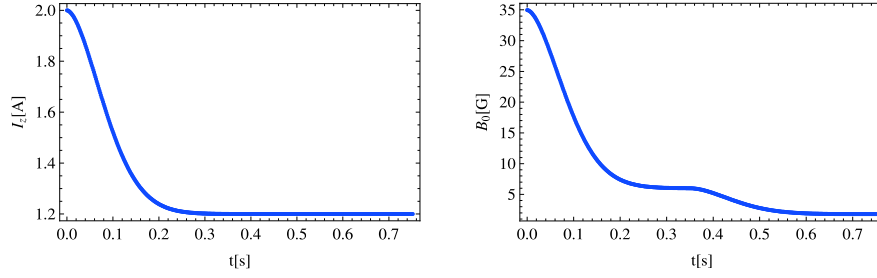


Figure 4.2: Lowering of the chip current I_z (left) and the bias field B_0 (right) by the decompression of the trapping potential.

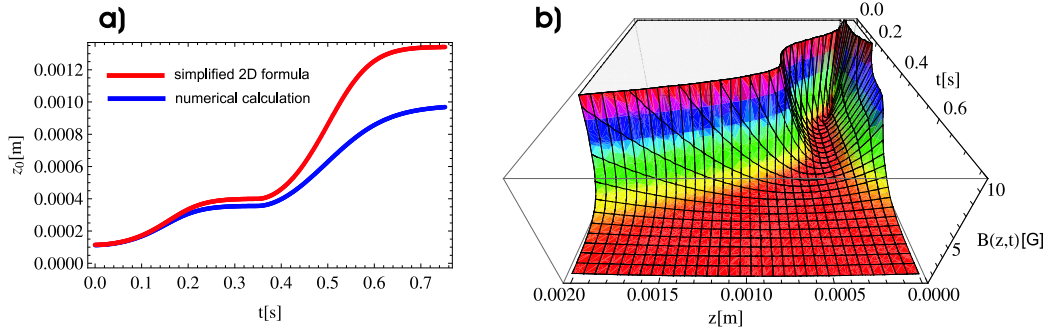


Figure 4.3: a) Position of the potential minimum z_0 during decompression of the trap: numerical calculation for the real trap (blue) and z_0 given by the 2D formula 3.8 (red). b) Time evolution of the confinement in the z -direction (in the harmonic approximation).

1.3). Adiabatically means slowly enough, so that the condensate can follow changes of the potential. This occurs when the time scale δt , on which the trapping frequency ω changes by $\delta\omega$, is of the order of the oscillation period in the trap: $\delta t \approx 1/\omega$. Moreover, one requires small frequency steps: $\delta\omega \ll \omega$. These two constraints combined lead to the adiabaticity condition:

$$\left| \frac{d\omega(t)}{dt} \right| \ll \omega^2(t). \quad (4.9)$$

As discussed in section 2.4, the Bose-Einstein condensate arises in a steep elongated trap with the radial and axial trapping frequencies $\omega_{rad} = 2\pi \times 2250$ Hz and $\omega_{ax} = 2\pi \times 18.5$ Hz. Subsequently the trap is decompressed within 752 ms. During that time both the chip current I_z and the bias field B_0 are decreased according to equation 2.6 (Fig. 4.2). Figure 4.4 presents details of the decompression process. Calculated trapping frequencies $f = \omega/(2\pi)$ are shown in figure 4.4 a). Their final values in the holding trap are: $f_x = 4.46$

Hz, $f_y = 13.42$ Hz, and $f_z = 21.75$ Hz. The radial frequencies f_y and f_z are almost equal during most of the decompression time. In the holding trap they differ by a factor of two leading to a pumpkin seed shape of the potential (Fig. 4.4 b)) Note that, due to rotation of the trap axes, the indices x, y, z do no longer have their initial meaning. In particular, the axes of the radial confinement are rotated by 90° and interchanged. Rather, in figure 4.4 b) colors are used to classify the principal axes of the potential and the associated frequencies: red for the strongest confinement, blue for the medium and green for the weakest.

Figure 4.4 b) shows the surfaces of constant energy equal to the chemical potential μ (plots are made for $N = 10000$ atoms). In the Thomas-Fermi approximation they give a quite reliable impression of how the confined condensate looks like. One can see that the trap, initially elongated in the x -direction (left graph), is tilted both in the horizontal plane and in the z -direction (right graph). The angles θ and φ that characterize the tilt of the weak axis are plotted as a function of time in figure 4.4 c).

Finally, figure 4.4 d) is a graphical check of the adiabaticity condition 4.9. The black curves are the squares of the trapping frequencies, and the red and green ones are the negatives of the time derivatives of f_y and f_x respectively. Clearly, condition 4.9 is fulfilled for the majority of the decompression time. Only at the end phase of the decompression the weak confinement seem to decrease too fast. However, the numerical solution of the time dependent GP equation [Eckart, 2008] did not show any unwanted dynamics of the condensate in the holding trap.

4.2.2 Shift of the trap center by decompressing

In the second phase of decompression (from 350 ms on), the value of the chip current I_z is kept constant at 1.2 A and the bias field B_0 is further reduced (Fig. 4.2). In doing so, the position z_0 of the minimum increases (Eq. 3.8). It has already been pointed out, that equation 3.8 is just an approximation valid in the two-dimensional case or for tightly confining traps close to the chip surface. Evolution of z_0 given by equation 3.8 for time dependent I_z and B_0 is shown in figure 4.3 a) (red). The blue curve is the actual position of the potential minimum, found numerically. Obviously, the two curves diverge for higher z_0 and equation 3.8 is does not hold in this regime. Figure 4.3 b) shows the time evolution of the confinement (in the harmonic approximation) in the z -direction.

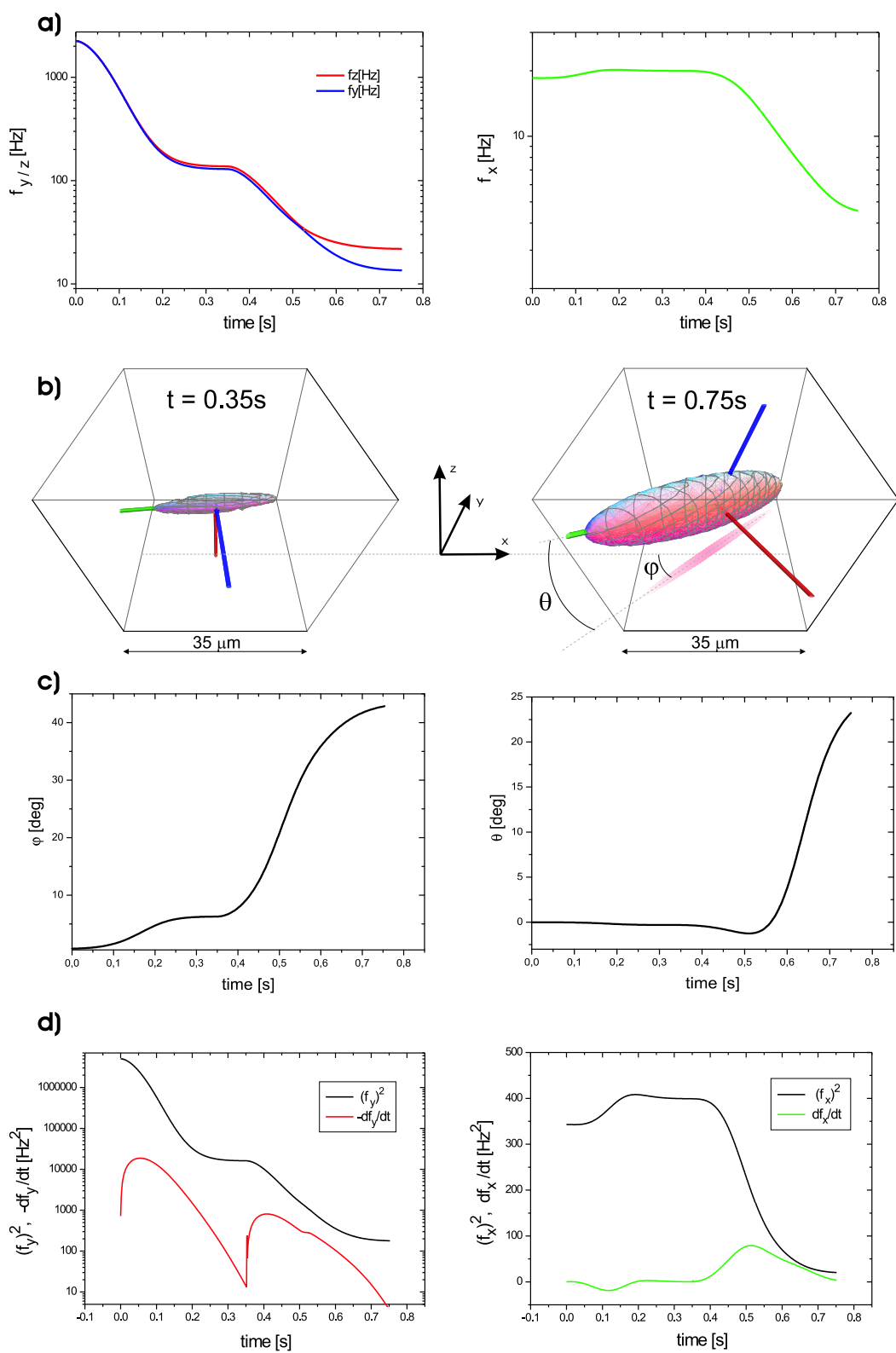


Figure 4.4: Adiabatic decompression of the trapping potential.

4.2.3 Collective oscillation of the BEC in the decompressed trap

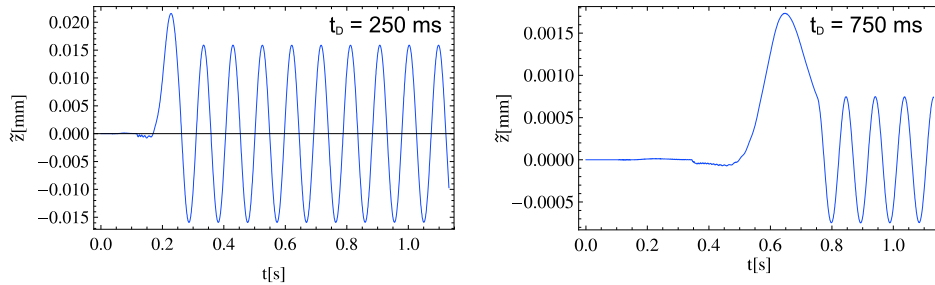


Figure 4.5: Calculated oscillations in the trap for a duration of the decompression of $t_D = 250$ ms (left) and $t_D = 750$ ms (right).

Before the trap is switched off, the potential minimum is intentionally shifted away in order to avoid a collision of the freely expanding condensate with the chip surface. On the other hand, moving the trap center can lead to some unwanted effects. Just imagine a barman who, while serving a beer, is sliding a glass on the table board. If you stop the glass all of sudden, you will lose half of your beer! In practice one cannot move an object from one place to another without accelerating it. In the rest frame of the trap center an inertial force acts on the atoms, which displaces them from the equilibrium position. Center-of-mass of the atomic cloud begins to oscillate around the momentary potential minimum (dipole oscillation). If the cloud is thermal, interatomic collisions will damp the oscillation. However, for a quantum degenerated gas, the conservative magnetic potential is an almost completely friction-free environment in which a collective oscillation can last for a time easily exceeding the vacuum limited lifetime of the BEC.

For an atom with mass m confined in a time dependent harmonic potential, the classical equation of motion in the z -direction¹ is:

$$m\ddot{z} = -k(t)(z - z_0(t)), \quad (4.10)$$

with the spring constant $k(t) = m\omega_z^2(t)$. In the rest frame of the trap center given by $\tilde{z}(t) = z - z_0(t)$, equation 4.10 can be rewritten as:

$$m\ddot{\tilde{z}} = -k(t)\tilde{z} - m\ddot{z}_0, \quad (4.11)$$

¹Despite the asymmetry of the Quantus chip, the position of the minimum of the potential does not vary significantly in the horizontal directions while decompressing the trap.

where the last term on the right hand side is the inert force, which depends on the acceleration of trap center. The numerical solution of equation 4.11 is shown in figure 4.5. After decompression, the atomic cloud oscillates in z -direction with a frequency equal to the vertical frequency of the holding trap ($\omega_z = 2\pi \times 10.53$ Hz). The amplitude of this oscillation depends critically on the duration of the decompression t_D . Increasing this time by a factor of three reduces the amplitude of the oscillation more than ten times. 0.75 s has been chosen as a compromise between minimizing the oscillation amplitude and maximizing the number of atoms that remain in the holding trap. Moreover, the smooth, gauss-like form of the ramp used to reduce the trap potential during decompression (Eq. 2.6 and Fig. 4.2) has been optimized to minimize the amplitude of the oscillation.

The calculated oscillation amplitude is $0.7 \mu m$, which is much less than the spatial extension of the condensate (Fig.4.4 b)) and is not to be resolved with the existing imaging system. Even after decreasing t_D on purpose, direct observation of the BEC oscillation in the trap is hardly possible. Instead, one can trace the periodic time dependence of the center-of-mass velocity. After decompression, the BEC is held in the shallow holding trap for a certain time t_{hold} . Its position and velocity in the trap are given by:

$$\begin{aligned} z_0(t_{hold}) &= z_0 + A \sin(\omega_z t_{hold} + \varphi_0) \\ v_0(t_{hold}) &= A\omega_z \cos(\omega_z t_{hold} + \varphi_0), \end{aligned} \quad (4.12)$$

with the oscillation amplitude A and some initial phase φ_0 . On the ground, after switching-off the trap, the condensate is accelerated by gravity and falls down. Its vertical position depends on both: the time t_{TOF} of free evolution and the holding time t_{hold} :

$$\begin{aligned} z(t_{TOF}, t_{hold}) &= z_0 + v_0(t_{hold})t_{TOF} + \frac{1}{2}gt_{TOF}^2 \\ &= z_{off} + A\omega_z \cos(\omega_z t_{hold} + \varphi_0)t_{TOF}. \end{aligned} \quad (4.13)$$

As already mentioned, the oscillation in the trap cannot be seen, therefore the time dependence of z_0 can be neglected. Figure 4.6 a) presents a series of measurements of the center-of-mass position z for a fixed time of flight $t_{TOF} = 24$ ms and variable t_{hold} (red squares). As expected from equation 4.13, the center-of-mass oscillates with the trapping frequency ω_z around the offset position $z_{off} = z_0 + 1/2gt_{TOF}^2$. The red solid line is a sine function fitted to the experimental data. Due to a slight tilt of the vertical axis of the trap, moving the trap in the z -direction also excites axial oscillation in x -direction (black line and squares). At the same time the tilt is sufficiently

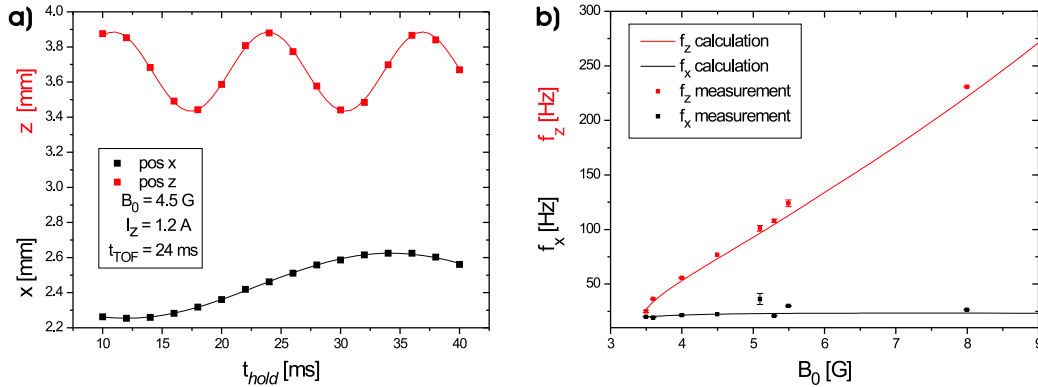


Figure 4.6: a) Measured oscillation in the z - (red) and x -direction (black) after $t_{TOF} = 24$ ms for a duration of the decompression $t_D = 110$ ms. b) Trapping frequency dependence on the bias field B_0 (the chip current $I_z = 1.2$ A).

small such that the field curvature along the principal axes of the trap and along the frame axes does not differ significantly.

Such measurement of the trapping frequencies has been performed for several final values of the bias field B_0 corresponding to different steepness of the holding trap. The result is depicted in figure 4.6 b). The solid lines give the calculated dependency of the trapping frequencies on B_0^2 . The experimentally found trapping frequencies (red and black squares) are in very good agreement with the theoretical prediction, which confirms the reliability of the simulation.

Note that each square in the left graph of figure 4.6 corresponds to running the complete experimental sequence once. It takes less than half a minute to collect one data point in the laboratory so that a complex measurement like that of figure 4.6 b) can be done within a few hours. However, things get more complex in microgravity. Since the drop tower facility allows to perform only three drops per day, a measurement of the trapping frequency can take several days. Nevertheless an effort to estimate the frequencies has been undertaken (Fig. 4.7). A slight discrepancy between the measured (fitted) and simulated frequencies is caused by the tilt of the principal axes of the trap (Fig. 3.7), which is not negligible for a decompressed trap in microgravity. Errors of the simulation are mainly due to the uncertainty of the dimension of the bias coils which has been assumed to be 0.5 mm.

²The gravitational potential has been included in the simulation.

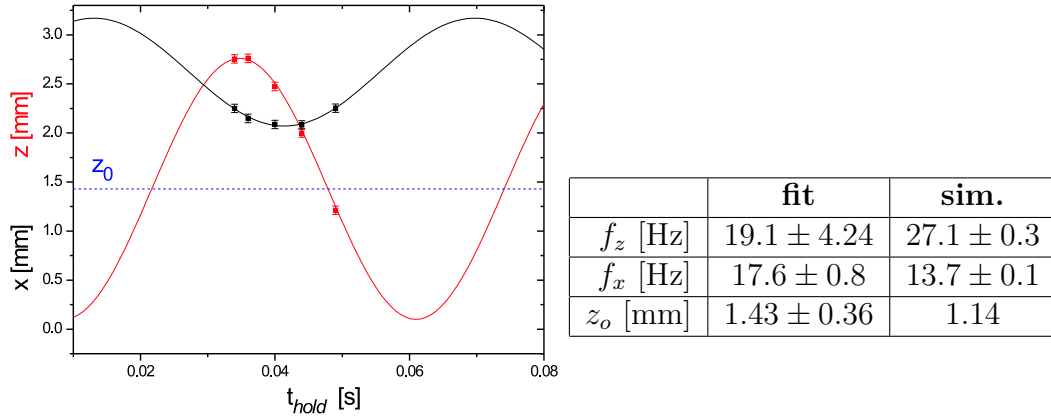


Figure 4.7: Measured oscillation in microgravity ($I_z = 2$ A and $B_0 = 2.4$ G).

4.3 Free expansion of the BEC in microgravity

4.3.1 Center-of-mass motion

The x - and z -position of the center-of-mass of the condensate during the time of flight was read out from absorption images and the results are depicted in figure 4.8. Whereas experimental data for the x -direction are in a good agreement with the theoretical prediction, we observe an unexpected large drift in the vertical direction. The corresponding acceleration in the z -direction is $a = 7.92 \times 10^{-3}$ m/s² for $t < 750$ ms. Moreover, a turning point at $TOF \approx 750$ ms makes the observation even more difficult to explain. Possible forces and boosts on the atoms are analyzed below, however none of them is sufficient for a conclusive interpretation of the data.

As will be shown in the next section, the analysis of the expansion data indicates the existence of a residual magnetic field focusing the atoms in the x -direction. The presence of such a field could also explain the much smaller horizontal displacement of the center-of-mass position.

4.3.2 Systematic errors

Initial velocity in the holding trap

Even though the decompression time of the magnetic trap and the shape of the ramp have been optimized, it is not possible to completely avoid a residual center-of-mass motion in the holding trap. The numerical solution

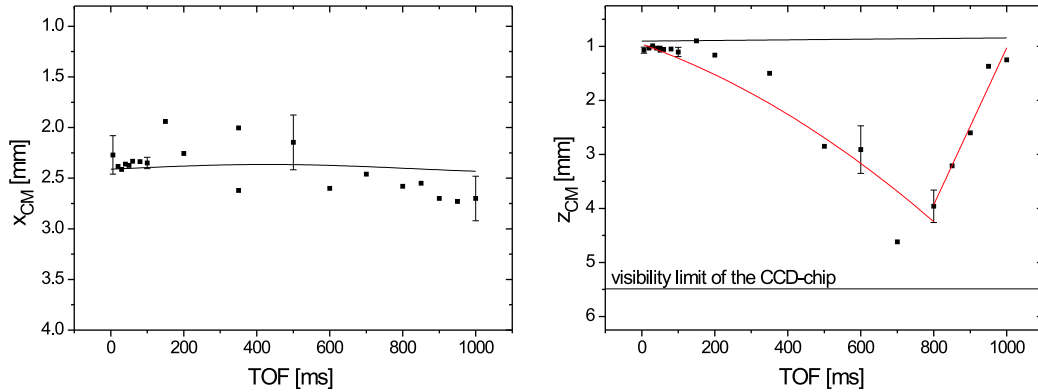


Figure 4.8: Center-of-mass position of the BEC during 1 s TOF. Error bars are standard deviations for the TOFs for which several measurements were done. Black lines are simulated with Eq. 4.10 in 3D with a residual trapping field in the x -direction ($\omega_x = 2\pi \times 0.34$ Hz). Red lines on the right graph are fits to the data and correspond to a hypothetical acceleration $a = 7.92 \times 10^{-3}$ m/s² for $t < 750$ ms and to a velocity $v = 14$ mm/s for $t > 750$ ms

of the 3D counterpart of equation 4.10 predicts an initial velocity of $V_x = 160$ $\mu\text{m/s}$ and $V_z = -60$ $\mu\text{m/s}$ after turning off the trap.

With our current controller we are able to switch off the chip current within less than one μs (the bias field is subsequently slowly ramped down within 50 ms). It is possible, that during the switching the condensate gets a "kick", which adds to its initial velocity. This issue however has not been investigated quantitatively within this thesis.

Residual air friction

The drop tube is evacuated to less than 20 mbar before each drop. Nevertheless, residual air pressure has a measurable effect on the falling capsule. Since friction of the residual air acts as a viscous force that is proportional to the velocity of the drop capsule, this force increases during the drop and decelerates the capsule by more than 10^{-5} g at the end of the drop³ (Fig. 4.9). During the third second of free fall, that is during the free expansion of the BEC, the residual deceleration is on the order of $0.5 - 1 \cdot 10^{-5}$ g. Obviously, this friction does not act on the condensate kept inside the ultra-high vacuum chamber, thus it falls a bit faster than the capsule. In other words, in the rest frame of the falling capsule an additional fictitious inertial force pushes

³Experiments, which require better μg -level can benefit from nested capsule assembly. It resembles the famous Russian toy Matryoshka (or Babushka), which is a set of dolls of decreasing sizes placed one inside the other

the condensate away from the chip (that is in the positive z -direction). In the worst case of $a = 10^{-4} \text{ m/s}^2$, the atoms would move by $50 \text{ } \mu\text{m}$ during the free expansion of 1 s.

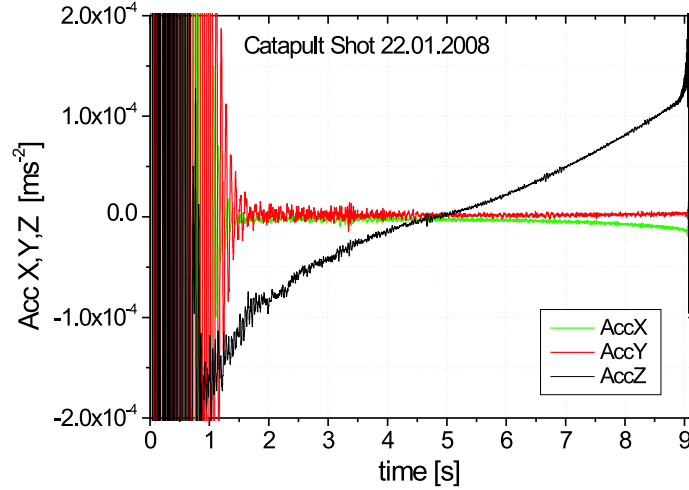


Figure 4.9: Acceleration in the drop capsule measured during a catapult shot. Residual air pressure in the drop tube results in a velocity dependent damping force on the capsule. Measurement with the ONERA SuperStar accelerometer; figure courtesy of H. Sellig (ZARM).

Residual magnetic field in the tower

The drop tube is composed of several steel cylinders with a height of 6 m each, put one on another and welded. Welding is liable to increase the amount of ferrite in the steel, consequently increasing its magnetic permeability. As a consequence, residual magnetic field inside of the drop tube features a spatial modulation with a period of $\approx 6 \text{ m}$ (Fig. 4.10). The spatial modulation of the field generates field gradients. With one flux-gate sensor, we were able to estimate the magnetic field gradient in the vertical direction only. However, since the diameter of each cylinder is greater than its height, it is reasonable to assume that the horizontal components of the gradient are at most of the same order as the vertical ones. During the free expansion of the BEC the highest gradient in the z -direction would cause an acceleration of at most $3 \cdot 10^{-5} \text{ m/s}^2$. Note however, that the spatially oscillating field has a gradient that changes its sign, therefore the average force on the atoms should vanish.

It should be pointed out that the above estimate of the field gradient relies on a measurement that has been performed with a single layer of μ -metal screening (Fig. 4.10). With the second layer mounted later on both,

the DC-offset and the amplitude of the modulation are further reduced by approximately a factor of three.

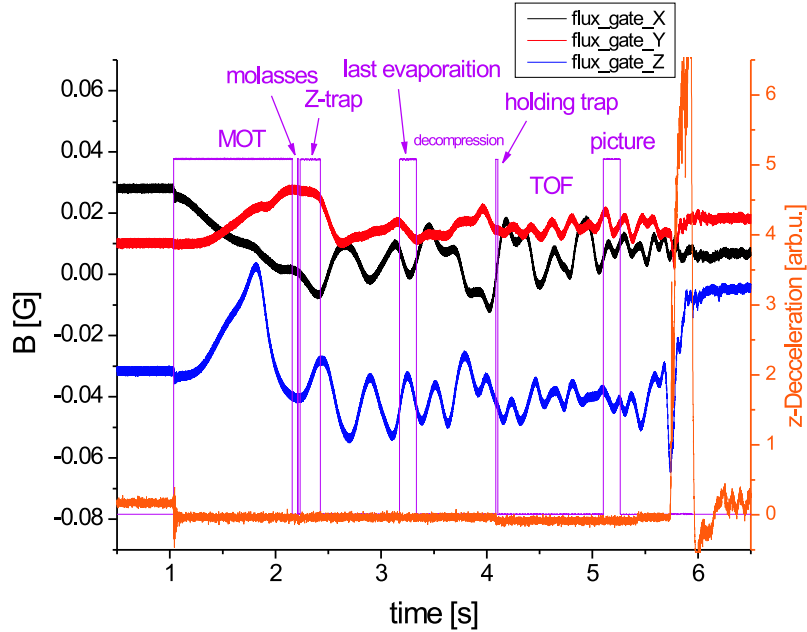


Figure 4.10: Residual magnetic field along the symmetry axis of the drop tube measured inside a single layer of μ -metal screening. Digital timing markers (pink) indicate precisely the phases of the experiment during the drop.

Inhomogeneity of the Helmholtz-field

As described in section 2.4, in order to define a quantization axis, a homogeneous magnetic field of 0.8 G in the y -direction is kept on during TOF. The field is generated by a pair of Helmholtz coils, the same as used for the bias field in the magnetic trap. The field of the Helmholtz coils is most homogeneous along the symmetry axis of the coils. However, this is located 5 mm below the chip surface, 3-4 mm above the center-of-mass of the freely expanding condensate. This motivated us to simulate the inhomogeneity of the coil field in detail. The results are presented in figure 4.11. One can see, that the weak-field-seeking atoms will be pushed towards the chip surface if the average distance between the coils is greater than their radius⁴ (blue curves Fig. 4.11 b) and c)). However, even with an inaccuracy of 0.5 mm in

⁴If the distance is smaller than the radius, the magnetic field has a minimum at the center between the coils, the gradient has opposite sign but the same absolute value.

coil fabrication, which is well beyond the tolerances that are typically guaranteed by any mechanical workshop, the resulting acceleration at the place of the atoms is only on the order of $5 \cdot 10^{-5} \text{ m/s}^2$.

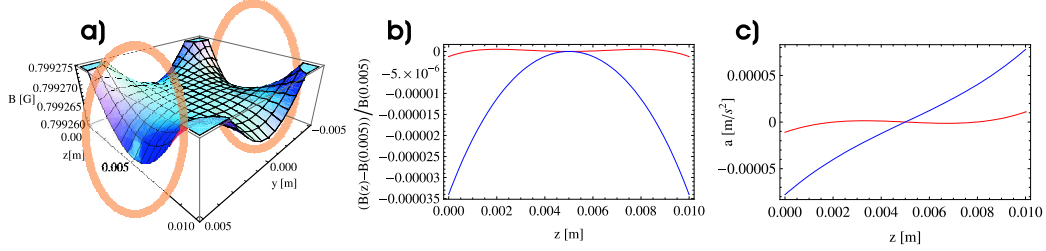


Figure 4.11: Inhomogeneity of the Helmholtz-coil generating the bias magnetic field B_0 . The coils have an average radius $r = 90 \text{ mm}$ (not to scale in graph a)) and $N = 100$ windings forming a 10×10 square wire matrix. The symmetry axis of the coils is located at $z = 5 \text{ mm}$ ($z = 0$ refers to the chip surface). b) Relative deviation from the field value in the center and c) the field gradient (in units of acceleration of a Rb atom) for ideal coils with an average distance $d = r$ (red) and for coils with $d = 90.5 \text{ mm}$ (blue). Plots were made for $I = 0.08 \text{ A}$

Ion-getter pump

The ion-getter vacuum pump, which is equipped with two strong permanent magnets, is located on the platform above the vacuum chamber at an average distance of 0.5 m from the atom chip. Based on the pump's data sheet we reconstructed the radial magnetic field gradient at the place of the BEC to be $B'(r) = 3.5 \cdot 10^{-4} \text{ G/cm}$. This corresponds to an acceleration $a = 2.2 \cdot 10^{-4} \text{ m/s}^2$ pointing downwards, that is in the positive z -direction. The pump however has its own 3 mm thick μ -metal screen, which together with the screen surrounding the vacuum chamber should reduce the gradient by at least a factor of 30.

Residual charge on the chip

The chip current is actively stabilized to zero during the free expansion. We noticed however that there is an electric potential difference $\Delta u = 0.6 \text{ V}$ between the Z-wire and the vacuum chamber when the chip current is off. Thus, there must be an inhomogeneous electric field $E(r)$ inside of the vacuum chamber. In order to estimate its strength, we consider the Z-wire and the walls of the vacuum chamber to form a cylindrical capacitor with an

inner radius equal to the width of the wire $r_1 = 30 \mu\text{m}$ and the outer radius equal to the distance of the chip to the wall: $r_2 \approx 5 \text{ cm}$. Then the electric field decreases with the distance r from the chip as: $E(r) = \Delta u / (r \ln(r_2/r_1))$.

A neutral rubidium atom placed in a static electric field E exerts an energy shift: $\Delta U = \frac{1}{2}\alpha E^2$, where $\alpha = 0.0794 \text{ MHz}/(\text{kV}/\text{cm})^2$ is the DC-polarisability of the ground state. Inserting the above expression for $E(r)$ yields a $1/r^2$ dependence of the potential energy and a $1/r^3$ dependence of the force. Quantitatively, at $r = 1 \text{ mm}$ an atom would exert an acceleration towards the chip surface of $a = 2.4 \times 10^{-7} \text{ m/s}^2$ - much smaller than any other effects considered.

The atom chip is composed of several micro strip lines (Fig. C.1), only two of which are connected to the current controller and used in the experiment. Since the unused wires are not grounded, it is possible that they couple capacitively to the other wires and gather a static charge. This effect however has not been investigated quantitatively so far, but it is hard to imagine, that the induced voltage exceeds 1 V. Nevertheless, the unused wires will definitely have to be grounded for the next drop campaigns.

4.3.3 Free (?) expansion

The axial and the radial size of the BEC was determined from absorption images for different times of flight (Fig.1.7 and 4.12). The measured radial size is in good agreement with the numerical simulation. However, the condensate expands much less than expected in the axial direction. Its final axial size of approx. $150 \mu\text{m}$ after 1 s of TOF is unphysical, which can be deduced from the following consideration. First, as described in section 3.2.2, when decompressing the microtrap by reducing the bias field, only one trapping frequency can be reduced to zero, whereas the two other frequencies reach their finite saturation values of $\omega_y = 2\pi \times 12$, $\omega_z = 2\pi \times 21 \text{ Hz}$ for the Quantus chip. Since the expansion parameters λ_i are coupled (Eq. 4.5) these two frequencies increase the expansion speed also in the axial direction. Minimizing ω_x slows down the expansion but simultaneously increases the axial size of the ground state in the holding trap. For $\omega_x = 2\pi \times 0.3 \text{ Hz}$ the axial size would be approx. $150 \mu\text{m}$ in the holding trap and it would increase more than twice after 1 s TOF. Even more, a trap with such low frequency would not be able to hold 10000 atoms, since the potential barrier is much lower than the chemical potential (Fig. 3.12).

Much slower axial expansion would be possible with lower radial frequencies of the holding trap ω_y and ω_z . This would however slow down the radial expansion and the measured radial size would not fit the simulation.

This inconsistency in the size of the expanding BEC suggests the existence

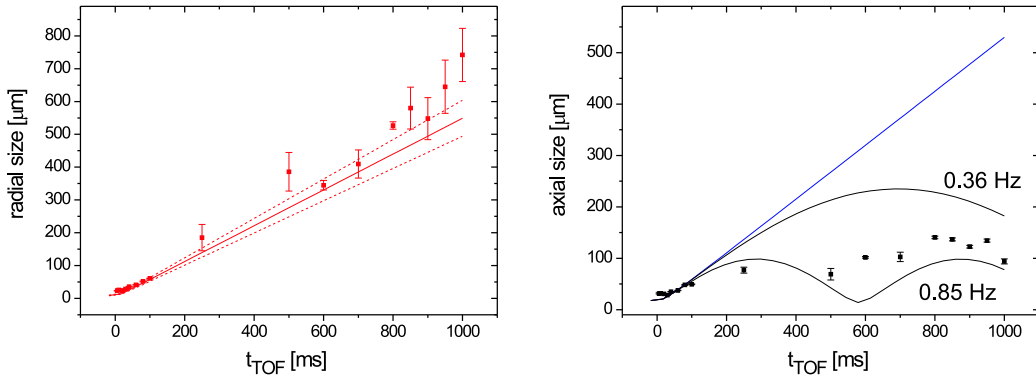


Figure 4.12: Expansion of the BEC during 1 s TOF. Left: radial size (z -direction), right: axial size (x -direction). Squares are extracted from inverted parabola fits to absorption images normalized to $N=10000$ atoms. Red and blue solid lines are projections on the z - and x -axes of the 3D condensate density calculated with equation 4.8. The red dashed lines reflect the 10% uncertainty level of the simulation due to an assumed 0.5 mm inaccuracy in the fabrication of the bias coils. Black solid lines simulate the axial expansion in the presence of a residual focusing field with a frequency of $2\pi \times 0.36$ and $2\pi \times 0.85$ Hz respectively. The existence of such a field would not affect the radial size.

of a residual force focusing the atoms in axial direction. Such a field can be modeled by a nonzero element Ω_{11} of the Hessian matrix. The sudden release of the condensate into a residual trap whose frequency is much smaller than that of the holding trap is not an adiabatic process. Thus, the condensate axial width oscillates in a breathing mode. Additionally, since the axis of the residual trap does not coincide with that of the holding trap, the y -axis of the expanding condensate undergoes a torsional oscillation. Both oscillation modes lead to an effective periodic change of the axial width that is seen by the camera. The black solid curves in the right graph in figure 4.12 illustrate the axial expansion in the presence of a residual field with a minimum at $x = 0$ and a harmonic frequency of $2\pi \times 0.36$ and $2\pi \times 0.85$ Hz respectively. The experimental data clearly indicate the presence of a sub-Hertz residual field. The source of this field could be for instance a residual magnetization of the vacuum chamber.

Note that the blue and black curves in figure 4.12 do not differ significantly for the free expansion times accessible in earth-bound experiments (TOF < 100 ms). However, after one second of free expansion the size of the condensate released from a trap with the initial frequency $\omega_x = 2\pi \times 4.5$ Hz can differ by a factor of 3 due to the presence of a weak residual trap with a

harmonic frequency of $\omega_{res} = 2\pi \times 0.36$ Hz. The field of such a trap varies only by a few μG over the spatial scale of $200 \mu\text{m}$ considered here. This indicates that a freely expanding quantum gas might potentially offer a high sensitivity for measurements of extremely small magnetic fields.

Free expansion of a thermal cloud

The hypothesis of a residual field confining the atoms in the x -direction was confirmed by measuring the expansion of the thermal cloud (Fig. 4.13). Atoms with a temperature $T = 23$ nK were prepared by aborting the RF-evaporation 40 kHz above the transition to BEC and subsequent decompression of the trap. The density distribution of the confined thermal atoms reflects the shape of the potential (the very left absorption image in Fig. 4.13). However, a thermal cloud should expand isotropically after switching off the trap. This means, that for free expansion times larger than $1/\omega$ the density distribution should become spherically symmetric. From the absorption images in figure 4.13 it can clearly be seen that the aspect ratio of the cloud $\eta(t) = \sigma_x(t)/\sigma_z(t)$ does not saturate to unity but further decreases for $t > 100$ ms.

Since the radial size of the cloud $\sigma_z(t)$ is not affected by the presence of the residual field, one can estimate the temperature of the cloud by means of ballistic expansion in the z -direction (Fig. 4.13 bottom left graph). The width of the freely expanding thermal gas is given by: $\sigma_z(t) = \sqrt{\sigma_z^2(0) + v^2 t_{TOF}^2}$ with an initial width $\sigma_z(0)$ and a mean expansion velocity $v = \sqrt{k_B T/m}$. The best fit to the expansion data (red curve), with $\sigma_z(0)$ and T as fit parameters, yields $23(\pm 2.5)$ nK for the temperature. The black curve (bottom right graph) characterizes the free axial expansion with this temperature. Only for short expansion times ($t_{TOF} < 50$ ms) the axial widths fit the free expansion model with $T = 23$ nK. For longer times the influence of the residual trap can not be neglected and the expansion is slowed down. Expansion in the presence of a harmonic field can be modeled by substituting $v \rightarrow v(t_{TOF}) = \sqrt{k_B T/m - \bar{a} t_{TOF}}$ where $\bar{a} = \frac{1}{2}\omega_x^2 \sigma_x^{max}$ is the average acceleration on a cloud expanding to a maximum width σ_x^{max} . This expansion model with $\sigma_x^{max} = 187 \mu\text{m}$ and $\omega_x = 2\pi \times 0.85$ Hz is represented by the blue solid line. Clearly, the measured widths of the thermal cloud confirms the existence of a weak sub-Hertz residual trap in axial direction.

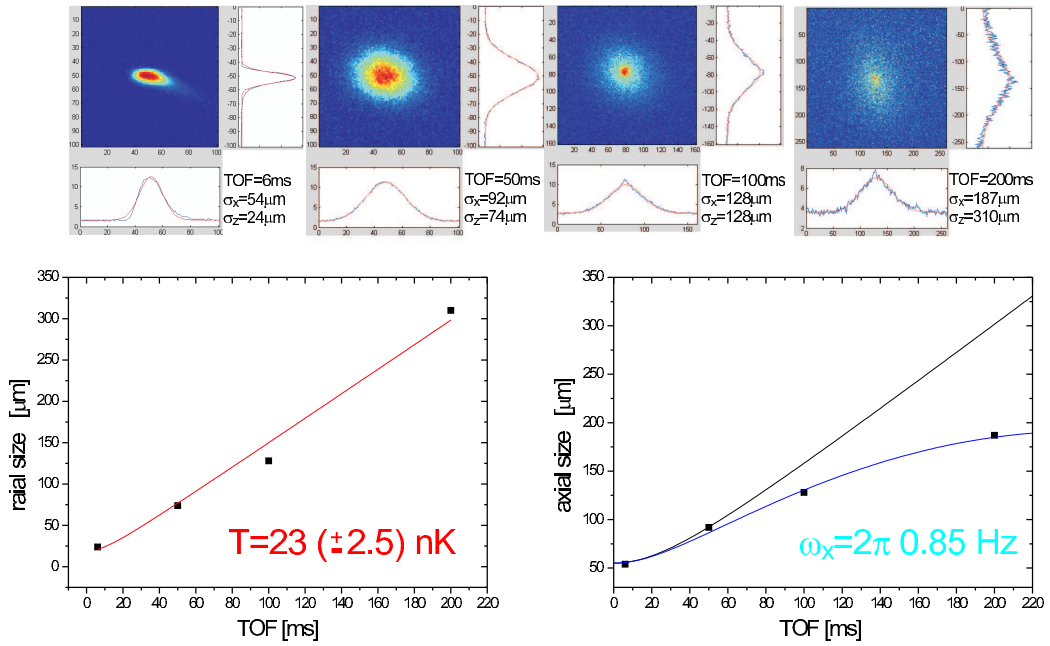


Figure 4.13: Ballistic expansion of an ultra cold thermal cloud: absorption images and their projections on the x - and z -axis taken after various times of flight (upper row). The red line in the bottom left graph is the best fit to the data (black squares) with the temperature as a fit parameter. The black curve in the bottom right graph characterizes the free axial expansion with a temperature $T=23 \text{ nK}$. The blue curve describes axial expansion in the presence of a weakly confining field in the x -direction with a harmonic frequency $\omega_x = 2\pi \cdot 0.85 \text{ Hz}$.

Chapter 5

Future perspective

5.1 BEC in a magnetic insensitive state

In the last chapter the unexpected movement of the condensate center-of-mass (Fig. 4.8) as well as the focusing effect in the x -direction during the free expansion (Fig. 4.12) were presented. Both effects indicate the existence of residual forces on atoms in the absence of the trapping potential. In order to confirm or exclude the magnetic character of these forces, preparation of atoms in the magnetic insensitive state $m_F = 0$ is currently being implemented. Since for an effective and fast evaporative cooling a high atom density and a steep trap is required, we plan to leave the atoms in the $m_F = 2$ state during the evaporation. Transfer to the $m_F = 0$ state will be performed after the decompression phase, directly before the free expansion.

Coherent population transfer between the Zeeman states is possible with the use of an adiabatic rapid passage (ARP). This quantum mechanical effect takes place when an electromagnetic field, coupling two levels of an atomic or molecular system, is frequency-swept across the resonance. The ARP was first observed in nuclear magnetic resonance [Bloch, 1946]. However the phenomenon is quite general and was demonstrated in optically induced electronic transitions [Ekstrom et al., 1999] and recently between the hyperfine and Zeeman transitions in the alkali atoms [C.Camparo and Frueholz, 1984].

A common way to explain the ARP is to use the dressed-atom approach [Camparo and Frueholz, 1984]. For a two-level atomic system, the dressed state Hamiltonian is given by:

$$H = \frac{1}{2}\hbar \begin{bmatrix} \delta & \Omega_R \\ \Omega_R^* & \delta \end{bmatrix} \quad (5.1)$$

with the eigenenergies $\pm \frac{1}{2}\hbar\sqrt{\Omega_R^2 + \delta^2}$. The Rabi frequency Ω_R describes the

coupling strength between the levels and δ is the detuning of the coupling field from the resonance. If we denote by $|1\rangle$ and $|2\rangle$ the eigenstates of the system "atom + field" without coupling ($\Omega_R = 0$), we find the normalized eigenvectors of 5.1 (the dressed states) to be the mixtures of the pure states:

$$\begin{aligned} |\phi_1\rangle &= \frac{\delta + \sqrt{\Omega_R^2 + \delta^2}}{\Omega_R \sqrt{1 + \left(\frac{\sqrt{\Omega_R^2 + \delta^2} + \delta}{\Omega_R}\right)^2}} |1\rangle + \frac{1}{\sqrt{1 + \left(\frac{\sqrt{\Omega_R^2 + \delta^2}}{\Omega_R}\right)^2}} |2\rangle \\ |\phi_2\rangle &= \frac{\delta - \sqrt{\Omega_R^2 + \delta^2}}{\Omega_R \sqrt{1 + \left(\frac{\sqrt{\Omega_R^2 + \delta^2} - \delta}{\Omega_R}\right)^2}} |1\rangle + \frac{1}{\sqrt{1 + \left(\frac{\sqrt{\Omega_R^2 + \delta^2} - \delta}{\Omega_R}\right)^2}} |2\rangle. \end{aligned} \quad (5.2)$$

Introducing the mixing angle θ defined by $\tan(2\theta) = \Omega_R/\delta$, expressions 5.2 simplify to

$$\begin{aligned} |\phi_1\rangle &= \cos(\theta) |1\rangle + \sin(\theta) |2\rangle \\ |\phi_2\rangle &= -\sin(\theta) |1\rangle + \cos(\theta) |2\rangle. \end{aligned} \quad (5.3)$$

The ARP occurs when the atom-field system enters and leaves the avoided crossing region ($\delta = 0$) in the same dressed state. For example, if an atom is initially prepared in the state with higher energy and the passage starts with $\delta < 0$, then $\theta = \pi/2$ and the dressed atom wave function is well approximated by $|2\rangle$ (Fig. 5.1 a). Now the frequency of the coupling field is adiabatically swept through the resonance. After the passage, for $\delta > 0$, $\theta \rightarrow 0+$ and $|\phi_2\rangle$ is well approximated by $|1\rangle$: the atom is in its lower energy eigenstate. Thus, if the dressed state does not change as the system traverses the avoided crossing region, the population is reversed.

For the ARP to occur the frequency sweep rate is required to be high (rapid) with respect to the relaxation processes in the system, and at the same time slow enough so that the system can follow adiabatically the frequency sweep. For the Zeeman sub-levels of the atomic ground state relaxation mechanisms can be neglected. Thus there is only an upper bound on the passage speed, which can be expressed as [Camparo and Frueholz, 1984]:

$$\frac{d\delta}{dt} \ll \Omega_R^2. \quad (5.4)$$

Figure 5.1 b) shows the dressed states of the $^{87}\text{Rb} \left| 5^2S_{1/2}, F = 2 \right\rangle$ manifold in the presence of a constant magnetic field $B_0 = 30$ G as a function of the frequency of the applied RF field. During the passage, the atom initially in the $m_F = 2$ state passes twice through the avoided crossing region (circles) and thus the population is twice coherently transferred between the Zeeman

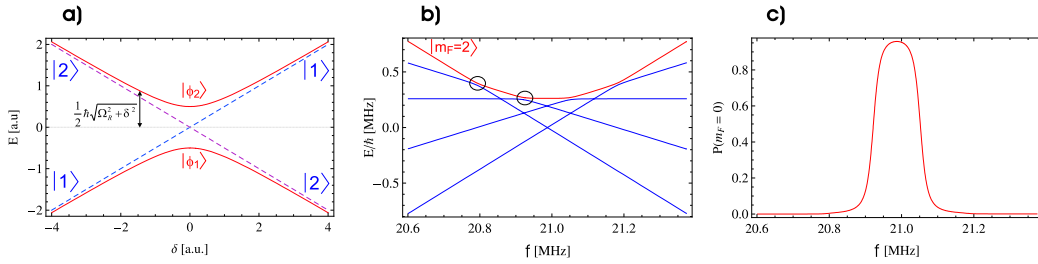


Figure 5.1: a) energy of a two level dressed atom without interaction (blue dashed) and with $\Omega_R = 1$ (red) as a function of the detuning δ of the coupling field. For large δ the dressed atom wave function and the corresponding energy coincide with those in the absence of the interaction; b) dressed energies of the ^{87}Rb $F = 2$ ground state in the presence of a 30 G bias field as a function of the RF-field frequency. Red line describes the energy of the state which for large δ coincides with the $m_F = 2$ pure state; c) probability to find the atom in the $m_F = 0$ state.

states. For $f = 20.92$ MHz the probability to find the atom in the $m_F = 0$ state is more than 95% (Fig. 5.1 c). The graphs were made for $\Omega_R = 10$ kHz. The passage would have to take longer than 40 ms in order to fulfill the adiabaticity condition 5.4.

Technically, the radio frequency for the ARP will be generated from a 40 MHz arbitrary function generator from National Instruments (NI PXI-5406). The signal will be amplified to a few Watt RF-power and coupled to the atoms with a single coil mounted inside of the vacuum chamber. This coil was originally intended to be used for evaporating cooling.

5.2 Bragg diffraction of the condensate

One of the simplest atom interferometry experiments that can be implemented in the existing apparatus is the Bragg diffraction of the condensate. The Bragg scattering of matter de Broglie waves on a grating formed by a standing light wave is in atom optic the analogon of a light diffraction on solid structures. In both cases the incident beam must satisfy the Bragg condition on the angle of incidence θ : $d \sin \theta = n \lambda$, where $n = 0, 1, 2, \dots$ is the diffraction order, d is the grating constant (or half of the optical wavelength of the standing wave) and λ is the wavelength of the incident light (or the de Broglie wavelength $\lambda_{DB} = h/p$ of the incident atom beam with the momentum p).

The diffraction of a matter wave on the standing wave can be understood

in terms of the position dependent phase shifts. Light tuned far from an atomic resonance shifts the energy levels of the atoms (light shifts). An energy shift applied for a time interval causes accumulation of a phase of the atomic wave function. Thus, a standing light wave acts as a phase grating for matter waves. Alternatively, the Bragg process can be also explained as a coherent photon exchange between the counter propagating components of the standing wave. Absorption of a photon from one beam by the atom is followed by a stimulated emission into the other beam. Thus the atom gains a discrete momentum change of $2\hbar k$ along the k vector of the standing wave (Fig. 5.2 a)).

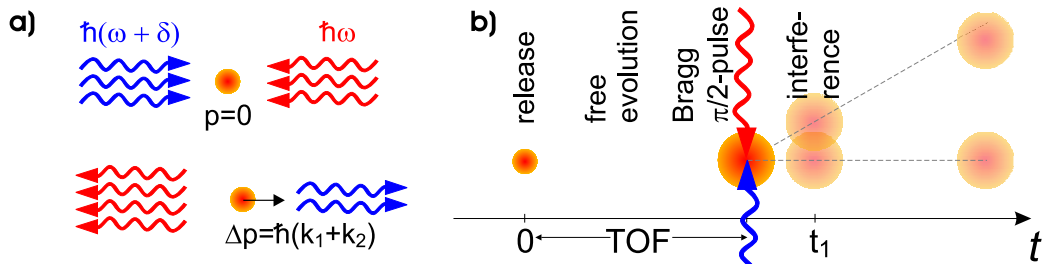


Figure 5.2: a) Bragg diffraction can be interpreted as an absorption of a photon from one beam followed by stimulated emission into the other beam. b) Proposed timing for the coherence study of the BEC.

The Bragg scattering was first observed at MIT [Mar et al., 1988] and first demonstrated with atoms in a Bose Einstein condensate at NIST [Kozuma et al., 1999]. The first order diffraction can be viewed as a coherent two-photon transition from a ground state with an initial momentum to the same ground state with a new momentum. As an atom pass through the standing wave, its momentum-space wave function will oscillate between the two coupled momentum states in a manner analogous to the Rabi oscillation of atomic population between two resonantly coupled states. The effective oscillation frequency is [Giltner et al., 1995]: $\Omega_{eff} = \Omega_1\Omega_2/2\Delta$, where $\Omega_{1,2}$ are the resonant Rabi frequencies of the two Bragg beams, and Δ is the detuning of the beams from the optical transition. By adjusting either of both: the interaction time or Ω_{eff} the population can be coherently transferred from one momentum state to the other with the efficiency varying from 0 to 100%. In particular, applying a $\frac{\pi}{2}$ - or a π -pulse will transfer 50% and 100% of the population respectively. Therefore, Bragg scattering provides us with the critical atom-optic elements (beam splitter, mirror) needed for constructing an atom-laser interferometer.

In contrast to the diffraction of an atomic beam, we plan to perform a diffraction experiment on the stationary condensate (similarly as described

in [Kozuma et al., 1999]). In this case the interaction time is not determined by the time of flight through the standing wave. Rather the duration of the laser pulse is varied. The Bragg condition on the angle of incidence becomes a condition on the frequency difference δ of the two counter propagating laser beams. For the first diffraction order the energy conservation requires:

$$\hbar\delta = \frac{\hbar^2(k_1 + k_2)^2}{2m}, \quad (5.5)$$

where m is the atomic mass and $k_{1,2} = 2\pi/\lambda_{1,2}$ are the wave numbers of the two beams. For the D2 transition in Rb $\lambda_1 \approx \lambda_2 = 780$ nm and 5.5 yields $\delta = 2\pi \times 15.1$ kHz. This frequency difference can be experimentally realized with two acousto-optic modulators.

Partial Bragg splitting of the condensate with a $\frac{\pi}{2}$ -pulse can be utilized to investigate the decoherence time of the BEC (Fig. 5.2 b). The $\frac{\pi}{2}$ -pulse applied after the free evolution time (TOF) will split the condensate. A few ms after the splitting (this time should be short enough in order not to separate totally the two clouds) an absorption image will be taken. For TOFs shorter than the decoherence time, an interference pattern is expected to be seen.

5.3 The QUANTUS II project

At the time when an end is brought to the adiabatic process of writing this thesis, a new generation of young scientists is intensely working on the second generation of the Quantus experiment. Their affords will be soon visualized by assembling of a drop capsule, which is, briefly, twice smaller and can do twice more than the existing one. To be more precise, the following aspects are taken into consideration by the construction of the Quantus II apparatus:

Catapult capability

The new experimental setup is exclusively designed for being launched with the catapult. This puts stringent demands on the construction of the capsule (Tab. 2.1). In particular the net weight has to be reduced by 30% and the payload volume squeezed by almost a factor 2. Further miniaturization of the system is therefore required. Components with the highest potential for the size reduction are: the board batteries and the computer, the vacuum chamber, control electronics and the laser optical board. Concerning the laser system, a hybrid master laser and a hybrid MOPA are being currently developed at the Ferdinand-Braun-Institut für Höchstfrequenztechnik (FBH) in Berlin. Hybrid systems [Paschke et al., 2002; Schwertfeger et al., 2004] contain laser chip, beam-shaping optics, external resonators, and oscillator-amplifier mounted on a micro-optical bench with the spatial size of several

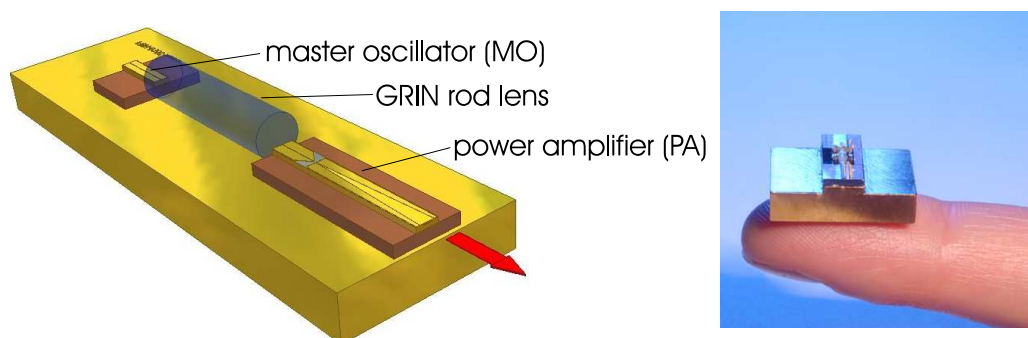


Figure 5.3: MOPA components on a micro-optical bench (schematic left and the real size photo right). Picture courtesy of the Ferdinand-Braun-Institut für Höchstfrequenztechnik (FBH) in Berlin.

mm (Fig. 5.3). Apart from the reduced volume, an obvious advantage of miniaturized lasers is their low sensitivity to external acoustic vibrations. This will be beneficial for the frequency stability during the catapult launch.

Increased number of atoms

Increasing the number of condensed atoms by at least one order of magnitude is one of the most important issues of the QUANTUS II setup. As described in reference [Wildermuth et al., 2004] with the use of a mesoscopic U-shaped current-carrying Cu structure it is possible to collect more than 3×10^8 ^{87}Rb atoms in a mirror magneto-optical trap without using external quadrupole coils. This is an important achievement towards mass reduction, since our MOT coils are the largest in the whole setup (Fig. 2.6). The authors of [Wildermuth et al., 2004] are able to load roughly 2×10^8 atoms to the magnetic Ioffe-Pritchard trap generated by a Z-shaped wire structure. The maximal chip-current for the magnetic trap is up to 60 A. Finally the Bose-Einstein condensation of 10^5 atoms occurs.

The new chip should additionally allow for further decompression of the trapping potential characterized by sub-Hz harmonic trapping frequencies. This will enable much slower expansion of the BEC released from the trap. Observation times of a few seconds will be accessible with the catapult.

Another feature of the Quantus II setup is an atom loading mechanism basing on a two-dimensional magneto-optical trap (2D-MOT) [Dieckmann et al., 1998]. The atoms will be captured from the background gas in the high pressure source chamber (Fig. 5.4). Cooling in two dimensions will allow for the generation of a slow beam of cold atoms which will load the mesoscopic U-MOT placed in a second, ultra-low pressure chamber. Due to the absence of the Rb dispenser in this vacuum chamber the background gas pressure can be reduced to 10^{-11} mbar. This promises to enhance the

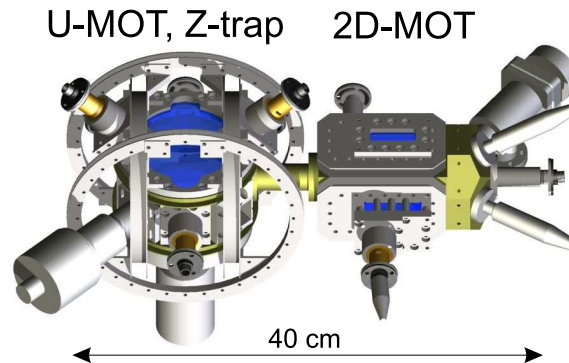


Figure 5.4: A compact double-MOT vacuum chamber for the QUANTUS II experiment. Picture courtesy of Waldemar Herr (IQO Hannover)

lifetime of atoms in the magnetic trap and that of the condensate.

An important point in the design of the new vacuum chamber was extended optical access. Compared to the existing setup, the new chamber provides input for Raman beams and possibly for the optical dipole trap. Moreover, there are two perpendicular view ports for the CCD cameras to increase the amount of information gathered with the absorption or fluorescence imaging.

Atom interferometry with the QUANTUS II

As discussed in chapter 1 atom interferometry is one of those fields of quantum physics, which can benefit from the microgravity environment. The Quantus II aims at inertial sensing experiments with the use atom interferometer with the quantum-degenerated gases. For such experiments a Raman laser is required. The activities to construct a catapult capable Raman laser has already begun in our group. One approach is to extend the existing "block" design (Fig. 2.17) by an external cavity in order to minimize the laser linewidth to approx. 100 kHz. Two such narrow band lasers could be easily phase-locked and thus could serve as the Raman laser. Since the frequency stability of an ECDL is extremely sensitive to the mechanical disturbances, it is a challenge to design a laser that will operate reliably during the catapult launch. An alternative is to use the current "block" design with a DFB Diode and to phase-modulate the light at 6.8 GHz (for instance with a fiber phase modulator). The sidebands will be used selectively to injection-lock two FP diodes. If necessary, the light will be amplified in a TA.

Quantum gas mixtures

One of the most important modifications of the Quanus II setup is a possibility to perform interferometric experiments with two atomic species, bosonic ^{87}Rb and fermionic ^{40}K simultaneously. Applications such as a test of the Einstein's equivalence principle are scheduled. The equivalence principle has been tested on Earth by comparing the gravitational acceleration of the two isotopes ^{85}Rb and ^{87}Rb to a 10^{-7} accuracy level [Fray et al., 2004]. Using diverse atomic species, whose mass differs substantially, can further improve the current accuracy limit.

Appendix A

Harmonic frequencies in a three-dimensional trap

Given a three-dimensional, time dependent, smooth¹ potential $U(x, y, z, t)$ having a critical point at $\vec{r}_0(t) = \begin{bmatrix} x_0(t) \\ y_0(t) \\ z_0(t) \end{bmatrix}$. Since the first partial derivatives of U are equal zero at the critical point, Taylor expansion of U around \vec{r}_0 , up to the second order terms in \vec{r} can be written in a form:

$$U(x, y, z, t) - U_0(t) = \frac{1}{2} [x - x_0(t), y - y_0(t), z - z_0(t)] \Omega(t) \begin{bmatrix} x - x_0(t) \\ y - y_0(t) \\ z - z_0(t) \end{bmatrix} \quad (\text{A.1})$$

with $U_0(t) = U(\vec{r}_0(t))$ and a symmetric second partial derivative matrix

$$\Omega(t) = \begin{bmatrix} \frac{\partial^2 U}{\partial x^2} & \frac{\partial^2 U}{\partial x \partial y} & \frac{\partial^2 U}{\partial x \partial z} \\ \frac{\partial^2 U}{\partial y \partial x} & \frac{\partial^2 U}{\partial y^2} & \frac{\partial^2 U}{\partial y \partial z} \\ \frac{\partial^2 U}{\partial z \partial x} & \frac{\partial^2 U}{\partial z \partial y} & \frac{\partial^2 U}{\partial z^2} \end{bmatrix} \Bigg|_{\substack{x = x_0(t) \\ y = y_0(t) \\ z = z_0(t)}}$$

also called the Hessian matrix of U or simply the Hessian.

Classification of the critical point

There is:

- a local minimum at \vec{r}_0 if all eigenvalues of Ω are positive,
- a local maximum at \vec{r}_0 if all eigenvalues of Ω are negative,

¹continuous with continuous all first and second partial derivatives

- a saddle point at \vec{r}_0 otherwise (if none of the eigenvalues of Ω equals zero).

Orthogonal diagonalization of Ω

The right hand side of the equation A.1 is a polynomial that is quadratic in the variables x, y, z and is in general called a quadratic form associated to the matrix Ω .

Spectral theorem yields: A square matrix Ω can be diagonalized via an orthonormal change of basis if and only if the matrix Ω is symmetric. In particular, all of the eigenvalues of a symmetric matrix are real and an orthonormal basis of eigenvectors can be found. These basis vectors are called the principal axes of the matrix Ω .

In the other words, there is an orthogonal matrix \mathbf{P} whose columns build an orthonormal basis, and $\mathbf{P}^{-1}\Omega\mathbf{P} = \mathbf{P}^T\Omega\mathbf{P} = \mathbf{D}$, where \mathbf{D} is a diagonal matrix whose diagonal entries are the (real) eigenvalues λ_i of Ω . Thus $\Omega = \mathbf{P}\mathbf{D}\mathbf{P}^T$. If we denote $\mathbf{d} = \vec{r} - \vec{r}_0$ we can find a new coordinate system defined

by $\mathbf{r}' = \mathbf{P}^T\mathbf{d} = \mathbf{P}^{-1}\mathbf{d} = \begin{bmatrix} x' \\ y' \\ z' \end{bmatrix}$ in which the potential has a particular simple form:

$$\begin{aligned} U(x, y, z) - U_0 &= \\ &= \frac{1}{2}\mathbf{d}^T\Omega\mathbf{d} = \frac{1}{2}\mathbf{d}^T\mathbf{P}\mathbf{D}\mathbf{P}^T\mathbf{d} = \frac{1}{2}(\mathbf{P}^T\mathbf{d})^T\mathbf{D}(\mathbf{P}^T\mathbf{d}) = \frac{1}{2}\mathbf{r}'^T\mathbf{D}\mathbf{r}' = \\ &= \frac{1}{2}(\lambda_1x'^2 + \lambda_2y'^2 + \lambda_3z'^2). \end{aligned} \quad (\text{A.2})$$

If all λ_i are positive, A.2 resembles the equation of an ellipsoid:

$$\frac{x'^2}{a^2} + \frac{y'^2}{b^2} + \frac{z'^2}{c^2} = 1,$$

whose semi-axes a, b and c overlap with axis of the new primed coordinate system. Furthermore, second partial derivatives $\frac{\partial^2 U}{\partial x_i'^2}$ are equal to the eigenvalues λ_i of the Hessian. Thus, the harmonic frequencies of the trapping potential along x'_i -direction for a particle with the mass m are given by:

$$\omega_i(t) = \sqrt{\frac{\lambda_i(t)}{m}}. \quad (\text{A.3})$$

Appendix B

Magnetic field of a finite piece of wire

B.1 Infinitely thin conductor

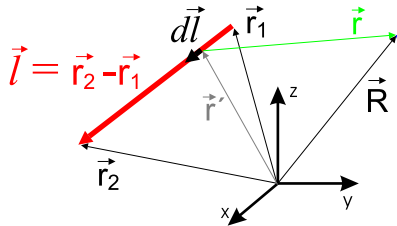


Figure B.1: Magnetic field at the place $\vec{R} = [x, y, z]$ generated by a finite piece of an infinitely thin wire represented by the vector \vec{l} .

A finite piece of an infinitely thin wire, situated at an arbitrary place in space, can be defined by two vectors pointing at the ends of the wire: $\vec{r}_1 = [r_{1x}, r_{1y}, r_{1z}]$, $\vec{r}_2 = [r_{2x}, r_{2y}, r_{2z}]$ (Fig. B.1). The "wire vector" $\vec{l} = \vec{r}_2 - \vec{r}_1 = [l_x, l_y, l_z]$ shows the direction of the electric current flow. In order to calculate the line integral given by the equation 3.16, one has to parametrize integration path:

$$\vec{l}(t) = \begin{bmatrix} l_x t \\ l_y t \\ l_z t \end{bmatrix}, t \in [0, 1], \quad d\vec{l} = \begin{bmatrix} l_x dt \\ l_y dt \\ l_z dt \end{bmatrix}. \quad (\text{B.1})$$

It follows that $\vec{r}^j = \vec{r}_1 + \vec{l}(t)$ and

$$\vec{r} = \vec{R} - \vec{r}^j = \begin{bmatrix} x - r_{1x} - l_x t \\ y - r_{1y} - l_y t \\ z - r_{1z} - l_z t \end{bmatrix}.$$

The cross product $\vec{r} \times d\vec{l}$ has a particularly simple and symmetric form independent of t :

$$\vec{r} \times d\vec{l} = \begin{bmatrix} l_y(z - r_{1z}) - l_z(y - r_{1y}) \\ l_z(x - r_{1x}) - l_x(z - r_{1z}) \\ l_x(y - r_{1y}) - l_y(x - r_{1x}) \end{bmatrix}. \quad (\text{B.2})$$

Thus, equation 3.16 becomes:

$$\vec{B}(x, y, z) = \frac{\mu_0 I}{4\pi} \begin{bmatrix} l_y(z - r_{1z}) - l_z(y - r_{1y}) \\ l_z(x - r_{1x}) - l_x(z - r_{1z}) \\ l_x(y - r_{1y}) - l_y(x - r_{1x}) \end{bmatrix} \int_0^1 \frac{dt}{[(x - r_{1x} - l_x t)^2 + (y - r_{1y} - l_y t)^2 + (z - r_{1z} - l_z t)^2]^{3/2}}. \quad (\text{B.3})$$

The integral in equation B.3 is an elementary one and has an analytic solution, which, for the sake of compactness, will not be shown here.

B.2 Infinitely flat conductor

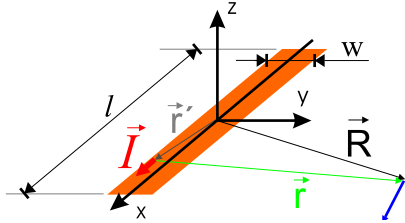


Figure B.2: Infinitely flat wire with the length l and width w laying in the $z = 0$ plane parallel to the x -axis.

For the conductors with a finite cross-section, the Biot-Savart law can be written in a more general form:

$$\vec{B}(\vec{R}) = \frac{\mu_0}{4\pi} \int_V d^3r' \vec{I}(r') \times \frac{\vec{R} - r'}{|\vec{R} - r'|^3}, \quad (\text{B.4})$$

with integration performed over the entire volume V of the current carrying conductor. \vec{I} is a current density vector and has a dimension A/m².

The field outside a cylindrical conductor is identical to that of an infinitely thin wire centered on the cylinder axis. Microfabricated wires, however, typically have a rectangular cross section with the height much smaller than the width ($7 \times 30 \mu\text{m}$ in the Quantus chip). The field of such a conductor is therefore well approximated by that of an infinitely flat wire with the zero

height, but the nonzero width w , for which an analytical solution to integral B.4 exists.

Consider a flat conductor with the length l and width w from the figure B.2. For simplicity it is centered at the origin and oriented parallel to the x -axis. In that case, the current flow vector inside of the conductor is constant and can be expressed by:

$$\vec{I} = I_w \hat{e}_x \delta(z), \quad (\text{B.5})$$

with $\delta(z)$ - the Dirac delta function, $\hat{e}_x = [1, 0, 0]$, and the linear current density $I_w = I/w$ (in A/m). Substituting B.5 in B.4 and with $\vec{R} - \vec{r}' = [x - x', y - y', z]$, the equation B.4 becomes:

$$\vec{B}(\vec{R}) = \frac{\mu_0 I}{4\pi w} \int_{-l/2}^{l/2} dx' \int_{-w/2}^{w/2} dy' \begin{bmatrix} 0 \\ -z \\ y - y' \end{bmatrix} \frac{1}{[(x - x')^2 + (y - y')^2 + z^2]^{3/2}}. \quad (\text{B.6})$$

This surface integral has an analytic solution, which is elementary but lengthy and will not be presented here. For $x = y = 0$ it simplifies to:

$$\vec{B}(z) = \frac{\mu_0 I}{4\pi w} \begin{bmatrix} 0 \\ -4 \text{ArcTan}\left(\frac{lw}{2z\sqrt{l^2+w^2+4z^2}}\right) \\ 0 \end{bmatrix}. \quad (\text{B.7})$$

The field in this case has the y -component only, which is plotted in figure B.3 (green) and compared to the field of an infinitely thin wire of the same length (red). It is apparent, that only at the distances comparable to w the two curves differ sufficiently. In the Quantus experiment, even a highly compressed magnetic trap has its minimum at the distance $z_0 \approx 100 \mu\text{m}$ from the chip surface, still three times more than the width of the central wire. Thus, for steep potentials the use of infinitesimally thin wire approximation is fully justified. However, shallow trap is much more sensitive to the current distribution so that the width and the form of the conductors should be considered (note that the width of the wires providing current to the central part of the Quantus chip reaches 1 mm - see Fig. C.1).

B.3 Approximating an arbitrary shape conductor with a chain of thin straight wires

Although an analytic solution for the magnetic field of a flat conductor exists, it is not very useful in practice. First, compared to a thin wire, it would be much more difficult (though still possible) to parametrize a piece of a flat

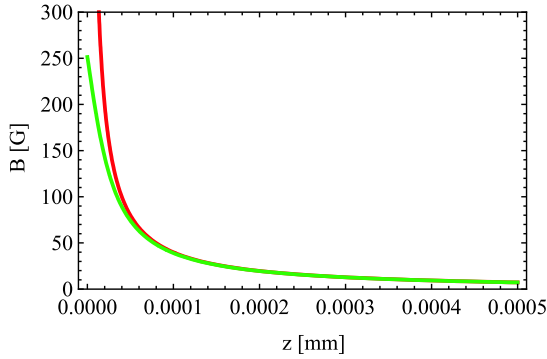


Figure B.3: Magnetic field amplitude along $\vec{R} = [0, 0, z]$ for a finite flat wire oriented as in figure B.2 with the width $w = 50 \mu\text{m}$ and the length $l = 2 \text{ mm}$ (green), and the field of an infinitesimally thin wire of the same length (red). The current is in both cases $I = 2 \text{ A}$. Note the finite value of the flat wire field at $z = 0$.

wire that is oriented arbitrarily in space. Second, current density is not well defined at the connection of two rectangular coplanar flat wires. This limits the flat wire approximation to the conductor pieces much longer than their width. Last, the model deals with constant current densities within a single piece, which is not the case for tapered conductors.

To omit the above limitations we model the strip lines of the Quantus chip with a chain of equidistant straight thin wires (Fig. B.4). As input to the routine which calculates the magnetic field, one just needs to specify the number of thin wires and the coordinates of the pinch points at the right and left edge of the conductor (Fig. C.1). Magnetic field of each single thin wire is calculated according to formula B.3 and contributions from all thin pieces are summed. Note that this method can be easily extended to the conductors with a finite height and arbitrary shape of the cross-section.

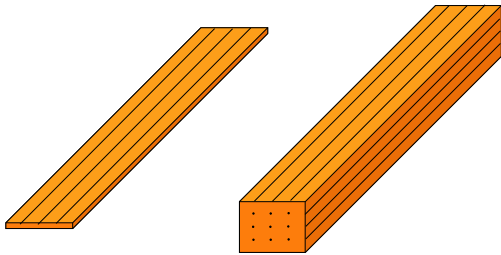


Figure B.4: Flat conductor (left) can be approximated by a chain of equidistant straight thin wires (black). The method can be straightforwardly applied to conductors with finite height (right).

Appendix C

Technical drawings

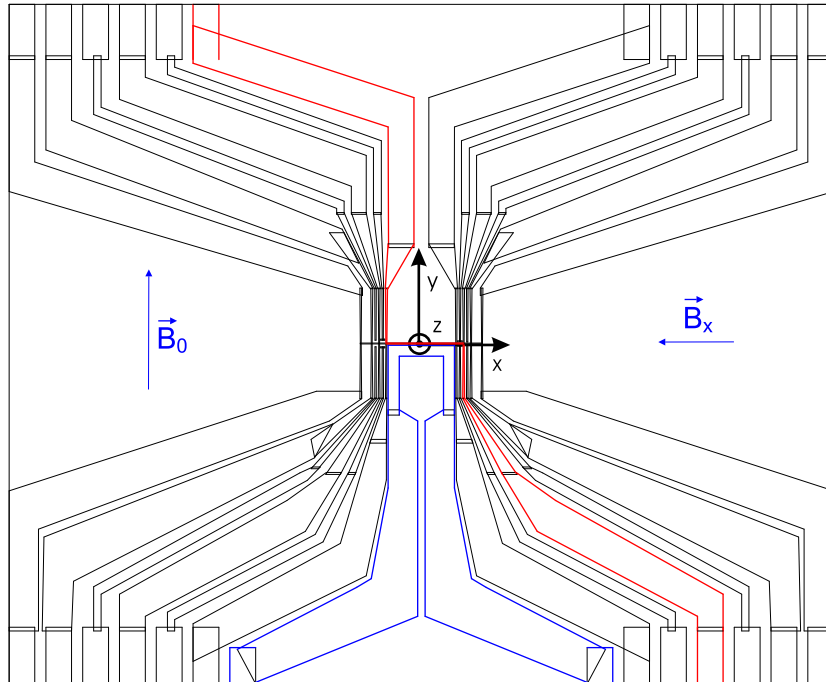


Figure C.1: Wire structure of the Quantus chip. The coordinates (in mm) of the pinch points at the left and right edge of the Z-wire are:

$Leftedge=[(-6.2,9.2),(-6.2,7.6),(-0.9,5.87),(-0.9,2.7),(-0.96,-0.0015),(1.14,-0.015),(1.12,-1.5),(2.2,-3.55),(3.15,-5.1),(7.5,-7.4),(7.5,-9.2)]$

$Rightedge=[(-5.5,9.2),(-5.5,8.45),(-0.2,6.67),(-0.2,2.6),(-0.91,1.48),(-0.93,0.015),(1.16,0.015),(1.17,-1.48),(2.58,-3.5),(3.65,-4.26),(8.2,-6.8),(8.2,-9.2)]$

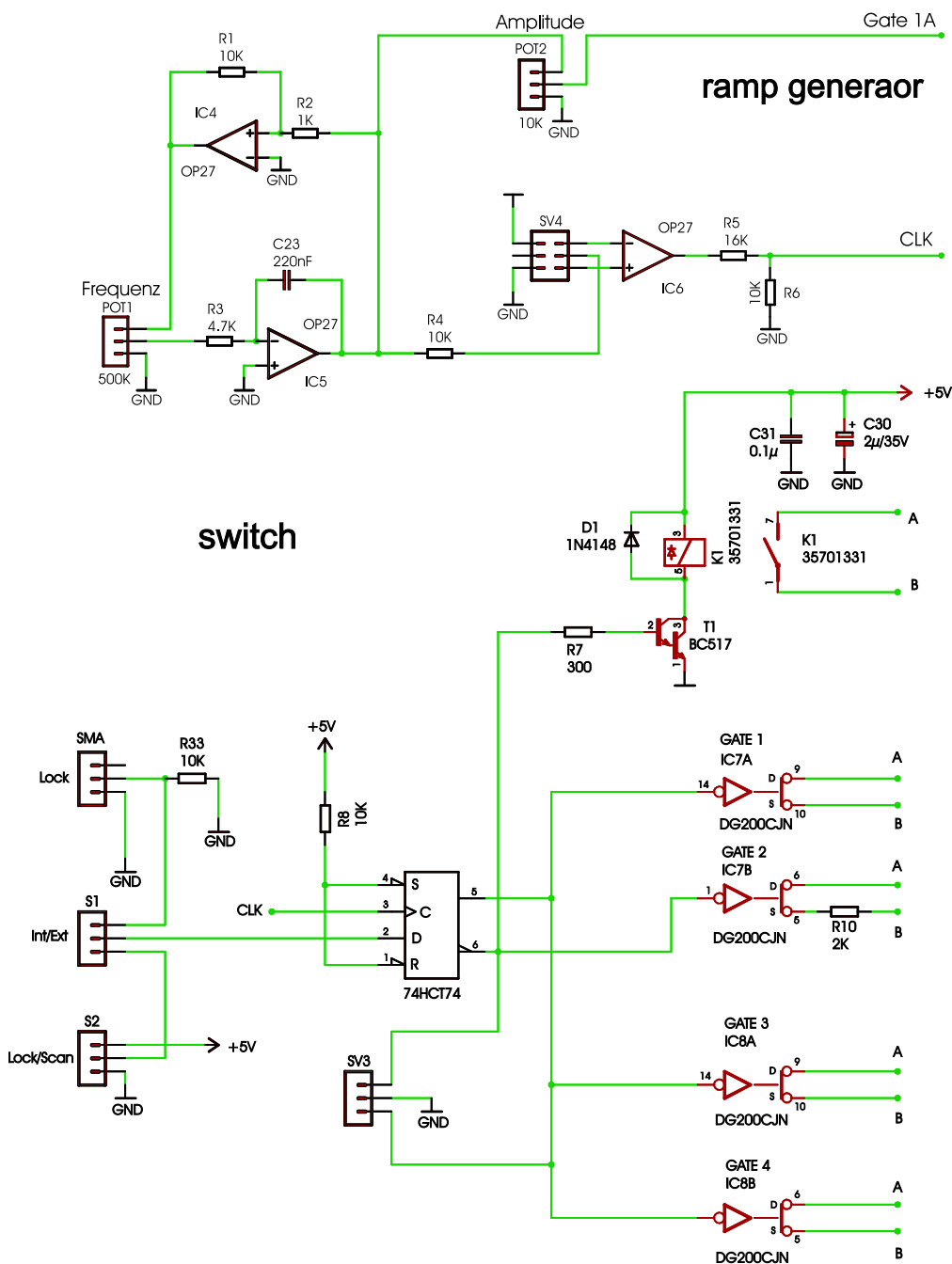
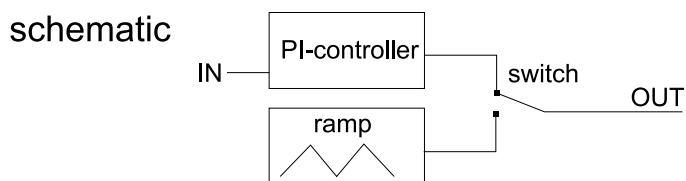


Figure C.2: Lockbox circuit 1

PI-controller

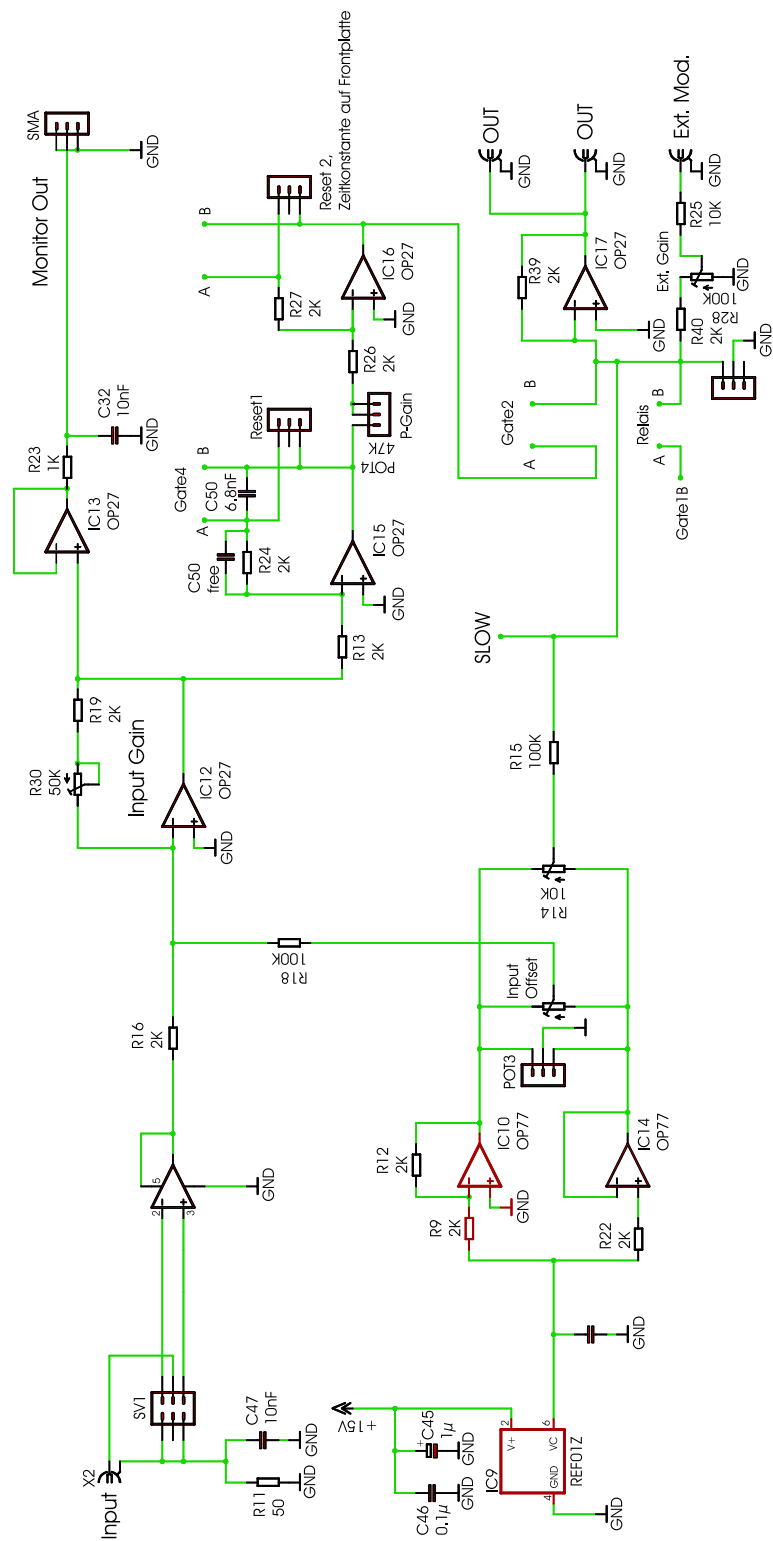


Figure C.3: Lockbox circuit 2

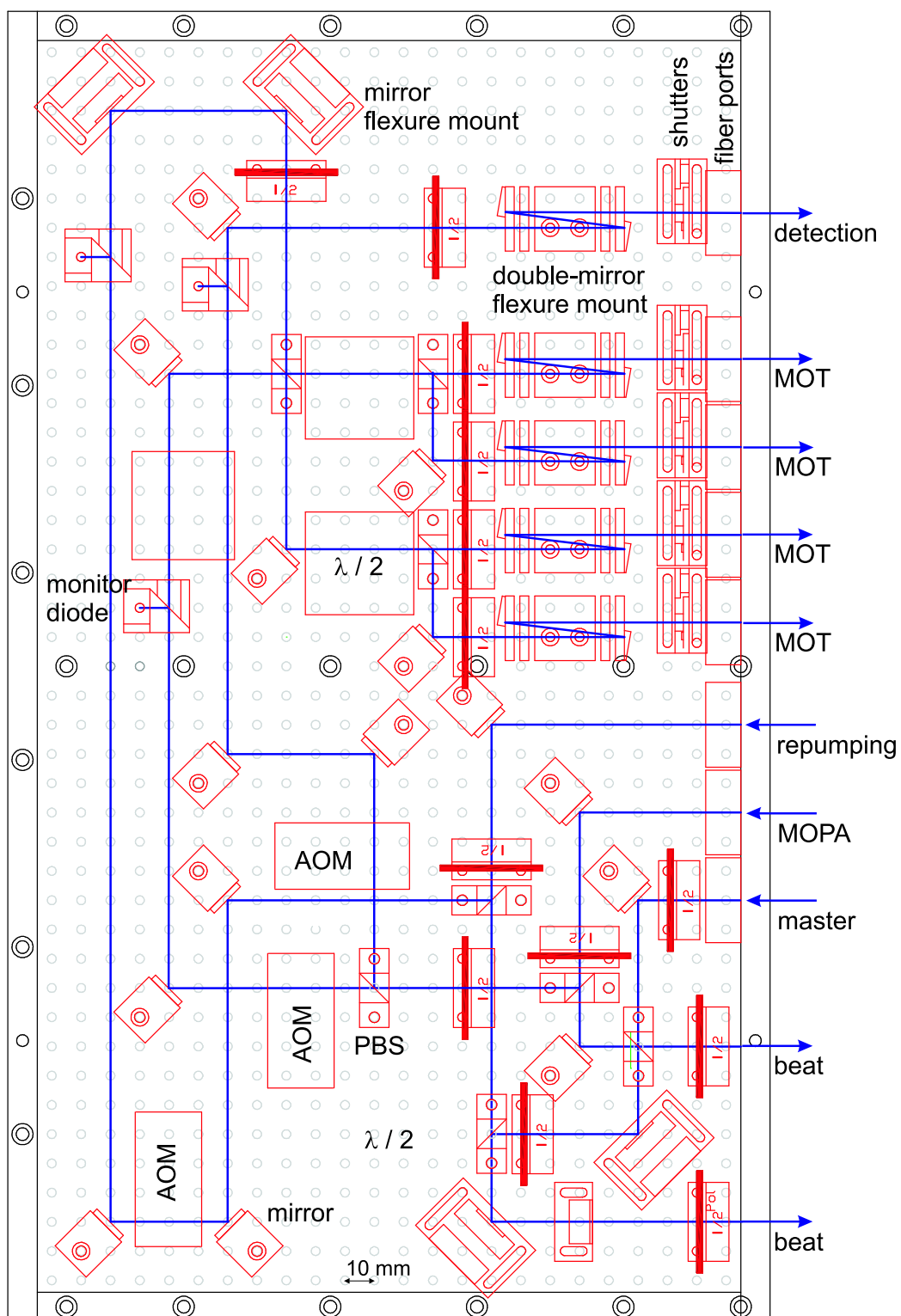


Figure C.4: AOM module

Optical Component	Manufacturer	Model Number	Custom Mount Design
Master Oscillator Power Amplifier (MOPA)	DFB: Eagleyard TA: Eagleyard MOPA: custom design	-	
1/2 waveplate	Laser Components	442WPL1225-L/2-780, cut into 5x5 mm ² pieces	
Polarizer	Codixx	ColorPol®VIS700 BC4 CW02	
Isolator 60 dB Low Power	Isowave	I-80-U-2, I-80-U-4	
Isolator 30 dB High Power	EOT	WT-04-I-780-HP-000	
Mirror (adjustable)	CVI	1/2" 780 nm, 0-45°	
Mirror (non-adjustable)	CVI	1/2" 780 nm, 0-45°	
Polarizing Beamsplitter (PBS)	Linos	335-513-000	

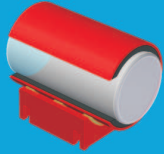

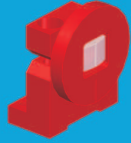
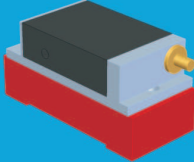
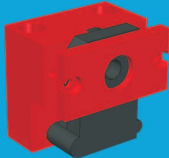
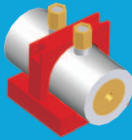

Rubidium Vapour Cell	Toptica	CE RB 50	
Spherical Lens	Linios	1/2" 780 nm, various f	
Cylindrical Lens	Thorlabs	LJ1810L2-B, cut into 8.3x10 mm ² slices	
Acousto-Optical Modulator (AOM)	Crystal Technology	3080-125	
Shutter	Sunex	SHT934	
Electro-Optical Modulator (EOM)	Linios	LM 13 Phas Custom housing	
Fiber Coupler	Schäffer+Kirchhoff	60SMS-1-4-A4,5S-02	

Figure C.5: *Optical components of the Quantus laser system*

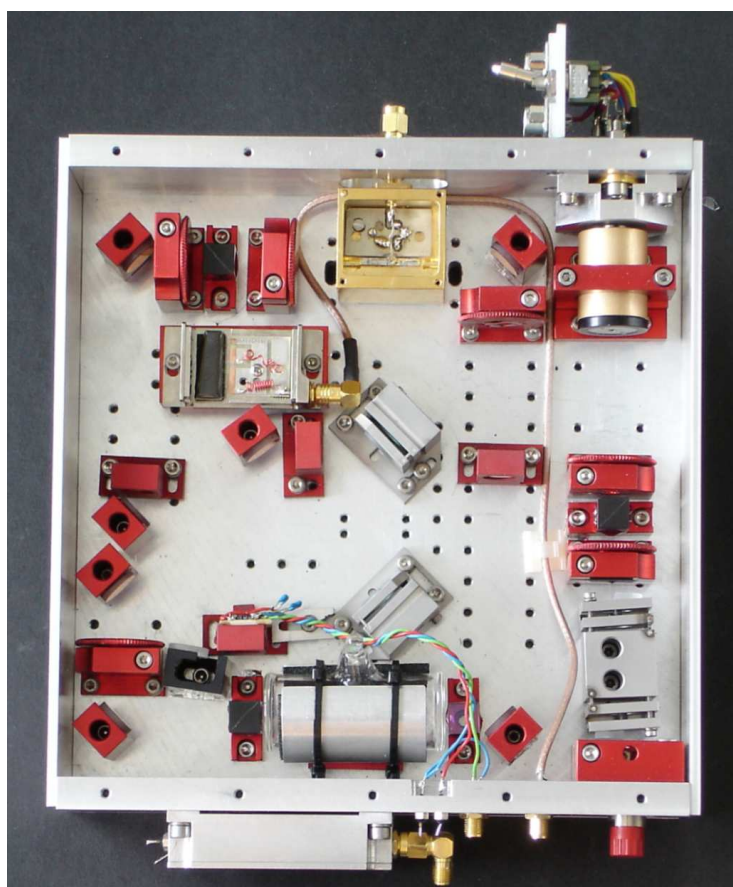


Figure C.6: *MTS master laser*

Bibliography

- J. Stuhler, A. Griesmaier, T. Koch, M. Fattori, T. Pfau, S. Giovanazzi, P. Pedri, and L. Santos. Observation of dipole-dipole interaction in a degenerate quantum gas. *Phys. Rev. Lett.*, 95(15):150406, 2005.
- H. Schmaljohann, M. Erhard, J. Kronjäger, K. Sengstock, and K. Bongs. Dynamics and thermodynamics in spinor quantum gases. *Appl. Phys. B*, 79(8):1001–1007, 2004.
- Ph. Laurent, P. Lemonde, E. Simon, G. Santarelli, A. Clairon, N. Dimarcq, P. Petit, C. Audoin, and C. Salomon. A cold atom clock in absence of gravity. *Eur. Phys. J. D*, 3:201–204, 1998.
- S. N. Bose. Plancks gesetz und lichtquantenhypothese. *Z. Phys. A*, 26(1): 178–181, 1924.
- M. Alonso and E. J. Finn. *Quantenphysik und Statistische Physik*. Oldenbourg Verlag, 2005.
- A. Einstein. Quantentheorie des einatomigen idealen gases. zweite abhandlung. *Sitzungber. Preuss. Akad. Wiss.*, 3, 1925.
- D. W. Snoke, J. P. Wolfe, and A. Mysyrowicz. Evidence for bose-einstein condensation of a two-component exciton gas. *Phys. Rev. Lett.*, 64(21): 2543–2546, 1990.
- K. B. Davis, M. O. Mewes, M. R. Andrews, N. J. van Druten, D. S. Durfee, D. M. Kurn, and W. Ketterle. Bose-einstein condensation in a gas of sodium atoms. *Phys. Rev. Lett.*, 75(22):3969–3973, 1995a.
- M. H. Anderson, J. R. Ensher, M. R. Matthews, C. E. Wieman, and E. A. Cornell. Observation of bose-einstein condensation in a dilute atomic vapor. *Science*, 269:198–201, 1995.

- C. C. Bradley, C. A. Sackett, J. J. Tollett, and R. G. Hulet. Evidence of bose-einstein condensation in an atomic gas with attractive interactions. *Phys. Rev. Lett.*, 75(9):1687–1690, 1995.
- W. Ketterle, D.S. Durfee, and D.M. Stamper-Kurn. Making, probing and understanding bose-einstein condensates. In *Bose-Einstein condensation in atomic gases, Proceedings of the International School of Physics "Enrico Fermi", Course CXL*, pages 67–176, 1999.
- K. Bongs and K. Sengstock. Physics with coherent matter waves. *Rep. Prog. Phys.*, 67:907–963, 2004.
- C. J. Pethick and H. Smith. *Bose-Einstein Condensation in Dilute Gases*. Cambridge University Press, 2002.
- L. P. Pitaevskii and S. Stringari. *Bose-Einstein Condensation*. Oxford University Press, 2003.
- A. E. Leanhardt, T. A. Pasquini, M. Saba, A. Schirotzek, Y. Shin, D. Kielpinski, D. E. Pritchard, and W. Ketterle. Cooling bose-einstein condensates below 500 picokelvin. *Science*, 301:1513–1515, 2003.
- D. B. Sullivan, J. C. Bergquist, J. J. Bollinger, R. E. Drullinger, W. M. Itano, S. R. Jefferts, W. D. Lee, D. Meekhof, T. E. Parker, F. L. Walls, and D. J. Wineland. Primary atomic frequency standards at nist. *J. Res. Natl. Inst. Stand. Technol.*, 106(1):47–63, 2001.
- N. F. Ramsey. Experiments with separated oscillatory fields and hydrogen masers. *Rev. Mod. Phys.*, 62(3):541–552, 1990.
- G. Santarelli, Ph. Laurent, P. Lemonde, A. Clairon, A. G. Mann, S. Chang, A. N. Luiten, and C. Salomon. Quantum projection noise in an atomic fountain: A high stability cesium frequency standard. *Phys. Rev. Lett.*, 82(23):4619–4622, 1999.
- Y. Sortais, S. Bize, C. Nicolas, A. Clairon, C. Salomon, and C. Williams. Cold collision frequency shifts in a 87rb atomic fountain. *Phys. Rev. Lett.*, 85(15):3117–3120, 2000.
- A. Peters, K. Y. Chung, and S. Chu. Measurement of gravitational acceleration by dropping atoms. *NATURE*, 400:849–852, 1999.
- A. Peters, K. Y. Chung, and S. Chu. High-precision gravity measurements using atom interferometry. *Metrologia*, 38:25–61, 2001.

- C. Lämmerzahl. The search for quantum gravity effects i. *Appl. Phys. B*, 84 (4):551–562, 2006.
- T. Damour and A. M. Polyakov. The string dilation and a least coupling principle. *Nucl. Phys B*, 423:532–558, 1994.
- T. Damourb and F. Dyson. The oklo bound on the time variation of the fine-structure constant revisited. *Nucl. Phys B*, 480:37–54, 1996.
- H. Marion, F. Pereira Dos Santos, M. Abgrall, S. Zhang, Y. Sortais, S. Bize, I. Maksimovic, D. Calonico, J. Grünert, C. Mandache, P. Lemonde, G. Santarelli, Ph. Laurent, A. Clairon, and C. Salomon. Search for variations of fundamental constants using atomic fountain clocks. *Phys. Rev. Lett.*, 90(15):150801, 2003.
- J. K. Webb, M. T. Murphy, V. V. Flambaum, V. A. Dzuba, J. D. Barrow, C. W. Churchill, J. X. Prochaska, and A. M. Wolfe. Further evidence for cosmological evolution of the fine structure constant. *Phys. Rev. Lett.*, 87 (9):091301, 2001.
- R. F. C. Vessot and M. W. Levine. A test of the equivalence principle using a space-borne clock. *Gen. Rel. Grav.*, 10(3):181–204, 1979.
- R. F. C. Vessot, M. W. Levine, E. M. Mattison, E. L. Blomberg, T. E. Hoffman, G. U. Nystrom, B. F. Farrel, R. Decher, P. B. Eby, C. R. Baugher, J. W. Watts, D. L. Teuber, and F. D. Wills. Test of relativistic gravitation with a space-borne hydrogen maser. *Phys. Rev. Lett.*, 45(26):2081–2084, 1980.
- A. Bauch and S. Weyers. New experimental limit on the validity of local position invariance. *Phys. Rev. D*, 65(8):081101, 2002.
- J. G. Williams, S. G. Turyshev, and D. H. Boggs. Progress in lunar laser ranging tests of relativistic gravity. *Phys. Rev. Lett.*, 93(26):261101, 2004.
- T. J. Sumner. Equivalence principle measurements. *Gen. Rel. Grav.*, 36(10): 2331–2339, 2004.
- S. Fray, C. Alvarez Diez, T. W. Hänsch, and M. Weitz. Atomic interferometer with amplitude gratings of light and its applications to atom based tests of the equivalence principle. *Phys. Rev. Lett.*, 93(24):240404, 2004.
- S. Dimopoulos, P. W. Graham, J. M. Hogan, and M. A. Kasevich. Testing general relativity with atom interferometry. *Phys. Rev. Lett.*, 98(11): 111102, 2007.

- B. Lounis, J. Reichel, and C. Salomon. Laser cooling of atoms in microgravity. *C. R. Acad. Sci. Paris IV*, 316:739–744, 1993.
- R. A. Nyman et al. I.c.e.: a transportable atomic inertial sensor for test in microgravity. *Appl. Phys. B*, 84:673–681, 2006a.
- Ch. Salomon et al. Cold atoms in space and atomic clocks: Aces. *C. R. Acad. Sci. Paris IV*, 2:1313–1330, 2001.
- Ph. Laurent et al. Design of the cold atom pharao space clock and initial test results. *Appl. Phys. B*, 84:683–690, 2006b.
- ZARM Drop Tower Bremen User Manual*. Drop Tower Operation and Service Company, ZARM FABmbH, November 2007. <http://www.zarm.uni-bremen.de/download.html>.
- H. Sellig. Private communication. measurement at ZARM with the ONERA SuperStar accelerometer, 2007.
- A. Vogel, M. Schmidt, K. Sengstock, K. Bongs, W. Lewoczko, T. Schuldt, A. Peters, T. Van Zoest, W. Ertmer, E. Rasel, T. Steinmetz, J. Reichel, T. Könemann, W. Brinkmann, E. Göklü, C. Lämmerzahl, H.J. Dittus, G. Nandi, W.P. Schleich, and R. Walser. Bose-einstein condensates in microgravity. *Appl. Phys. B*, 84:663–671, 2006.
- H. J. Metcalf and P. van der Straten. *Laser cooling and Trapping*. Springer-Verlag, New York, 1999.
- W. D. Phillips. Nobel lecture: Laser cooling and trapping of neutral atoms. *Rev. Mod. Phys.*, 70(3):721–741, 1998.
- T. van Zoest. *Realisierung erster quantenentarteter Gase unter Schwerelosigkeit*. PhD thesis, Der Fakultät für Mathematik und Physik der Gottfried Wilhelm Leibniz Universität Hannover, 2008.
- T. Könemann, W. Brinkmann, E. Göklü, C. Lämmerzahl, H. Dittus, T. van Zoest, E.M. Rasel, W. Ertmer, W. Lewoczko-Adamczyk, M. Schiemangk, A. Peters, A. Vogel, G. Johannsen, S. Wildfang, K. Bongs, K. Sengstock, E. Kajari, G. Nandi, R. Walser, and W.P. Schleich. A freely falling magneto-optical trap drop tower experiment. *Appl. Phys. B*, 89:431–438, 2007.
- J. Reichel, W. Hänsel, P. Hommelhoff, and T.W. Hänsch. Applications of integrated magnetic microtraps. *Appl. Phys. B*, 72:81–89, 2001.

- R. Folman, P. Krüger, J. Schmiedmayer, J. Denschlag, and C. Henkel. Microscopic atom optics: From wires to an atom chip. *Adv. Atom. Mol. Opt. Phys.*, 48:263–356, 2002.
- Y.-C. Chen, W.-B. Lin, H.-C. Hsue, L. Hsu, and I. A. Yu. Effect of the trapping laser linewidth on the atom number in a magneto-optical trap. *Chinese J. Phys.*, 38(5):920–926, 2000.
- J. Carroll, J. Whiteaway, and D. Plumb. *Distributed feedback semiconductor lasers*. The Institution of Electrical Engineers, 1998.
- M. Schiemangk. Entwicklung ultrastabiler Lasersysteme für Experimente mit Quantengasen unter Schwerelosigkeit. Master's thesis, Humboldt-Universität zu Berlin Mathematisch-Naturwissenschaftliche Fakultät I Institut für Physik, 2007.
- S. Kraft, A. Deninger, C. Trüch, J. Fortágh, F. Lison, and C. Zimmermann. Rubidium spectroscopy at 778–780 nm with a distributed feedback laser diode. *Laser Phys. Lett.*, 2(2):71–76, 2005.
- J. H. Shirley. Modulation transfer processes in optical heterodyne saturation spectroscopy. *Opt. Lett.*, 7:537–539, 1982.
- J. Zhang, D. Wei, C. Xie, and K. Peng. Characteristics of absorption and dispersion for rubidium d2 lines with the modulation transfer spectrum. *Opt. Express*, 11(11):1338–1344, 2003.
- G. C. Bjorklund. Frequency-modulation spectroscopy: a new method for measuring weak absorptions and dispersions. *Opt. Lett.*, 5(1):15–17, 1979.
- G. C. Bjorklund and M. D. Levenson. Frequency modulation (fm) spectroscopy. *Appl. Phys. B*, 32:145–152, 1983.
- J. M. Supplee, E. A. Whittaker, and W. Lenth. Theoretical description of frequency modulation and wavelength modulation spectroscopy. *Appl. Opt.*, 33(27):6294–6302, 1994.
- A. C. Wilson, J. C. Sharpe, C. R. McKenzie, P. J. Manson, , and D. M. Warrington. Narrow-linewidth master-oscillator power amplifier based on a semiconductor tapered amplifier. *Appl. Opt.*, 37(21):4871–4875, 1998.
- G. Wasik, W. Gawlik, J. Zachorowski, and W. Zawadzki. Laser frequency stabilization by doppler-free magnetic dichroism. *Appl. Phys. B*, 75:613–619, 2002.

- J. E. Lye, C. S. Fletcher, U. Kallman, H.-A. Bachor, and J. D. Close. Images of evaporative cooling to bose-einstein condensation. *J. Opt. B*, 4:57–61, 2002.
- D. A. Steck. Rubidium 87 d line data. available online at <http://steck.us/alkalidata> (revision 0.2, 1 September 2008), 2008.
- P. D. Lett, R. N. Watts, C. I. Westbrook, and W. D. Phillips. Observation of atoms laser cooled below the doppler limit. *Phys. Rev. Lett.*, 61(2): 169–172, 1988.
- J. Dalibard and C. Cohen-Tannoudji. Laser cooling below the doppler limit by polarization gradients: simple theoretical models. *J. Opt. Soc. Am. B*, 6(11):2023–2045, 1989.
- J. Reichel, F. Bardou, M. Dahan Ben, E. Peik, S. Rand, C. Salomon, and C. Cohen-Tannoudji. Raman cooling of cesium below 3 nk: New approach inspired by lévy flight statistics. *Phys. Rev. Lett.*, 75(25):4575–4578, 1995.
- K. B. Davis, M.-O. Mewes, M. A. Joffe, M. R. Andrews, and W. Ketterle. Evaporative cooling of sodium atoms. *Phys. Rev. Lett.*, 74(26):5202–5205, 1995b.
- K. B. Davis, M.-O. Mewes, and W. Ketterle. Evaporative cooling of sodium atoms. *Appl. Phys. B*, 60:155–159, 1995c.
- W. Ketterle and N.J. van Druten. Evaporative cooling of atoms. *Adv. At. Mol. Opt. Phys.*, 37:181–236, 1996.
- H. Friedburg and W. Paul. Optische abbildung mit neutralen atomen. *Naturwissenschaften*, 38(7):159–160, 1951.
- K.-J. Kügler, W. Paul, and U. Trinks. A magnetic storage ring for neutrons. *Phys. Lett. B*, 72(3):422–424, 1978.
- G. Cennini, G. Ritt, C. Geckeler, and M. Weitz. All-optical realization of an atom laser. *Phys. Rev. Lett.*, 91(24):240408, 2003.
- W. H. Wing. On neutral particle trapping in quasistatic electromagnetic fields. *Progr. Quant. Electr.*, 8:181–199, 1984.
- E. Majorana. Atomi orientati in campo magnetico variabile. *Nuovo Cimento*, 9(43), 1932.

- D. E. Pritchard. Cooling neutral atoms in a magnetic trap for precision spectroscopy. *Phys. Rev. Lett.*, 51(15):1336–1339, 1983.
- T. Bergeman, G. Erez, and H. J. Metcalf. Magnetostatic trapping fields for neutral atoms. *Phys. Rev. A*, 35(4):1535–1546, 1987.
- J. D. Weinstein and K. G. Libbrecht. Microscopic magnetic traps for neutral atoms. *Phys. Rev. A*, 52(5):4004–4009, 1995.
- K. Dieckmann. *Bose-Einstein Condensation with High Atom Number in a Deep Magnetic Trap*. PhD thesis, Universiteit van Amsterdam, Faculteit der Natuurwetenschappen, Van der Waals-Zeeman Instituut, 2001.
- H. Ott, J. Fortagh, G. Schlotterbeck, A. Grossmann, and C. Zimmermann. Bose-einstein condensation in a surface microtrap. *Phys. Rev. Lett.*, 87(23):230401, 2001.
- P. D. Schwindt. *Magnetic Traps and Guides for Bose-Einstein Condensates on an Atom Chip: Progress toward a Coherent Atom Waveguide Beam-splitter*. PhD thesis, Faculty of the Graduate School of the University of Colorado, Department of Physics, 1997.
- W. Hänsel, P. Hommelhoff, T. W. Hänsch, and J. Reichel. Bose-einstein condensation on a microelectronic chip. *NATURE*, 413:498–501, 2001.
- J. Denschlag, D. Cassettari, and Jörg Schmiedmayer. Guiding neutral atoms with a wire. *Phys. Rev. Lett.*, 82(10):2014–2017, 1999.
- Yu. Kagan, E. L. Surkov, and G. V. Shlyapnikov. Evolution of a bose-condensed gas under variations of the confining potential. *Phys. Rev. A*, 54(3):1753–1756, 1996.
- Y. Castin and R. Dum. Bose-einstein condensates in time dependent traps. *Phys. Rev. Lett.*, 77(27):5315–5319, 1996.
- M. Eckart. *Non-equilibrium dynamics of trapped gases in controlled geometries*. PhD thesis, Institut für Quantenphysik, Universität Ulm, Germany, 2008.
- P. A. Ruprecht, M. J. Holland, and K. Burnett. Time-dependent solution of the nonlinear schrödinger equation for bose-condensed trapped neutral atoms. *Phys. Rev. A*, 51(6):4704–4711, 1995.
- F. Bloch. Nuclear induction. *Phys. Rev.*, 70:460–474, 1946.

- C. R. Ekstrom, C. Kurtsiefer, D. Voigtand O. Dross, T. Pfau, and J. Mlynek. Coherent excitation of a he^* beam observed in atomic momentum distributions. *Opt. Comm.*, 123:505–511, 1999.
- J. C. Camparo and R. P. Frueholz. Parameters of adiabatic rapid passage in the 0-0 hyperfine transition of $\text{rb}87$. *Phys. Rev. A*, 30(2):803–811, 1984.
- J. C. Camparo and R. P. Frueholz. A dressed atom interpretation of adiabatic rapid passage. *J. Phys. B: At. Mol. Phys.*, 17:4169–4178, 1984.
- P. J. Mar, B. G. Oldaker, H. A. Miklich, and D.E. Pritchard. Bragg scattering of atoms from a standing light wave. *Phys. Rev. Lett.*, 60(6):515–518, 1988.
- M. Kozuma, L. Deng, E. W. Hagley, J. Wen, R. Lutwak, K. Helmerson, S. L. Rolston, and W. D. Phillips. Coherent splitting of bose-einstein condensed atoms with optically induced bragg diffraction. *Phys. Rev. Lett.*, 82(5):871–875, 1999.
- David M. Giltner, R. W. McGowan, and S. A. Lee. Theoretical and experimental study of the bragg scattering of atoms from a standing light wave. *Phys. Rev. A*, 52(5):3966–3972, 1995.
- K. Paschke, T. Reiche, G. Erbert, R. Güther, J. Fricke, F. Bugge, and J. Sebastian. 1.6 w hybrid master oscillator power amplifier with α -dfb-laser as master oscillator at 1057 nm. *El. Lett.*, 38(7):321–322, 2002.
- S. Schwertfeger, A. Klehr, and G. Erbert. Compact hybrid master oscillator power amplifier with 3.1-w cw output power at wavelengths around 1061 nm. *IEEE Phot. Techn. Lett.*, 16(5):1268–1270, 2004.
- S. Wildermuth, P. Krüger, C. Becker, M. Brajdic, S. Haupt, A. Kasper, R. Folman, and J. Schmiedmayer. Optimized magneto-optical trap for experiments with ultracold atoms near surfaces. *Phys. Rev. A*, 69(3):030901, 2004.
- K. Dieckmann, R. J. C. Spreeuw, M. Weidemüller, and J. T. M. Walraven. Two-dimensional magneto-optical trap as a source of slow atoms. *Phys. Rev. A*, 58(5):3891–3895, 1998.

Danksagung

Ganz herzlich möchte ich mich bei meinem Doktorvater, Herrn Professor Achim Peters bedanken: für die Aufnahme in seine Arbeitsgruppe und die Möglichkeit an einem hochinteressanten Experiment diese Arbeit anfertigen zu können. Vielen Dank für die 4 Jahre Betreuung und Einführung in die für mich neuen Messtechniken.

Dem QUANTUS-Projektleiter Herrn Prof. Ernst Rasel danke ich für eine gute Stimmung im Team und für die Motivierung in schweren Zeiten.

Meinen QUANTUS-Mitdoktoranden der ersten Generation: Anika Vogel, Tim van Zoest und Endre Kajari für eine fruchtbare Zusammenarbeit und eine entspannte Arbeitsatmosphäre,

Dr. Reinhold Walser danke ich ganz besonders für die wertvolle Mathematica Tipps,

Dem gesamten neuen Quantus-Team: ihr seid toll!,

Thilo Schuldt für die "Vertretung" am Anfang. Und für die rot-eloxierte Halterungen,

Sven Herrmann für die Sprachkorrekturen,

Evgeny Kovalchuk für seine immer praktische Tipps im Labor und die berühmte Hammertests des Lasers. Und für Äpfel!

Allen QOMs und NANOs für eine gute Stimmung am Hausvogteiplatz,

Sylvia Richter und Sabine Strobel für die Bewältigung des Papierkrams,

Klaus Palis für die Unterstützung in den Sachen Elektronik und Werkstatt,

Thorsten Lutz, Dieter Bischoff und Wiebke Brinkmann für die Unterstützung am Fallturm,

Ich möchte mich auch besonders bei Herrn Prof. Hanspeter Helm bedanken.

Er war dabei als ich die ersten Schritte als Physiker gemacht habe. Seine große Persönlichkeit und ein besonders intuitives Verständnis der Physik haben mein Interesse an der Forschung geweckt.

Euch allen vielen Dank!

Zum Schluss möchte ich noch einen süßen Kuss an Młoda schicken: cmok!
Młodowska, dzięki za wsparcie. I za to że jesteś!!!

Selbständigkeitserklärung

Hiermit erkläre ich, die vorliegende Arbeit selbständig ohne fremde Hilfe verfasst und nur die angegebene Literatur und Hilfsmittel verwendet zu haben. Ich habe mich anderwärts nicht um einen Doktorgrad beworben und besitze einen entsprechenden Doktorgrad nicht.

Ich erkläre die Kenntnisnahme der dem Verfahren zugrunde liegenden Promotionsordnung der Mathematisch-Naturwissenschaftlichen Fakultät I der Humboldt-Universität zu Berlin.

Berlin, 19.12.2008

Wojciech Lewoczko-Adamczyk